New timing estimations of cardiovascular events; applications to seismocardiography, microneurography, and blood pressure.

by

Alexandre Laurin

M.Sc., Concordia University, 2011
B.Sc., Concordia University, 2008

Dissertation Submitted in Partial Fulfillment
of the Requirements for the Degree of
Doctor of Philosophy

in the
Department of Biomedical Physiology and Kinesiology
Faculty of Science

SIMON FRASER UNIVERSITY
Fall 2015

Approval

Name:	Alexandre Laurin
Degree:	Doctor of Philosophy (Biomedical Physiology and Kinesiology)
Title:	*New timing estimations of cardiovascular events; applications to seismocardiography, microneurography, and blood pressure.*
Examining Committee:	**Dr. Damon Poburko** (chair) Professor
Dr. Andrew Blaber Senior Supervisor Professor	_____
Dr. Nandu Goswami Supervisor Associate Professor Institute of Physiology Medical University of Graz	_____
Dr. James Wakeling Supervisor Professor	_____
Dr. Sébastien Imperiale Supervisor Researcher Inria, France	_____
Dr. Rodney Vaughan Internal Examiner Professor School of Engineering Science	_____
Dr. Marco DiRienzo External Examiner Adjunct Professor Faculty of Medicine University of Milan	_____
Date Defended:	25 September 2015

Ethics Statement

The author, whose name appears on the title page of this work, has obtained, for the research described in this work, either:

a. human research ethics approval from the Simon Fraser University Office of Research Ethics,

or

b. advance approval of the animal care protocol from the University Animal Care Committee of Simon Fraser University;

or has conducted the research

c. as a co-investigator, collaborator or research assistant in a research project approved in advance,

or

d. as a member of a course approved in advance for minimal risk human research, by the Office of Research Ethics.

A copy of the approval letter has been filed at the Theses Office of the University Library at the time of submission of this thesis or project.

The original application for approval and letter of approval are filed with the relevant offices. Inquiries may be directed to those authorities.

Simon Fraser University Library
Burnaby, British Columbia, Canada

update Spring 2010

Abstract

There is a wealth of untapped information within commonly acquired cardiovascular signals. Electric, vibration, and pressure measurements in the cardiovascular system allow us to obtain precise timings of events that can inform us about its ability to maintain health. In particular, this thesis applies new data analysis methods to continuous blood pressure, muscle sympathetic nerve activity, and seismocardiography measurements.

Three phase estimation techniques, including one of our own design, were compared in terms of accuracy. The three techniques were based on wavelet analysis, Hilbert analysis, and a new peak detection method. All three techniques performed with equivalent accuracy, with the wavelet technique being computationally slower.

The new peak detection technique was applied to blood pressure and muscle sympathetic nerve activity data on participants undergoing lower body negative pressure. A set of six new indices returned values analogous to those obtained from traditional methods, suggesting their validity.

A third study considered seismocardiography, which measures thoracic vibrations as they pertain to the beating heart, and contains unique information about cardiac mechanics. At levels of lower body negative pressure of intensity below -30 mmHg, the algorithm was 95% accurate, and the heart rate variability indices were not statistically different from those obtained with electrocardiography.

The mechanical processes that cause seismocardiogram fiducial points have not been identified. By modelling the viscoelastic properties of thoracic materials, a previously developed solving algorithm was used to simulate seismocardiograms caused by a heart-like force applied to the sternum. Both simulations contained peaks analogous to all *in-vivo* seismocardiogram fiducial points.

Keywords: signal analysis, cardiovascular physiology, seismocardiography, 3D modelling, phase estimation, microneurography, muscle sympathetic nerve activity, blood pressure, lower body negative pressure, syncope, orthostatic intolerance, wavelet analysis, Hilbert analysis

Acknowledgements

I would like to acknowledge the contributions of the members of my supervisory committee, Andrew Blaber, Nandu Goswami, James Wakeling, and Sébastien Imperiale, without whom this work would not have been possible.

Furthermore, I would like extend a warm tip of the hat to:
Kouhyar Tavakolian who got a permanent position just a little too late to get a well-deserved place on my supervisory committee;
William Cupples for giving me a room with a view;
Nicholas Mitrou for activating the cage;
Carole Leguy for opening the door to world collaborations;
Farzad Khosrow-Khavar who for a while was the only person in the world who understood chapter 4;
as well as Dominique Chapelle and Phillipe Moireau for giving me the opportunity to bring my research to the next level.

Thank you.

Dedication

I dedicate this thesis to Katherine Carroll Laurin, who I hope will endure my incessant arguing for at least a while longer.

Table of Contents

List of Tables

List of Figures

Chapter 1

Introduction

> Creation is no great feat. Anything you make, I can unmake in a heartbeat.
>
> *Alexi, zephyr mage*

1.1 Motivation

At first glance, it is surprising that the analysis of the electrical activity of the heart, together with the analysis of blood pressure, can give us information about the central nervous system. Even more surprising is the fact that the state-of-the-art analysis techniques that are used to obtain this information are substantially based on mathematical manipulations developed in the early 19^{th} century. It is clear that the physiology and mathematics research communities gain from communicating openly and sharing advances.

In the case of the cardiovascular system, every year brings new diagnosis, monitoring, and treatment methods for a wide array of disorders. Concurrently, data collection and analysis techniques are constantly being revised and upgraded.

Concealed in electric, vibration, and pressure measurements on the human body are precise timings of cardiovascular events that can offer an abundance of information about its ability to maintain health. The timing between rises and drops in blood pressure with respects to nervous activity tells us how fast the brain is capable of processing and relaying crucial information. The timing between the opening and closing of the heart's aortic valve tells us how fast the heart is capable of pumping blood into circulation. If these timings are too long or too short, it can make the difference between fainting or staying conscious, going improperly or properly through the hospital triage process, and ultimately being in poor or good health.

There is a wealth of untapped information in the kinds of cardiovascular signals that have been acquired by researchers for years. The potential for new discoveries in this respect lies precisely at the convergence of the mathematical and physiological fields. The goal of

this thesis was to build bridges between mathematics and physiology, and use them to explore new avenues for obtaining precise timings in existing cardiovascular signals.

1.2 The cardiovascular system

1.2.1 The heart, arteries, and veins

Blood contributes to about 7% of the average adult human's body mass. This translates to roughly 5 litres. The main purpose of blood is the transport of chemicals, which requires circulation. Since liquids always flow from locations of high pressure to locations of low pressure, these quantities are well studied within the human body. In the cardiovascular system, the source of the most important blood pressure gradient is the heart (Fig. 1.1).

The arteries and veins are the conduits where blood is able to flow. Far from being passive, they include a number of mechanisms that encourage proper circulation. On the arterial side, and to a lesser extent on the venous side, the smooth muscles that line the vessels are able to contract and relax according to need, either augmenting or reducing resistance. Flow (Q) is related to resistance (R) and pressure gradient (ΔP), in general, by the relation

$$Q = \frac{\Delta P}{R}. \tag{1.1}$$

The venous side, which acts like a very low resistance blood capacitor, is comprised of relatively short segments separated by one-way valves that prevent back-flow. Mainly, the blood then pools in these segments until an outside perturbation, usually a skeletal muscle contraction or a pressure change due to breathing, propels it to the next segment towards the heart.

1.2.2 Autonomic control of the system

The autonomic nervous system continuously acts to maintain blood pressure homeostasis. It reacts to internal and external stimuli, for example promoting the movement of blood to the gut to help digestion, or to the skeletal muscles during strenuous physical activity.

Within the aortic arch and the carotid sinus, increased blood pressure distends vessel walls, which in turn increases baroreceptor afferent activity. This activity inhibits the vasoconstrictor center of the medulla and excite the vagal parasympathetic center. The net effects in the heart are decreased heart rate and contractility. The effect on the peripheral blood vessels is general dilation. Conversely, reduced vessel wall tension decreases baroreceptor activity and has the opposite net effect.

In the absence of external stimuli, blood pressure, heart rate, and the nervous activity that connects them, all oscillate at a rate of approximately 0.1 Hz. These oscillations are commonly referred to as Mayer waves in blood pressure [1], and constitute a major low-frequency (LF) oscillation in all 3 signals. Although some evidence points to the existence

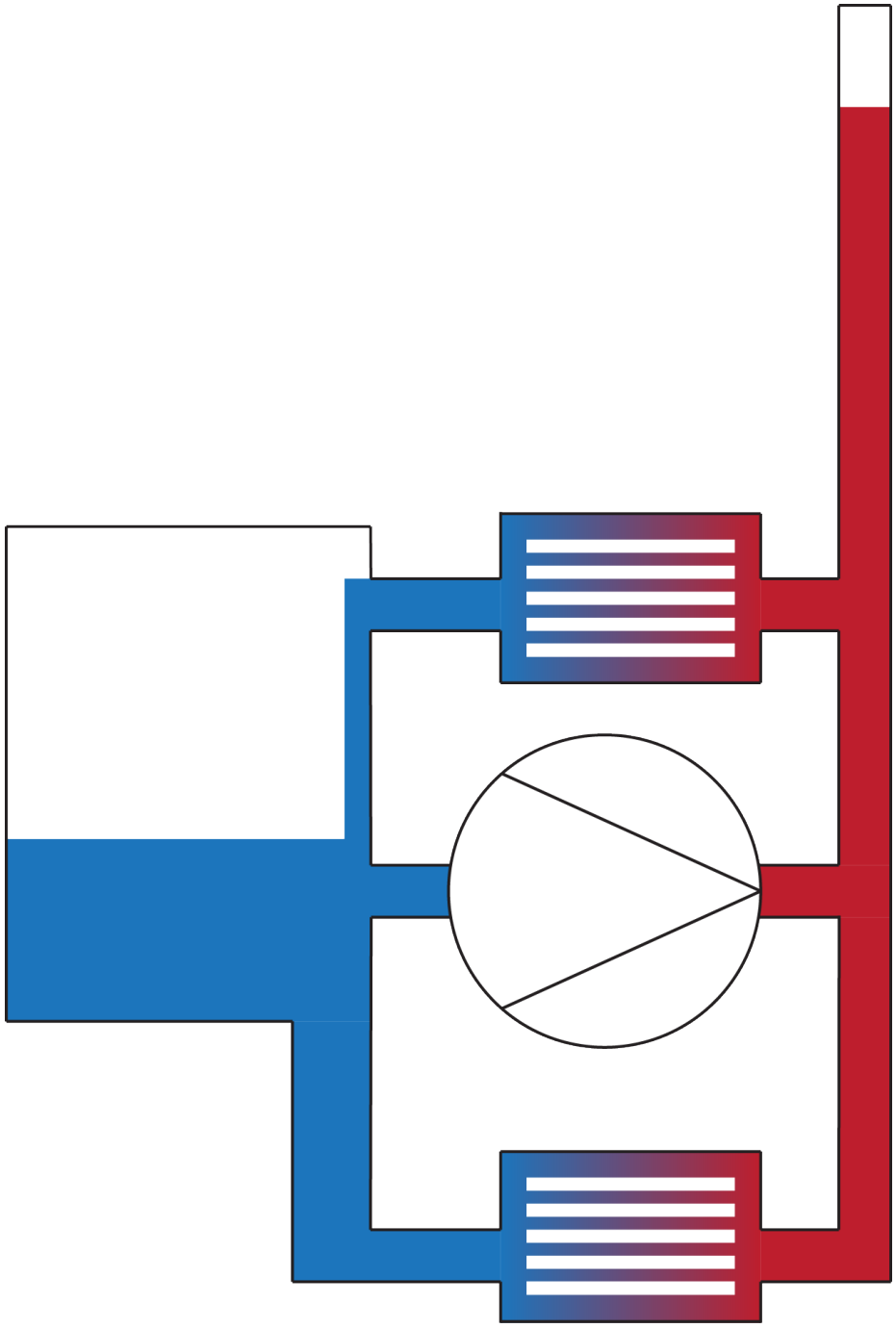

Figure 1.1: A simplified diagram of the cardiovascular system during standing. The venous system is depicted in blue, and the arterial in red. The red to blue gradients represents the capillary beds. The heart is symbolized as a pump in the center. The arterial side has a long narrow column of fluid, and the venous side has a stout column to show that they have low and high capacitance, respectively. The diagram omits pulmonary circulation, but includes circulation in the head.

of a central oscillator responsible for these waves, they are in large part due to inherent time delays in the processes involved in the centrally mediated baroreflex [2]. Communication latency between receptor and effector organs in the baroreflex negative feedback loop causes constant over/under-shoot and readjustment at the resonant frequency of 0.1 Hz (Fig. 3.2). Studying the relationships between the components of LF oscillations is key to understanding the static baroreflex.

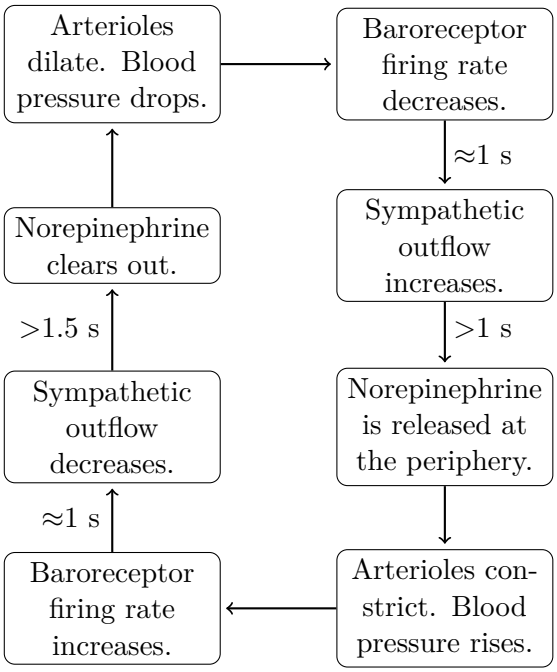

Figure 1.2: Summary of the main pathway of the arterial baroreflex loop. The principal time delays and communication lags are indicated [3, 4, 5]. Low frequency (0.1 Hz) oscillations in blood pressure (Mayer waves), muscle sympathetic nerve activity, and total peripheral resistance emerges from the interactions between these lags and delays [2]. One such loop takes between 7 and 25 seconds, taking into account variations in the amplitude of blood pressure variation and the periods of MSNA activity/inactivity.

1.3 General methodologies

1.3.1 Lower Body Negative Pressure

Lower body negative pressure (LBNP) was first described in 1965 by Stevens *et al.* [6]. It consists of placing the legs, up to the iliac crest in an air-tight box where vacuum is applied (Fig. 1.3). The technique is used to investigate the reaction of the cardiovascular system to stress similar to standing, hypovolemia or hemorrhage, but with minimal muscle pump effect and no vestibular stimuli, thus isolating a purer cardiovascular response [6, 7, 8, 9, 10]. LBNP lowers blood pressure, which decreases parasympathetic and increases

sympathetic outflow, which in turn increases heart rate, cardiac contracttility, and total peripheral resistance (Fig. 1.4). The immediate drop in blood pressure that follows the application of LBNP also distinguishes it from standing or tilting, where the immediate reaction is a short rise in blood pressure [11].

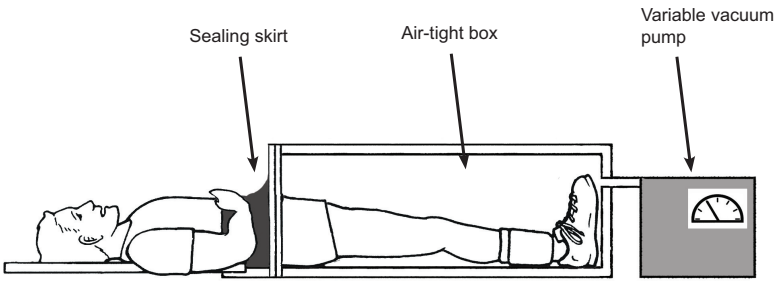

Figure 1.3: Diagram showing a basic lower body negative pressure setup. The seal is at the level of the iliac crest and is often an adjustable neoprene tube.

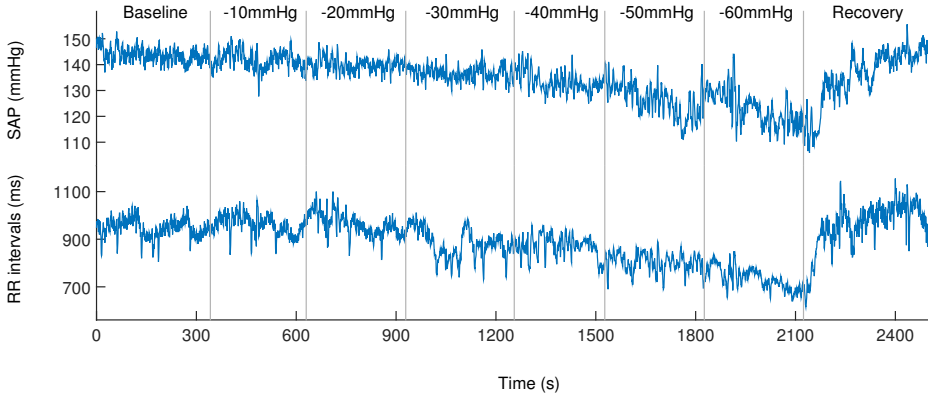

Figure 1.4: An example of a typical systolic arterial pressure (SAP) and RR intervals response during graded lower body negative pressure (LBNP). Visible on both time series are low-frequency ($\approx$ 0.1 Hz) oscillations due to the centrally mediated baroreflex, and high-frequency ($\approx$ 0.3 Hz) oscillations due to breathing.

Basic LBNP setups also have the ability to precisely adjust the amount of stress that is applied to the participant. This allows researchers to study a continuous spectrum of cardiovascular stress, bring subjects to presyncope faster than otherwise, and to end the stress instantly. Furthermore, it allows researchers to model gravitational conditions higher than 1G to simulate aggressive flying, or acute change in gravity such as would occur during the launch or landing of a spacecraft [12, 13]. It has also been shown to be an effective counter-measure to the deleterious effects of long-term microgravity by maintaining exercise rates and hydration, as well as reducing orthostatic intolerance [14, 15, 16].

1.3.2 Microneurography

The initial work on microneurography was conducted in Sweden in the mid nineteen-sixties by Karl-Erik Hagbarth and Åke Vallbo. Their team experimented with various configurations of needles, finally settling on 5-10 μm tungsten electrode tips. Their first publication studied afferent nerve traffic responses to pressure applied on the leg [4]. Before their work, recordings from single nerve fibres could only be obtained from decerebrate or anesthetized animals, and thus never from humans.

The use of needles to measure the activity of single nerve fibres requires careful adjustments of needle placement. Initially, the use of a screen to make minute adjustment was not possible, and audio feedback was used instead. It was while listening to these outputs that researchers first heard 0.1 Hz waves of noise, described as the sound of a calm ocean. In the end, and after much debate, they determined that these waves were in fact due to efferent sympathetic activity from C fibers [17]. The fact that these fibers are unmylinated and 5-10 times smaller than the electrode tip made this discovery quite surprising. The technique has since divided itself in three main areas of research, namely cutaneous sensation, proprioceptive control of voluntary movements, and sympathetic efferent activity [18], the latter of which is now called muscle sympathetic nerve activity (MSNA). It is this last component that is relevant to this thesis and will be discussed further.

Subsequent studies clarified the characteristics of MSNA. Simultaneous recordings in different limbs on a single individual showed striking resemblance, indicating that a single probe in a single muscle could be used as a valid indicator of overall sympathetic nerve traffic [19]. The first systematic (and quite comprehensive) study of the relationship between blood pressure and MSNA was performed by Sundlöf in 1977 [20]. Although lacking in modern signal analysis tools, they laid the foundations for most of the work that is performed today. They estimated the latency between individual heart beats and subsequent MSNA burst, discussed the phase relationship between the two variables, and observed that MSNA increased both in incidence and amplitude with decreasing diastolic pressure, rather than systolic (Fig. 1.4).

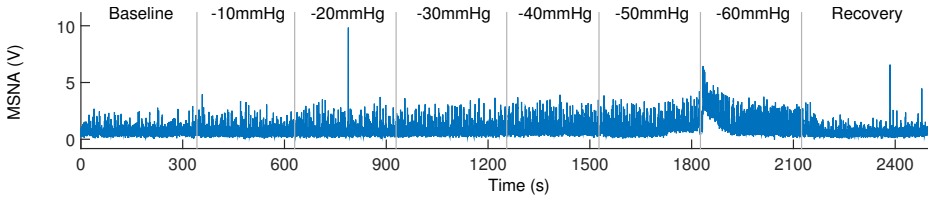

Figure 1.5: An example of a typical muscle sympathetic nervous activity (MSNA) response during graded lower body negative pressure (LBNP). Apparent on the figure is a clear increase in MSNA at the onset of the -60 mmHg section of LBNP. The data was obtained from the same subject and protocol as in Fig. 1.4

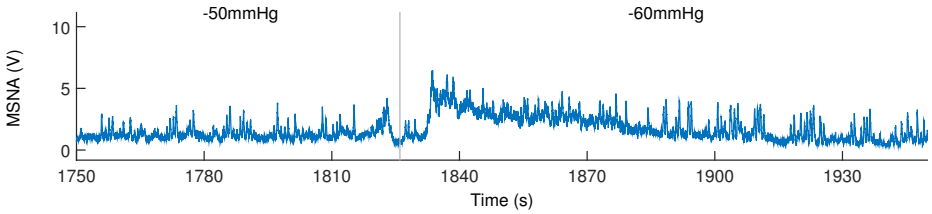

Figure 1.6: Part of Fig. 1.5 showing muscle sympathetic activity in bursts.

There are different ways to quantify MSNA over a period of time. Arguably the most natural, and indeed the one that the Hagbarth-Vallbo team initially used, is to compute the area under the curve. Indeed, if voltage is an instantaneous measurement of electrical activity in the nerve, adding up all the voltages over a time interval should return total activity. The main problem with this technique is that MSNA is very sensitive to electrode placement. Indeed, minuscule differences in electrode placement between subjects have large effects on the measured voltage, rendering comparisons difficult. A second quantification technique is then to subtract some moving average, or baseline, from the signal before proceeding to the integration. Unfortunately, this technique is sensitive to the signal-to-noise ratio (SNR), which is unknown, and again depends critically on the distance between the nerve fibre and the electrode tip, as well as on other electrical activity in the muscle.

The standard contemporary MSNA quantification technique relies on the fact that the signal exhibits activity in bursts (Fig. 1.6). It is then possible to count the number of bursts per minute, or per 100 heart beats, and to measure their individual height. While the height measurement technique has the same SNR problem as before, the number of bursts has been shown to be reliable and valid for comparisons between individuals [18].

MSNA does have limitations, the principal ones being that is it very susceptible to movement noise, requires hands-on apprenticeship, and trades off individual nerve (mal)function for general sympathetic outflow.

1.3.3 Seismocardiography

Seismocardiography (SCG) is the measurement by accelerometers of low frequency ($<$0.25 Hz) thoracic vibrations caused by the beating of the heart. The signal was first observed and described by Bozhenko in 1961 [21], and widely used since the sixties by Baevsky to monitor cosmonauts [22]. Its use was negligible outside Russia until 1991, when Zanetti and Salerno published a series of articles which characterized the signal using echocardiography [23], presented a case study about a 52 year-old woman with episodic dyspnea and chest tightness [24], and so on [25, 26]. It was first used on the International Space Station in 2002 [27] and continues to have an important presence there, due in part to the absence of earthly acceleration noise.

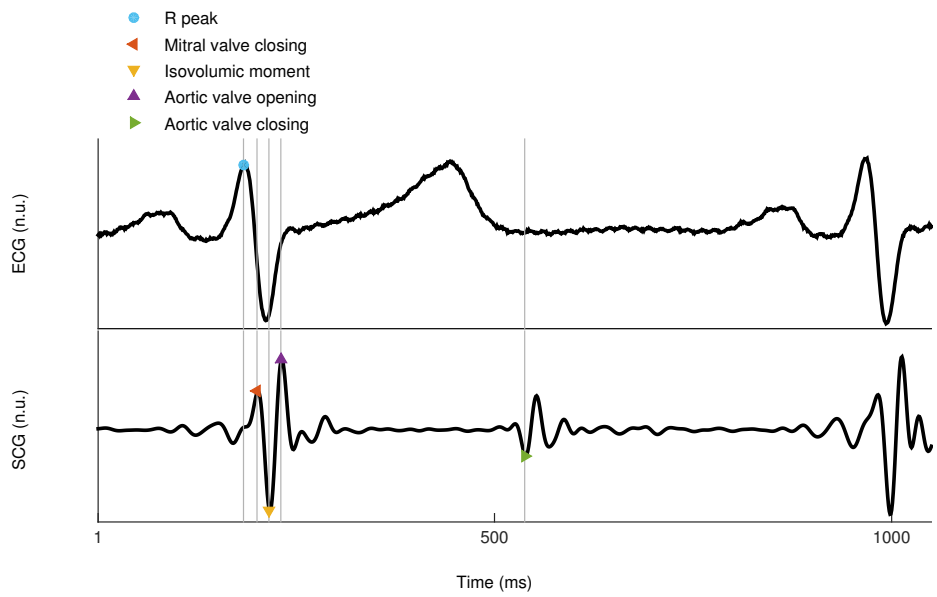

Figure 1.7: Example electrocardiogram (ECG) and seismocardiogram (SCG) with relevant fiducial points.

Peaks observed in SCG have been related to significant cardiac events, the main ones being mitral valve closing (MC), isovolumic moment (IM) and aortic valve opening (AO) during the systolic cycle, and aortic valve closure (AC) during the diastolic cycle (Fig. 1.7). The assignment of these fiducial points was based on concurrent echocardiogram analysis of SCG morphology [28, 29]. Precise cardiac mechanical timings that can only be obtained from SCG are critically dependent on accurate identification of these fiducial points [30, 31]. To this end, our team has been involved in the development of an algorithm capable of correct identification of ten IM peaks per five minutes of recording [32].

The modern-day ubiquity of accelerometers in wearable devices and smart phones opens the possibility of using SCG as an inexpensive source of data. Such devices have been used to accurately obtain heartbeat intervals [33, 34, 35], and the possibility of using SCG to obtain useful heart rate variability indices has been explored by us [36], and others [35, 37].

Research teams that use SCG are few, and to our knowledge, no general-public application for the signal has been developed. The fact remains that SCG is very susceptible to noise and present important variations between individuals, making the design of automatic annotation software difficult, but interesting.

1.3.4 Signal analysis

Signal analysis involves filtering and decomposition and is almost synonymous with Fourier analysis. The central idea is that, in the same way that any 2 dimensional vector can be seen as a sum of an x vector and a y vector, every time series can be seen as a sum of sine waves. This idea was first expressed by Joseph Fourier in 1822 [38].

Fourier analysis allows for the decomposition of a physiological signal into its constituent sine waves and enables us to see how much each frequency contributes to its make-up. There are then various ways to remove or modulate selected frequencies and reconstruct a modified, filtered signal.

There are a variety of ways to manipulate a signal using Fourier analysis, two of which are of particular relevance to this thesis.

The Hilbert transform, named after David Hilbert, was developed in the first half of the 20^{th} century [39]. As it pertains to this thesis, the Hilbert transform obtains the time-domain phase of the signal's constituting sine waves, and creates a weighted average of them according to their respective energy. This particular application will be discussed in detail in section 2.2, particularly in equation 2.2. In essence, it creates time-domain information from frequency-domain information in an intuitive, but brilliant way. The Hilbert transform is then able to attach notions of overall phase and frequency to signals which aren't periodic, concepts which end up being quite useful.

The continuous wavelet transform in its modern form was developed by Jean Morlet in the early 1980's [40], although it is largely based on previous work by Dennis Gabor published decades earlier [41]. A problem with the Fourier transform is that it loses all time-domain information once it leaps into the frequency-domain. A first naive solution to this problem would be to cut the original signal into regular intervals and perform a Fourier transform on each interval. One would then regain the ability to monitor changes over time. A second more subtle technique would be to cut the original signal in shorter intervals for higher frequencies, and longer intervals for lower frequencies, thus reflecting the higher frequencies' ability to have better time resolution. Gabor's contribution to these solutions was to modulate, or window, these intervals by using a bell curve. Morlet then set rules to smoothly and continuously preform this modulation over a range of frequencies.

The wavelet transform is capable of decomposing a signal into its constituent sine waves while retaining the ability show how this decomposition changes over time. Since its initial development, wavelet transform theorists have devised wavelets of various shapes which are adapted to specific situations.

1.4 Summary

The relationships between the signals mentioned above are intricate and can rarely be approached straightforwardly. The following chapters comprise a description of new ideas and techniques aimed specifically at obtaining quantifiable information from them to yield simple interpretations.

The first step was to establish the basis of different specific methods of signal analysis. To do this, the ability of different techniques to obtain accurate estimates of phase in physiological signals was examined. Phase is a property that is quite universal and can easily

be generalised to many physiological contexts. Furthermore, the ability of a technique to estimate phase informs us on its ability to estimate other useful quantities such as frequency and power.

In the two subsequent chapters, signal analysis techniques previously examined were applied to study in detail two sets of physiological data. In the first case, we use them to quantify the relationship between MSNA and diastolic arterial pressure (DAP). This relationship is described in terms of various timings, time delays, amplitudes, and strengths. Our techniques attempt to investigate these values as directly as possible in order to make interpretations simpler and clearer.

In the second case, techniques of signal analysis were used to design software capable of annotating SCG without user input. The goal is to automatically identify fiducial points on the signal. This process implements general techniques described in chapter 2 as well as other methods developed specifically to solve this problem. The ability of our annotations to return valid information was tested by comparing it to the gold standard electrocardiogram technique.

In chapter 5, the problem of the interpretation of seismocardiograms was approached from another angle, that of in-depth mathematical modelling. There exists various ways of correlating SCG fiducial points to other cardiovascular phenomena, either healthy or pathological. Our work concentrates on explaining the exact causes of these fiducial morphological characteristics. In this way, SCG is enabled to be analysed in terms of cardiac forces and movements as well as timings.

The four central chapters are written as self-contained papers and can each be read independently. For this reason, some figures are included in more than one chapter.

1.5 References

[1] S. Mayer, "Studien zur physiologie des herzens und der blutgefässe 6. abhandlung: Über spontane blutdruckschwankungen.," *Sitzungsberichte Akademie der Wissenschaften in Wien. Mathematisch-naturwissenschaftliche Classe, Anatomie*, vol. 74, pp. 281–307, 1876.

[2] C. Julien, "The enigma of Mayer waves: facts and models," *Cardiovascular research*, vol. 70, no. 1, pp. 12–21, 2006.

[3] C. Borst and J. M. Karemaker, "Time delays in the human baroreceptor reflex," *Journal of the autonomic nervous system*, vol. 9, no. 2, pp. 399–409, 1983.

[4] K.-E. Hagbarth and Å. Vallbo, "Pulse and respiratory grouping of sympathetic impulses in human muscle nerves," *Acta physiologica Scandinavica*, vol. 74, no. 1-2, pp. 96–108, 1968.

[5] C. Schroeder, J. Tank, M. Boschmann, A. Diedrich, A. M. Sharma, I. Biaggioni, F. C. Luft, and J. Jordan, "Selective norepinephrine reuptake inhibition as a human model of orthostatic intolerance," *Circulation*, vol. 105, no. 3, pp. 347–353, 2002.

[6] P. M. Stevens and L. E. Lamb, "Effects of lower body negative pressure on the cardiovascular system," *The American journal of cardiology*, vol. 16, no. 4, pp. 506–515, 1965.

[7] V. Convertino, "Lower body negative pressure as a tool for research in aerospace physiology and military medicine.," *Journal of gravitational physiology: a journal of the International Society for Gravitational Physiology*, vol. 8, no. 2, pp. 1–14, 2001.

[8] T. Hachiya, M. L. Walsh, M. Saito, and A. P. Blaber, "Delayed vasoconstrictor response to venous pooling in the calf is associated with high orthostatic tolerance to lbnp," *Journal of Applied Physiology*, vol. 109, no. 4, pp. 996–1001, 2010.

[9] W. H. Cooke, K. L. Ryan, and V. A. Convertino, "Lower body negative pressure as a model to study progression to acute hemorrhagic shock in humans," *Journal of Applied Physiology*, vol. 96, no. 4, pp. 1249–1261, 2004.

[10] R. F. Rea, M. Hamdan, M. P. Clary, M. J. Randels, P. J. Dayton, and R. G. Strauss, "Comparison of muscle sympathetic responses to hemorrhage and lower body negative pressure in humans," *Journal of Applied Physiology*, vol. 70, no. 3, pp. 1401–1405, 1991.

[11] C. A. Gilbert and P. M. Stevens, "Forearm vascular responses to lower body negative pressure and orthostasis.," *Journal of Applied Physiology*, vol. 21, no. 4, pp. 1265–1272, 1966.

[12] J. Hordinsky, U. Gebhardt, H. Wegmann, and G. Schäfer, "Cardiovascular and biochemical response to simulated space flight entry.," *Aviation, space, and environmental medicine*, vol. 52, no. 1, pp. 16–18, 1981.

[13] M. Romuald, Z. Mariusz, D. Artur, and R. Krzysztof, "Lbnp as useful tool for pilot candidates selection to the polish air force: a preliminary study.," *Journal of gravitational physiology: a journal of the International Society for Gravitational Physiology*, vol. 8, no. 1, pp. P147–8, 2001.

[14] K. Hyatt and D. West, "Reversal of bedrest-induced orthostatic intolerance by lower body negative pressure and saline," *Aviation, Space, and Environmental Medicine*, vol. 48, no. 2, pp. 120–124, 1977.

[15] E. Lawrence and M. Stevens, "Influence of lower body negative pressure on the level of hydration during bed rest," *Aerospace Medicine*, p. 1145, 1965.

[16] S. Lee, B. S. Bennett, A. R. Hargens, D. E. Watenpaugh, R. E. Ballard, G. Murthy, S. R. Ford, and S. M. Fortney, "Upright exercise or supine lower body negative pressure exercise maintains exercise responses after bed rest," *Medicine and Science in Sports and Exercise*, vol. 29, no. 7, pp. 892–900, 1997.

[17] H. Torebjo, R. Hallin, *et al.*, "Identification of afferent c units in intact human skin nerves," *Brain Research*, vol. 67, no. 3, pp. 387–403, 1974.

[18] Å. B. Vallbo, K.-E. Hagbarth, and B. G. Wallin, "Microneurography: how the technique developed and its role in the investigation of the sympathetic nervous system," *Journal of Applied Physiology*, vol. 96, no. 4, pp. 1262–1269, 2004.

[19] G. Sundlöf and B. G. Wallin, "The variability of muscle nerve sympathetic activity in resting recumbent man," *The Journal of Physiology*, vol. 272, no. 2, pp. 383–397, 1977.

[20] G. Sundlöf and B. Wallin, "Human muscle nerve sympathetic activity at rest. relationship to blood pressure and age," *The Journal of Physiology*, vol. 274, no. 1, pp. 621–637, 1978.

[21] B. S. Bozhenko, "Seismocardiography–a new method in the study of functional conditions of the heart," *Terapevticheskii Arkhiv*, vol. 33, pp. 55–64, 1961.

[22] R. M. Baevsky, A. D. Egorov, and L. A. Kazarian, "The Method of Seismocardiography," *Kardiologiia*, vol. 18, pp. 87–9, Jan. 1964.

[23] J. Zanetti, M. Poliac, and R. Crow, "Seismocardiography: waveform identification and noise analysis," in *Computers in Cardiology 1991, Proceedings.*, pp. 49–52, IEEE, 1991.

[24] D. M. Salerno, J. M. Zanetti, L. A. Green, M. R. Mooney, J. D. Madison, and R. A. Van Tassel, "Seismocardiographic changes associated with obstruction of coronary blood flow during balloon angioplasty," *The American Journal of Cardiology*, vol. 68, no. 2, pp. 201–207, 1991.

[25] M. Poliac, J. Zanetti, and D. Salerno, "Performance measurements of seismocardiogram interpretation using neural networks," in *Computers in Cardiology 1991, Proceedings.*, pp. 573–576, IEEE, 1991.

[26] J. M. Zanetti and D. M. Salerno, "Seismocardiography: a technique for recording precordial acceleration," in *Computer-Based Medical Systems, 1991. Proceedings of the Fourth Annual IEEE Symposium*, pp. 4–9, IEEE, 1991.

[27] V. M. Baranov, R. M. Baevsky, J. Drescher, and J. Tank, "Investigations of the cardiovascular and respiratory systems on board the international space station: Experiments puls and pneumocard," in *IAF abstracts, 34th COSPAR Scientific Assembly*, p. 152, 2002.

[28] R. Crow, P. Hannan, D. Jacobs, L. Hedquist, and D. Salerno, "Relationship between seismocardiogram and echocardiogram for events in the cardiac cycle," *American journal of Noninvasive Cardiology*, vol. 8, no. 39, pp. 39–46, 1994.

[29] K. Tavakolian, A. Blaber, B. Ngai, and B. Kaminska, "Estimation of hemodynamic parameters from seismocardiogram," in *Computing in Cardiology*, (Belfast), pp. 1055–1058, 2010.

[30] K. Tavakolian, G. A. Dumont, G. Houlton, and A. P. Blaber, "Precordial vibrations provide noninvasive detection of early-stage hemorrhage," *Shock*, vol. 41, no. 2, pp. 91–96, 2014.

[31] D. M. Salerno and J. Zanetti, "Seismocardiography for monitoring changes in left ventricular function during ischemia.," *CHEST Journal*, vol. 100, no. 4, pp. 991–993, 1991.

[32] F. Khosrow-khavar, K. Tavakolian, A. Blaber, J. M. Zanetti, R. Fazel-Rezai, and C. Menon, "Automatic annotation of seismocardiogram with high frequency precordial accelerations," *IEEE Journal of Biomedical and Health Informatics*, vol. 19, no. 4, 2014.

[33] M. Di Rienzo, E. Vaini, B. Bruno, P. Castiglioni, P. Lombardi, G. Parati, C. Lombardi, P. Meriggi, and F. Rizzo, "Wearable seismocardiography: Towards the beat-to-beat assessment of cardiac mechanics during sleep in microgravity," *2014 8th Conference of the European Study Group on Cardiovascular Oscillations, ESGCO 2014*, pp. 239–240, 2014.

[34] M. Di Rienzo, E. Vaini, P. Castiglioni, P. Lombardi, P. Meriggi, and F. Rizzo, "A Textile-Based Wearable System for the Prolonged Assessment of Cardiac Mechanics in Daily Life," in *IEEE EMBC*, pp. 6896–6898, 2014.

[35] J. Ramos-Castro, J. Moreno, H. Miranda-Vidal, M. a. García-González, M. Fernández-Chimeno, G. Rodas, and L. Capdevila, "Heart rate variability analysis using a seismocardiogram signal.," *Conference proceedings: Annual International Conference of the IEEE Engineering in Medicine and Biology Society. IEEE Engineering in Medicine and Biology Society. Conference*, vol. 2012, pp. 5642–5, 2012.

[36] A. Laurin, A. Blaber, and K. Tavakolian, "Seismocardiograms return valid heart rate variability indices," in *Computing in Cardiology Conference*, pp. 413–416, 2013.

[37] M. J. Tadi, E. Lehtonen, T. Koivisto, M. Pankaala, A. Paasio, and M. Teras, "Seismocardiography: Toward heart rate variability (hrv) estimation," in *Medical Measurements and Applications (MeMeA), 2015 IEEE International Symposium on*, pp. 261–266, IEEE, 2015.

[38] J. Fourier, *Theorie analytique de la chaleur, par M. Fourier*. Chez Firmin Didot, père et fils, 1822.

[39] G. H. Hardy, J. E. Littlewood, and G. Pólya, *Inequalities*. Cambridge University Press, 1952.

[40] A. Grossmann and J. Morlet, "Decomposition of Hardy functions into square integrable wavelets of constant shape," *SIAM journal on mathematical analysis*, vol. 15, no. 4, pp. 723–736, 1984.

[41] D. Gabor, "Theory of communication. part 1: The analysis of information," *Journal of the Institution of Electrical Engineers-Part III: Radio and Communication Engineering*, vol. 93, no. 26, pp. 429–441, 1946.

Chapter 2

Quantitative comparison of three phase estimation techniques and a guide to their practical use in physiology

> Victory in the pits is almost as rewarding as the methods I use to achieve it.
>
> *MTG, Sadistic Hypnotist*

2.1 Introduction

Homeostasis in biological systems is maintained by negative feedback loops. This feedback system contributes to the creation of oscillations in the corresponding physiological signals. For example, oscillations exist in heart rate [1], spontaneous vasomotion of arteries [2, 3], electrical activity of skeletal muscle [4], and circadian rhythms in hormone levels [5]. The key variables that characterize an oscillation are its amplitude, frequency, and phase. Of interest is phase, as it determines the progress of one oscillatory cycle at a particular time.

Phase analysis is particularly relevant to the study of the relationship between a pair of associated signals. The detection of relationships between physiological signals can aid the understanding of the integrated function of multiple parts of a given system. *A priori* to studying these phase relationships, however, one should be able to confidently understand and estimate the phase itself. There are multiple techniques that are routinely employed for estimating the phase of signals. However, it is unclear whether these approaches produce

equivalent results or whether some methods may be preferable for particular physiological applications. So far no technique has been accepted as a gold standard.

The oscillations of physiological signals contain information about a system's behaviour and interactions occurring within it. If a signal sufficiently resembles a periodic function, this information can be extracted mathematically using frequency analyses. It bears mentioning that in such cases, as in the signals analysed in this study, the term frequency is used even if they exhibit what can be more precisely described as *pseudo-frequency*, as they are never precisely periodic.

When two parts of a physiological system interact, oscillations in the signals arising from each part adjusts in response to changes in the other. This has been shown in networks in the brain [6], the physiological origin of pathological human tremors [7], the relationship between blood pressure and sway patterns in human standing [8], blood flow in adjacent nephrons [9], and glycolytic oscillations in cells that receive a periodic nutrient supply [10]. In these systems, phase and phase difference can be used either themselves or as a means to obtain phase lock indices or time delays. Monitoring free-running physiological signals only allows investigators to determine synchronicity between them. Without externally perturbing such signals, coincidental synchrony and physical coupling cannot be distinguished [11].

The power spectrum of a signal gives information about the degree to which periodic components are present, and at what frequency the oscillations occur. When there are strong oscillations present in a signal, further analysis can be conducted. Analysis, such as estimating phase, of data that does not contain oscillatory signals of sufficient power is not valid.

The phase of a physiological signal represents certain aspects of the physical state of the system being measured, and therefore it is interpreted differently depending on context. For example, in the case of a blood pressure time series, phase can be used as a normalized indicator of arterial contraction and relaxation. In the case of the position of the foot of a pedalling cyclist, phase indicates which part of a particular pedal cycle is present at a particular time. Each cycle (Fig. 2.1, top) increases phase by 2π radians (Fig. 2.1, middle). Since the circumference of a unit circle is 2π, phases that differ from one another by a multiple of 2π represent the same physiological state. In this study, the convention by which phase is visualised by *wrapping* it from $-\pi$ to π (Fig. 2.1, bottom) was used.

Because phase is defined on a circle, errors arise upon application of arithmetic statistics to it. This fact is illustrated by the following example: the arithmetic mean of the angles $\pi/4$ and $7\pi/4$ is π. However, since $7\pi/4$ is the same as $-\pi/4$ when plotted on a circle, the circular mean is 0. For this reason, circular statistics are used when dealing with phase. A good resource for circular statistics is found in [12].

The goals of this study were twofold: the first was to compare the performances of three different techniques of phase estimation: (i) the Hilbert transform; (ii) wavelet transform; and (iii) peak detection, *in silico*. The second was to apply each technique to four different

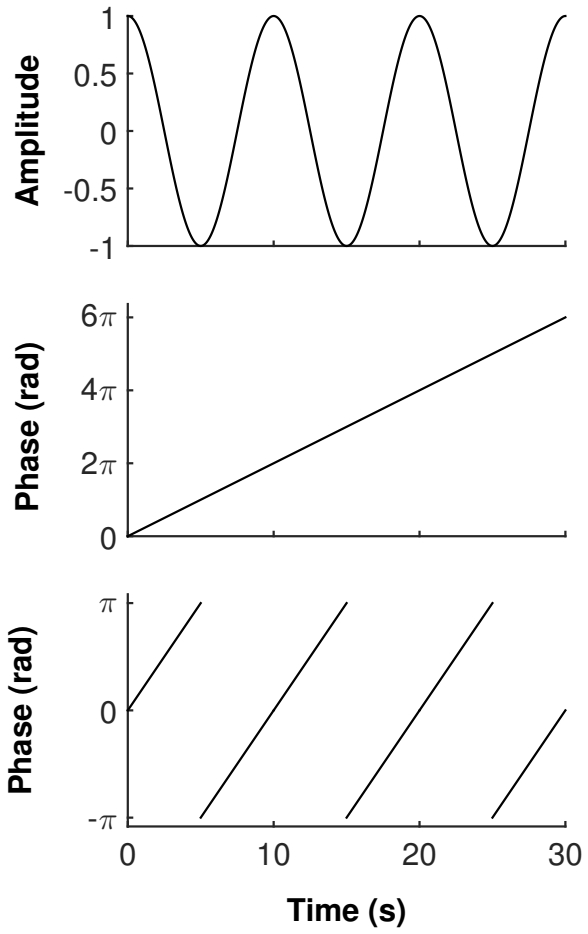

Figure 2.1: Example cosine function and its corresponding phase. There are three cycles of the cosine wave (**top**), resulting in a total increase of 6π radians of phase (**middle**). The **bottom** panel shows the same phase wrapped from $-\pi$ to π.

types of experimentally collected *in vivo* data and compare the interpretations that arose consequently.

Each technique was tested to observe whether it led to the same physiological conclusions for each type of data. It is clear from past work that the Morlet wavelet and Hilbert techniques return statistically similar results for signals that have a previously defined narrow frequency band [13, 14]. However, it is unclear how well these techniques compare to the computationally simpler peak detection method. Because measurement noise and physiological noise are the primary sources of interference with phase estimators, each technique was tested for its robustness to noise. The computing time of these three techniques was also compared.

Although it is clear that phase estimations often lead to phase difference quantifications such as phase lock or synchrony indices, it is not within the scope of this study to discuss the value of these indices. Rather, under the assumption that any phase difference calculation will benefit from more accurate phase estimation, only the variables necessary to their computation were examined.

The limits of the conditions for which the techniques are similar were determined, and a clear "if-then" decision tree to guide users to select the best technique for their signal(s) of interest is presented.

2.2 Methods

Each signal was filtered using a forwards-backwards 6^{th} order Butterworth bandpass filter. This filter design, particularly in its application in one time-direction and then the other, was chosen to minimize its effect on phase. The band was determined case-by-case and will be described in detail in the relevant sections. Phase slips of $\pm 2\pi$ were removed from phase difference time series, for clarity of presentation. All data synthesis and analysis was performed using Matlab (r2014b, The Mathworks, Natick, MA, USA) and statistical comparisons were performed using SPSS (v22, IBM, Armonk, NY, USA).

2.2.1 Estimating phase

This section describes the wavelet transform, Hilbert transform, and peak detection techniques.

i *The Morlet wavelet transform* is a Gaussian-windowed Fourier transform. The Morlet wavelet of order six, used in this study, is a cosine wave modulated by a Gaussian of such width that 6 periods fit in 95% of its area. The wavelet transform quantifies the degree to which a wavelet represents the given signal. It then shifts the wavelet in time and frequency, to generate the spectral density of the signal over time.

For example, for a cosine wave of frequency α during a certain time, it is expected that the magnitude of its wavelet transform at that time and frequency will be relatively high. Conversely, the wavelet transform of a random noisy signal would have a relatively low magnitude for all times and frequencies. For a great introduction on the subject see [15], and [16]. The software used for these analyses is freely available (`http://paos.colorado.edu/research/wavelets/software.html`).

In this study, phase was determined for the the frequency α_{max} with the highest power for every time point t_i. Phase was computed as

$$\phi(t_i) = \tan^{-1} \frac{\mathrm{im}\Big(s_w(\alpha_{max}, t_i)\Big)}{\mathrm{re}\Big(s_w(\alpha_{max}, t_i)\Big)}, \tag{2.1}$$

where s_w is the wavelet transform of the signal s.

ii *The Hilbert transform* uses the Fourier transform to create a 90^o phase shift filter. As it pertains to this study, it obtains phase information by using the Fourier power to compute a weighted average of the phases in the frequency domain

$$\phi = \frac{1}{\sum_\alpha |s_F(\alpha)|} \sum_\alpha |s_F(\alpha)| \cdot \tan^{-1} \frac{\mathrm{im}\Big(s_F(\alpha)\Big)}{\mathrm{re}\Big(s_F(\alpha)\Big)}, \tag{2.2}$$

where s_F is the Fourier transform of the signal s.

iii *The peak detection* algorithm identifies all local maxima on the filtered signal. A local maximum is defined here as simply as possible, as any point higher than both the directly previous point and directly successive point. at least p_1 away from each other in time, where p_1 is the period associated with the upper cutoff frequency of the bandpass filter. The rationale behind the choice of this p_1 is analogous to that for the choice of f_1, that is, it is chosen to represent the smallest physiologically possible distance between two successive peak events. If t_a and t_b are times of two successive peaks, then the phase ϕ between these peaks is defined as

$$\phi(t) = 2\pi \frac{t - t_a}{t_b - t_a}.$$

This phase is then wrapped to $(-\pi, \pi]$.

The main distinction of the peak detection technique is that it is not limited by the time-frequency uncertainty principle. When using frequency analyses such as the Hilbert or wavelet transforms, It is impossible to reduce the time spread and frequency spread

simultaneously. The peak detection technique extrapolates phase information from time information under the assumption that measurable rises and drops occur in a strictly known frequency band.

2.3 *In silico analyses*

The three phase-estimation techniques were compared *in silico*. The main goal was to compare the accuracy of these techniques with respect to signal-to-noise (SNR) ratio, but the computing time of each technique was also taken into account. The *in silico* data were designed to resemble the *in vivo* physiological data presented later.

A time series was created with a frequency f that changed randomly in a normal distribution $f(\mu, \sigma)$ around a central frequency $\mu = 0.1$ Hz, and standard deviation $\sigma = 0.01$ Hz. The time series were defined by parts, every part being a single-cycle cosine wave. They were designed to change frequency every cycle, have a sample frequency of 100 samples/s, and create 7 minutes of signal (Fig. 2.2A). The 100 Hz sample frequency was chosen to exceed the Nyquist frequency while striking a balance between maximizing temporal resolution and minimizing computation time.

The true phase was computed to be the straight line going from 0 to 2π between each successive peak, and then wrapped to $(-\pi, \pi]$.

Noise was added to each simulation time series for signal-to-noise ratios SNR $\in [-20, 5]$ dB, in 1 dB increments. These signals were then passband filtered to [0.02, 0.3] Hz. At each SNR, the phase was estimated using the three techniques and the difference between the true phase and estimated phase was computed. This process was repeated 100 times (Fig. 2.3; Table 2.1). Computation time was measured for each trial (Table 2.2).

Table 2.1: Difference between mean estimated phase and true phase of a synthetic sine wave. The difference was computed at each level of SNR from -20 to 5 dB, and this was repeated 100 times.

SNR (dB)	Wavelet	Hilbert	Peak Det.
-20	-0.3 ± 0.1	0.01 ± 0.01	0.004 ± 0.002
-15	0.06 ± 0.05	0.03 ± 0.01	0.002 ± 0.001
-10	-0.011 ± 0.010	-0.002 ± 0.004	0.003 ± 0.001
-5	0.003 ± 0.001	0.006 ± 0.002	0.002 ± 0.001
0	-0.002 ± 0.001	-0.005 ± 0.063	0.0030 ± 0.0003
5	-0.002 ± 0.001	0.007 ± 0.056	0.0020 ± 0.0002
∞	0.002 ± 0.001	0.0060 ± 0.0002	0.0010 ± 0.0001

Mean $\pm$ standard deviation (rad)

$^*p < 0.05$ compared to Hilbert and peak detection

To determine differences in the precision of each technique, the difference between mean and squared difference at each SNR was tested with analysis of variance (ANOVA) with

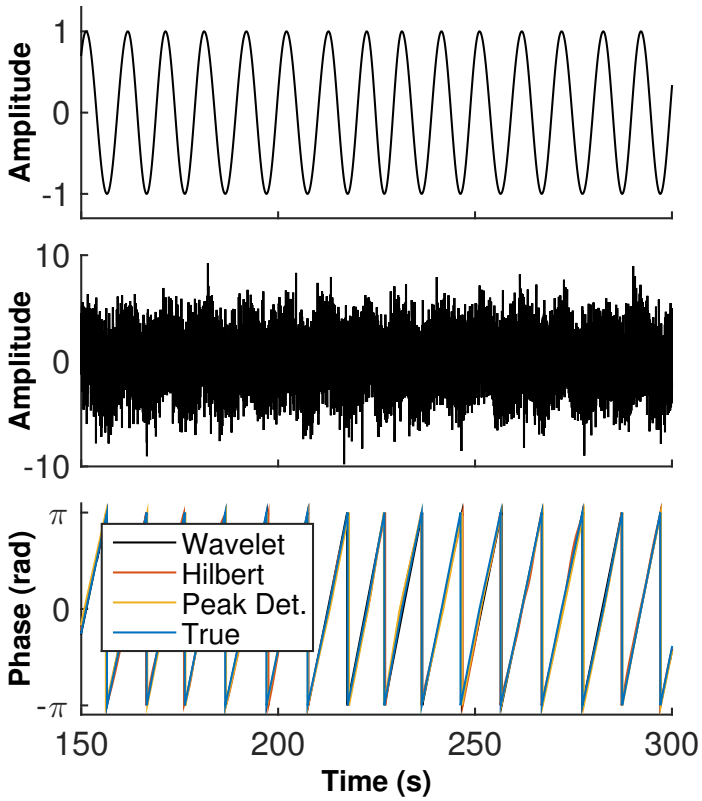

Figure 2.2: Example signals and phase estimates, *in silico*. **Top**: Clean signal with central frequency $\mu = 0.1$ Hz, and standard deviation $\sigma = 0.01$ Hz. Signal-to-noise ratio (SNR) $= \infty$. **Middle**: A noisy signal. SNR = -10 dB. **Bottom**: Wrapped phase estimates for Hilbert, wavelet, and peak detection techniques at SNR $= -10$ dB.

Table 2.2: Mean computation time for each technique of phase estimation for each trial with SNR ranging from -20 to 5 dB, with 100 simulations.

Method	Time (s)
Wavelet	1.7288 ± 0.0180
Hilbert	0.0877 ± 0.0314*
Peak Det.	0.1364 ± 0.0671*

Mean $\pm$ standard deviation (rad)
*$p < 0.05$ compared to wavelet

Sidak post hoc tests. At SNR where the maximum absolute difference was less than 0.1 radians, this difference was not considered to be of potential physiological relevance. Therefore these values were not included in our statistical comparison of the techniques. Squared differences were not different between the Hilbert and peak detection techniques at any SNR, while the wavelet technique was different from the others when SNR was less than -9 dB.

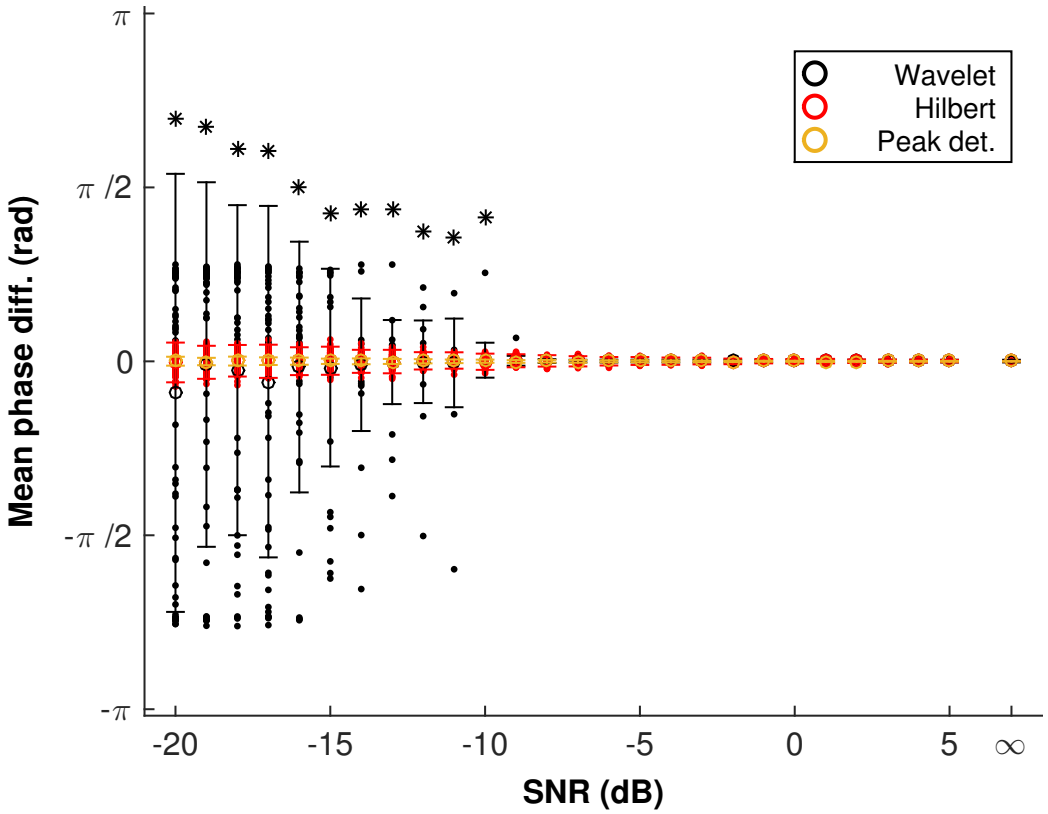

Figure 2.3: The effect of added Gaussian white noise on the accuracy of each phase estimator. At each signal-to-noise ratio (SNR), the difference between true phase and estimated phase is shown as a solid point for each of the 100 trials. The mean difference is shown as an open circle and error bars are 1.96 × standard deviation. *Mean wavelet phase difference is significantly different from both other techniques' mean ($p<0.01$).

Noise in physiological signals can either come from data acquisition or be intrinsic to the system itself. While the former can be estimated using standard techniques, estimates for the latter are usually much harder to obtain. In a blood pressure measurement, for example, an unreported involuntary muscle contraction in a subject could create noise as a temporary oscillation in a relevant frequency band, which would be difficult to quantify. While an SNR of -9 dB is very low, some types of physiological data can be that noisy and still contain relevant information [17].

2.4 *In vivo analyses*

The three phase estimation techniques were applied to four sets of physiological data. For each set, the acquisition and formatting techniques are described. Results are presented for each data set and interpreted in terms of phase estimation and physiology. The animal experiments were conducted according to the guidelines set forth by the Canadian Council on Animal Care and approved by the Animal Care Committee of Simon Fraser University.

Human experiments were conducted in accordance with the Declaration of Helsinki and with approval from the Simon Fraser University Office of Research Ethics.

2.4.1 Human systolic blood pressure and RR intervals

The phase difference between systolic blood pressure and RR intervals is used to estimate the time delay of efferent cardiac baroreflex control. Ten healthy subjects (6 males) ages 20-57, were tested in the supine position. Blood pressure and electrocardiogram (ECG, lead II configuration) were recorded using the Finometer (Finapres Medical Systems, Amsterdam, Netherlands) for five minutes at a sample frequency of 1 kHz. R waves and systolic blood pressure (SBP) peaks were identified, RR intervals were computed, and the resulting time series were resampled at 5 Hz. SBP and RR interval time series were filtered with a passband of [0.04, 0.15] Hz to isolate low-frequency variability [1]. Oscillations in this band are present in both RR intervals and SBP, correspond to each other, and are called Mayer waves in SBP [2]. The phase of both signals was computed using the three techniques (Fig. 2.4).

For each subject, the circular mean and standard deviation of phase difference between SBP and RR intervals was computed. The mean phase difference over all participants was 1.38 ± 0.16 rad for the wavelet technique, -1.29 ± 0.2 rad for the Hilbert technique, and -1.1 ± 0.44 rad for the peak detection technique (Fig. 2.5). For the interpretation of cardiac baroreflex phase difference, all three approaches were equivalent.

2.4.2 Human nasal temperature and RR intervals

Changes in thoracic pressure caused by respiration affect RR intervals, eliciting respiratory sinus arrhythmia. This can be investigated by measuring the phase difference between nasal temperature (NT) and RR intervals. Seventeen healthy participants (7 males) ages 18-51, with no experience in meditation were tested. Participants were seated, instructed to close their eyes, and to remain motionless and silent for 20 minutes. They were further instructed to regulate their attention on the sensations of breathing without willfully altering its rate or depth.

Nasal temperature and ECG (lead II configuration) were recorded using the Pneumocard [18]. RR interval time-series were obtained from the ECG in the same manner as described above. NT was resampled to 5 Hz and used to determine breathing rate. The phase of both signals was computed using the three techniques (Fig. 2.6).

In this case, the two time series (NT and RR intervals) were filtered to a passband of $[0.15, 0.4]$ Hz to isolate high-frequency variability [1]. Heart rate variability in this high-frequency range is caused by respiratory sinus arrhythmia and the central frequency represents the respiratory frequency [19].

For each subject, the circular mean and average standard deviation of phase difference between NT and RR intervals was computed. The mean phase difference was -0.7 ± 0.37

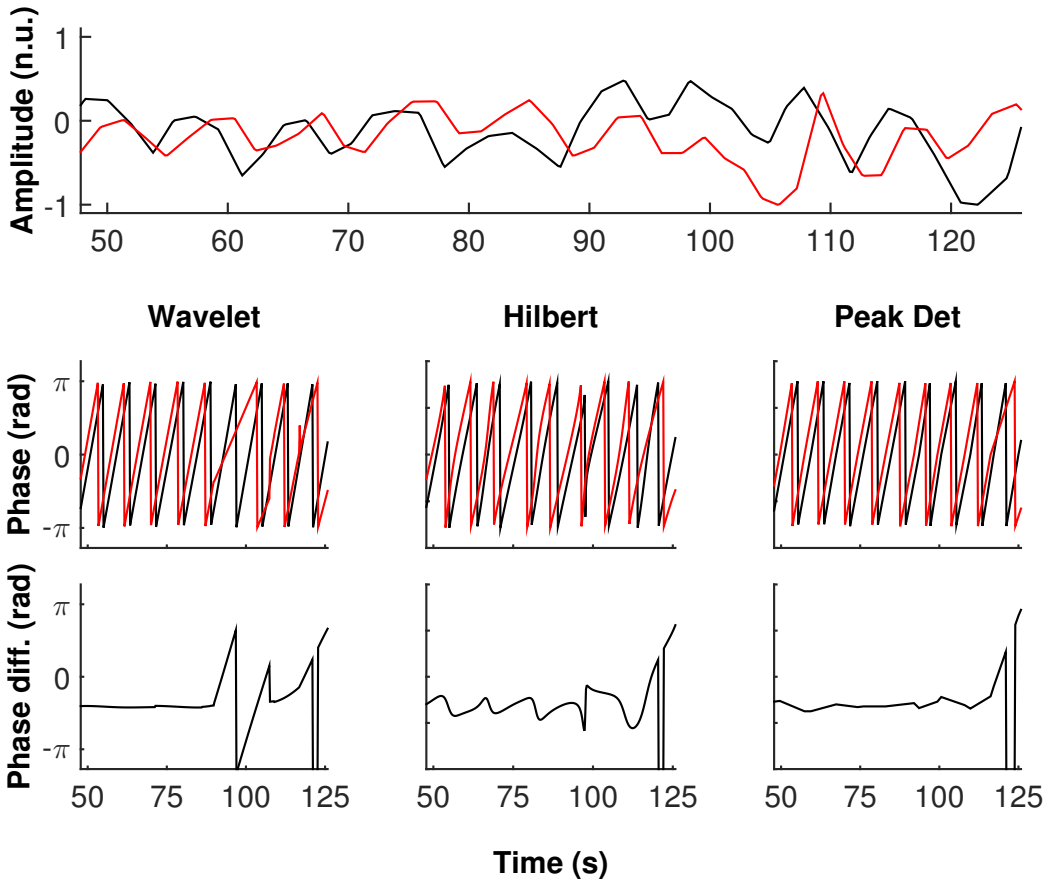

Figure 2.4: **Top:** Example unfiltered RR interval (red) and systolic blood pressure (SBP, black) time series. Static oscillations in SBP create analogous oscillations in RR intervals. Normalised units were obtained by subtracting the mean and dividing the resulting maximum amplitude. **Middle:**The phase of SBP and RR intervals are shown as calculated by each technique. **Bottom:** Phase difference between the two time series. The results that are returned by all three techniques show similar patterns.

rad for the wavelet technique, -0.73 ± 0.35 rad for the Hilbert technique, and -0.81 ± 0.48 rad for the peak detection technique (Fig. 2.7).

The data from this study allowed the investigation of a limitation of the three phase estimation techniques. It is well known that respiratory sinus arrhythmia has a complex relationship with both frequency of breathing and the act of consciously modulating breathing rate and depth [20, 21]. The coupling in phase between rate of breathing and RR intervals breaks down as breathing rate decreases. This is due in part to an interaction with baroreflex mediated oscillations occurring at frequencies around 0.1 Hz. For this reason, the standard band pass filter was used, set to exclude breathing rates slower than 0.15 Hz.

The mean rate of breathing was computed for each subject by identifying the peaks of the NT graphs, using a technique analogous to the peak detection phase estimation technique, and taking the inverse the difference in time from one peak to the next (Fig. 2.8).

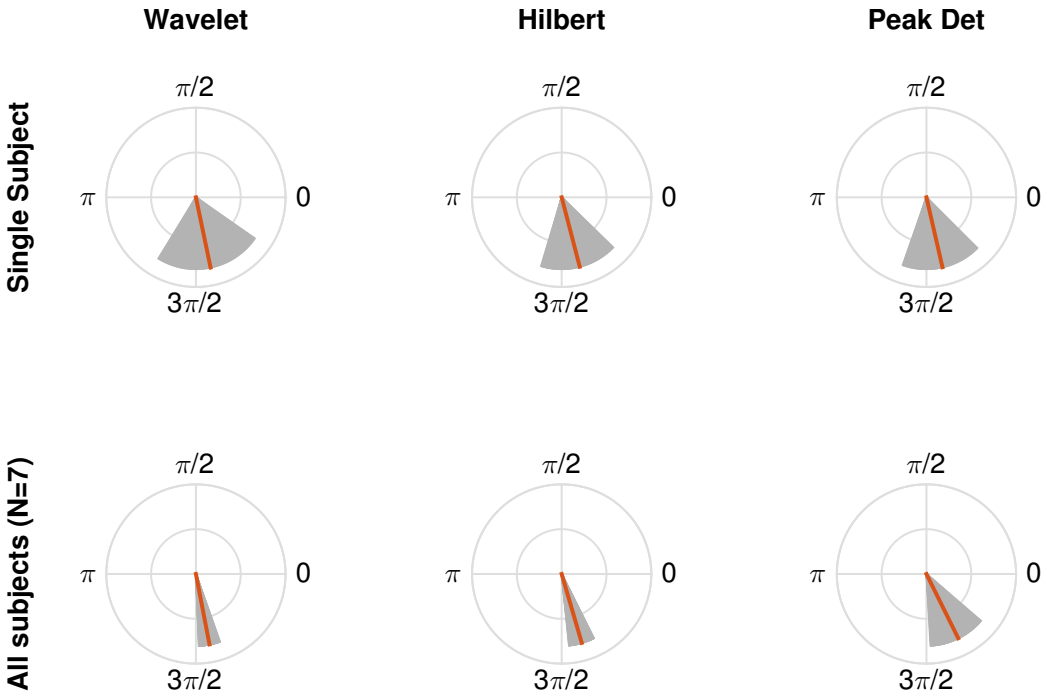

Figure 2.5: **Top:** Example circular mean (red line) ± circular standard deviation (grey) of phase difference between RR intervals and systolic blood pressure for the three techniques of interest in one individual. **Bottom:** Group values of mean (red) of circular means ($n = 7$) ± circular standard deviations (grey) of phase difference between RR intervals and systolic blood pressure.

To illustrate general trend, the data was fit with an exponential using the least-squares method, which returned absolute mean errors smaller than 0.16 rads. In all three plots, the data shows a trend of increased standard deviation for decreased rate of breathing. For interpretation of phase differences associated with respiratory sinus arrhythmia, all three approaches are equivalent.

2.4.3 Human electromyograms and muscle-tendon length

Mechanical function largely depends on the timing of muscle activation relative to muscle lengthening or shortening. The phase of muscle activation has emerged as an important variable by which the nervous system can regulate mechanical performance of muscles during locomotion. One male cyclist was tested on an indoor cycle ergometer (Indoor Trainer, SRM, Julich, Germany). Limb kinematics were collected using an optical motion capture system (Certus Optotrak, NDI, Waterloo, Canada). LED markers were placed on the pelvis, greater trochanter, thigh segment (triad), femoral lateral epicondyle, shank (triad) lateral malleolus, calcaneus, metatarsophalangeal joint, and the bike pedal of the left and right limbs. Participants pedalled at a cadence of 80 revolutions per minute. Time varying medial gastrocnemius (MG) muscle-tendon unit lengths were calculated using a subject

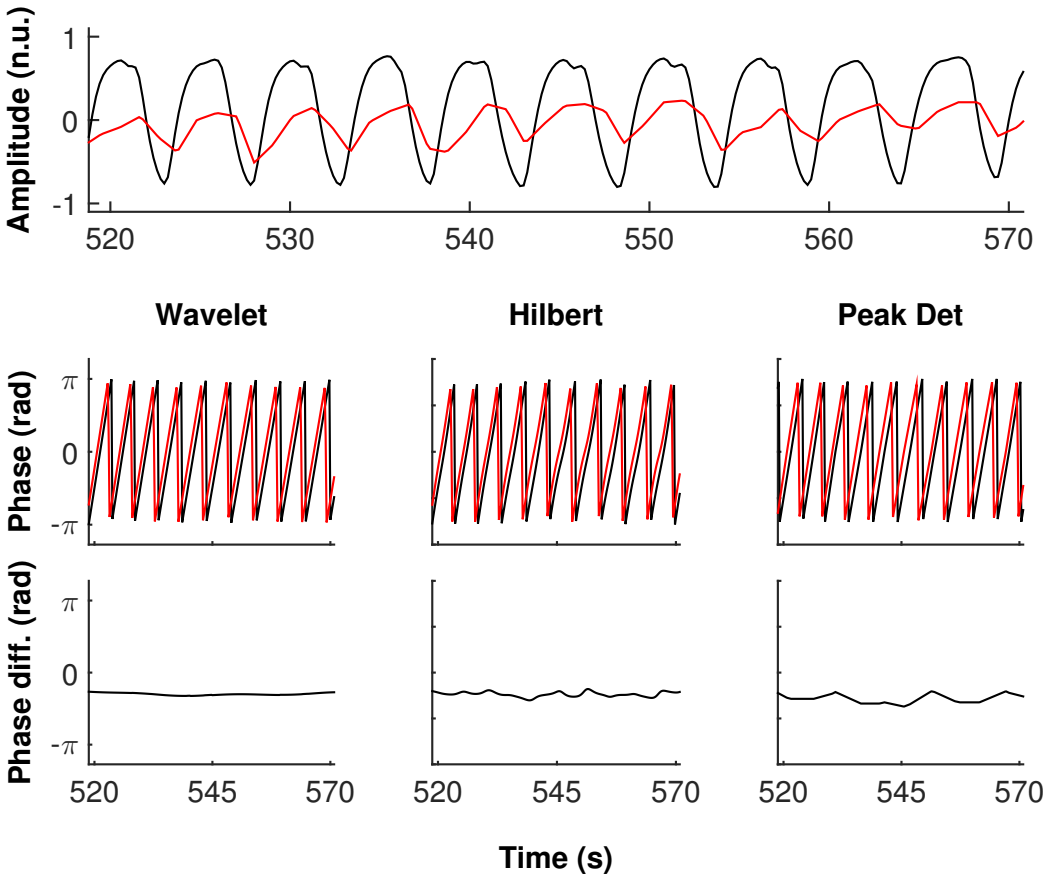

Figure 2.6: **Top:** Example unfiltered nasal temperature (NT, red) and RR interval (black) time series. Through various pathways, breathing creates oscillations in RR intervals. Normalised units were obtained by subtracting the mean and dividing by the resulting maximum amplitude. **Middle:** The phase of NT and RR intervals are shown as calculated by each technique. **Bottom:** Phase difference between the two time series.

specific scaled musculoskeletal model (pre-defined muscle paths from cadaveric studies) and experimentally collected joint kinematics in the biomechanics simulation software OpenSim [22].

Surface EMG was recorded during the cycling conditions from the MG using bipolar Ag/AgCl electrodes (10 mm diameter, 21 mm spacing) and Biovision amplifiers (Biovision, Wehrheim, Germany). Electrodes were placed in the mid-region of the muscle bellies after the hair had been removed and the skin cleaned with isopropyl alcohol solution. EMG was sampled at 2000 Hz and recorded using a 16-bit analogue-to-digital convertor (USB-6210, National Instruments, Austin, TX, USA). EMG signals were quantified by their intensities during each pedal revolution. The intensity is a close approximation to the power of the signal and was calculated across the frequency band $[10, 450]$ Hz using an EMG-specific wavelet analysis [23]. The LED marker positions of the left pedal was used to synchronize the EMG intensities for each pedal revolution, with the motion capture data. All 14-second

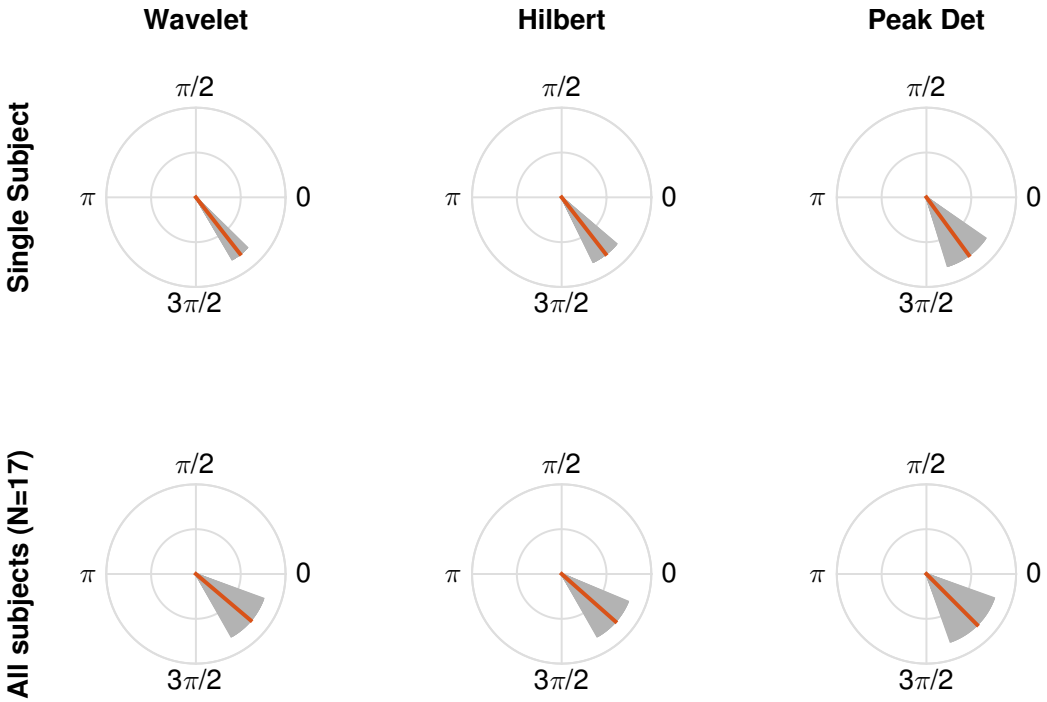

Figure 2.7: **Top:** Example circular mean (red line) ± circular standard deviation (grey) of phase difference between nasal temperature (NT) and RR intervals for the three techniques of interest in one individual. **Bottom:** Group circular mean (red) and standard deviation (grey) of circular means (n =17) of phase difference between NT and RR intervals. All pairs of distributions were not statistically different ($p > 0.54$).

time series were downsampled to 100 Hz and filtered to isolate the frequency of pedalling using a passband of $[1.0, 1.5]$ Hz.

An individual muscle can act as power generating motor if active while shortening, an energy transmission element if active while isometric, or an energy absorbing brake if active while lengthening [24]. Our results display a stable phase lag between muscle activity (EMG intensity) and the onset of muscle-tendon unit shortening (Fig. 2.9). The mean phase difference was -0.7 ± 0.37 rad for the wavelet technique, -0.73 ± 0.35 rad for the Hilbert technique, and -0.81 ± 0.48 rad for the peak detection technique (Fig. 2.10).This suggests that the MG is largely active during muscle lengthening, thus acts as a brake to absorb energy. The MG is likely active during this period to avoid knee hyperextension and excessive ankle dorsiflexion during pedal downstroke and allow for effective force transfer to the pedal.

For interpretation of phase difference between muscle activity and onset of muscle shortening, all three approaches were equivalent.

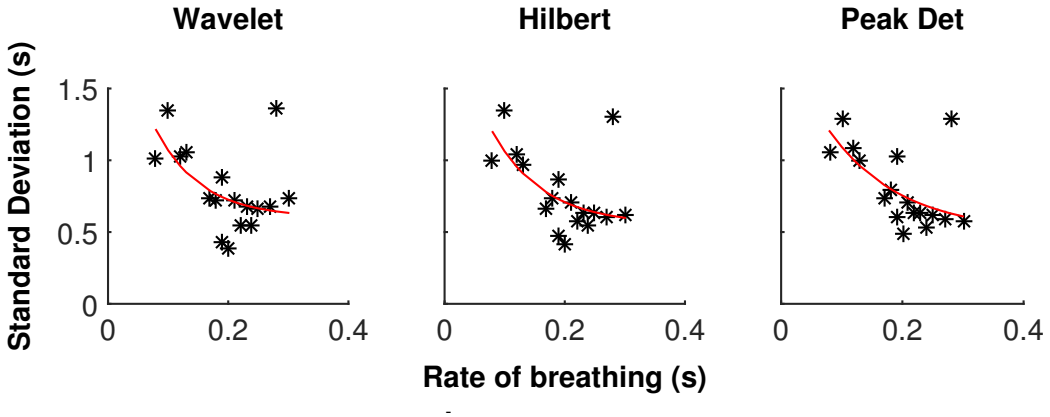

Figure 2.8: For each subject, circular standard deviation of the phase difference between nasal temperature and RR intervals *vs* their rate of breathing. To illustrate general trend, exponential functions were fitted to the data (red).

2.4.4 Synchrony of renal autoregulation

It has been shown previously that laser speckle perfusion imaging (LSCI) can detect physiological signals including those associated with renal autoregulation [9], and that these dynamics can be segmented into regions that are phase-synchronised [25, 9]. Autoregulation is mediated in part by the classic myogenic response (MR) of smooth muscle, where increased intraluminal pressure causes vasoconstriction, and decreased pressure causes vasodilation. Male Long-Evans rats ($n = 7$) were anesthetised with isoflurane and their left kidney was exposed via a subcostal flank incision. Cortical perfusion was monitored for 5 minutes on approximately 1/3 of the visible surface of the kidney with LSCI using a Moor full-field laser speckle perfusion imager (Moor Instruments, Axminster, UK). Three regions of interest (ROI) were selected on the surface. ROI1 and ROI2 were close to each other, separated by 140 μm while ROI3 was located approximately 1.2 mm away from ROI1. Perfusion time series were extracted from each ROI. Each 25 Hz time series was downsampled to 1 Hz and band pass filtered to isolate the $[0.09, 0.32]$ Hz frequency range associated with MR in rats. The phase of each ROI was computed using the three techniques described perviously. Then, the difference in phase was calculated between ROI1 and ROI2 and between ROI1 and ROI3. Because detecting synchrony between two signals is more dependent on the constant temporal relationship between signals rather than the magnitude of the mean, the circular mean as well as circular standard deviation of the phase difference between each pair of ROI were computed.

Renal surface perfusion from three ROI in one rat is shown in Fig. 2.11. The data show that when two ROI are close to each other, the dynamics associated with myogenic autoregulation are synchronous through time, and when ROI are far apart the same dynamics are not synchronous (Table 2.3, Fig. 2.12). All three phase estimation technique provided equivalent interpretations of myogenic renal autoregulation.

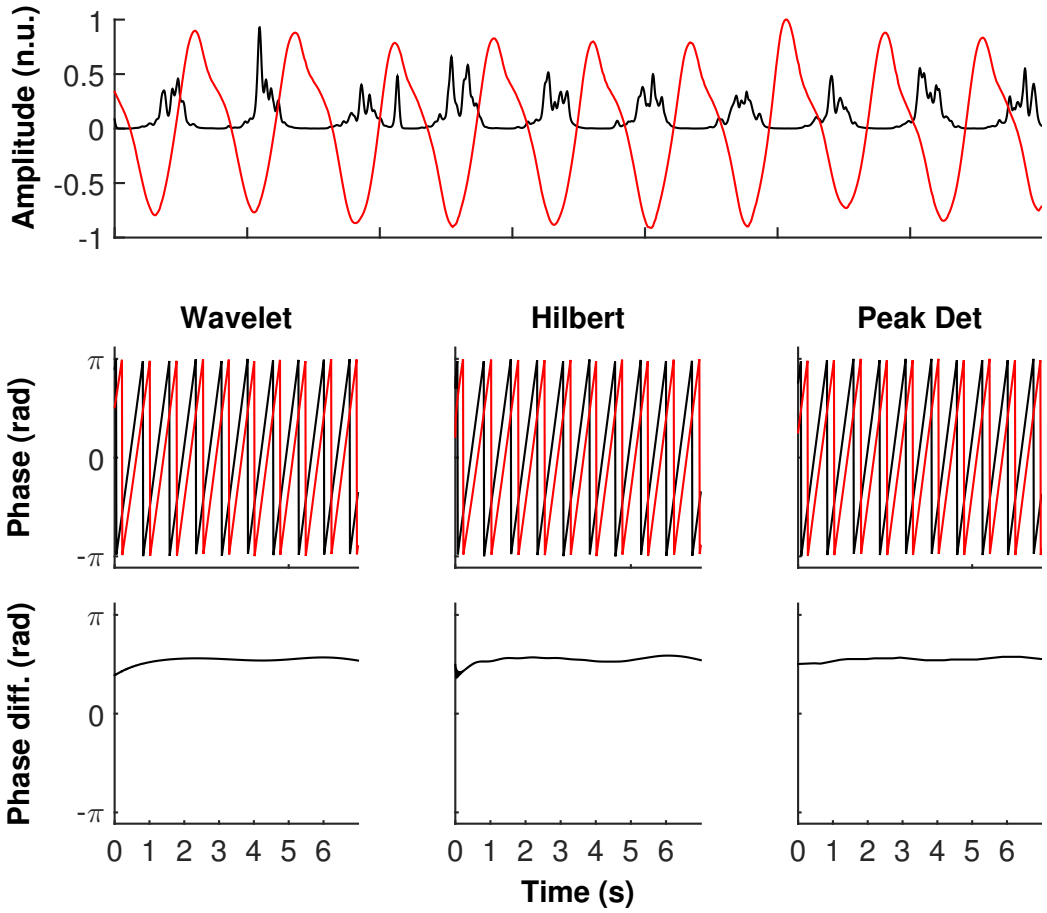

Figure 2.9: Medial gastrocnemius electromyogram (EMG; black) intensity and medial gastrocnemius muscle-tendon unit (MTU; red) length in one human subject during bicycling at a fixed crank speed of 80 revolutions per minute. **Top:** The EMG and MTU length throughout a 7 second recording are shown. Both EMG intensity and MTU length oscillate with the frequency of pedalling. **Middle:** The phase of MTU length and EMG intensity are shown as calculated by each technique. **Bottom:** there is a stable phase difference between EMG intensity and MTU. The results that are returned by all three techniques show similar patterns.

Table 2.3: Difference in phase between two regions on the surface of rat kidney ($n = 7$), with the regions being either close to each other (192μm) or far apart (914 μm).

	Near	Far	p-value
	Circular Mean		
Wavelet	0.036 ± 0.083	0.083 ± 0.750	0.876
Hilbert	0.005 ± 0.110	-0.094 ± 0.760	0.756
Peak Det	-0.059 ± 0.110	-0.49 ± 1.11	0.328
	Circular SD		
Wavelet	0.50 ± 0.39	0.92 ± 0.21	0.043
Hilbert	0.35 ± 0.12	0.87 ± 0.27	0.003
Peak Det	0.28 ± 0.31	0.95 ± 0.30	0.002

Mean $\pm$ standard deviation (rad)

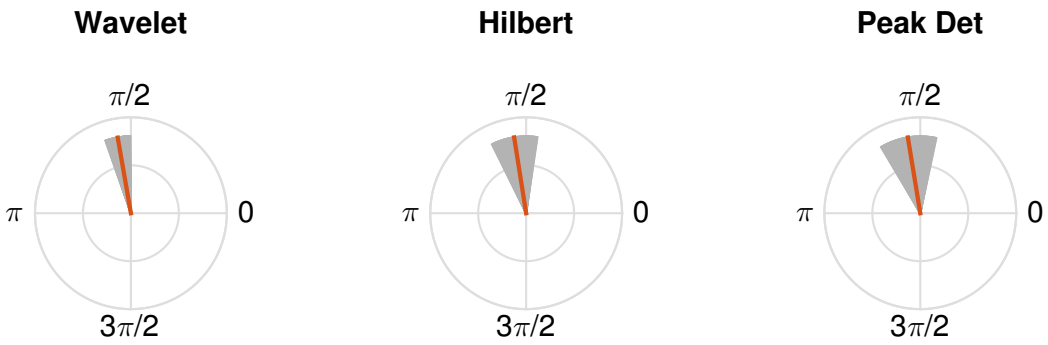

Figure 2.10: Circular mean of phase difference between human EMG intensity and muscle-tendon unit length. The red bar in each plot represents the mean phase difference while the grey area represents the circular standard deviation of phase difference. The mean phase difference is near $\pi/2$ in all three techniques, with similar standard deviation although wavelet showed a slightly lower degree of variation compared to the other two techniques.

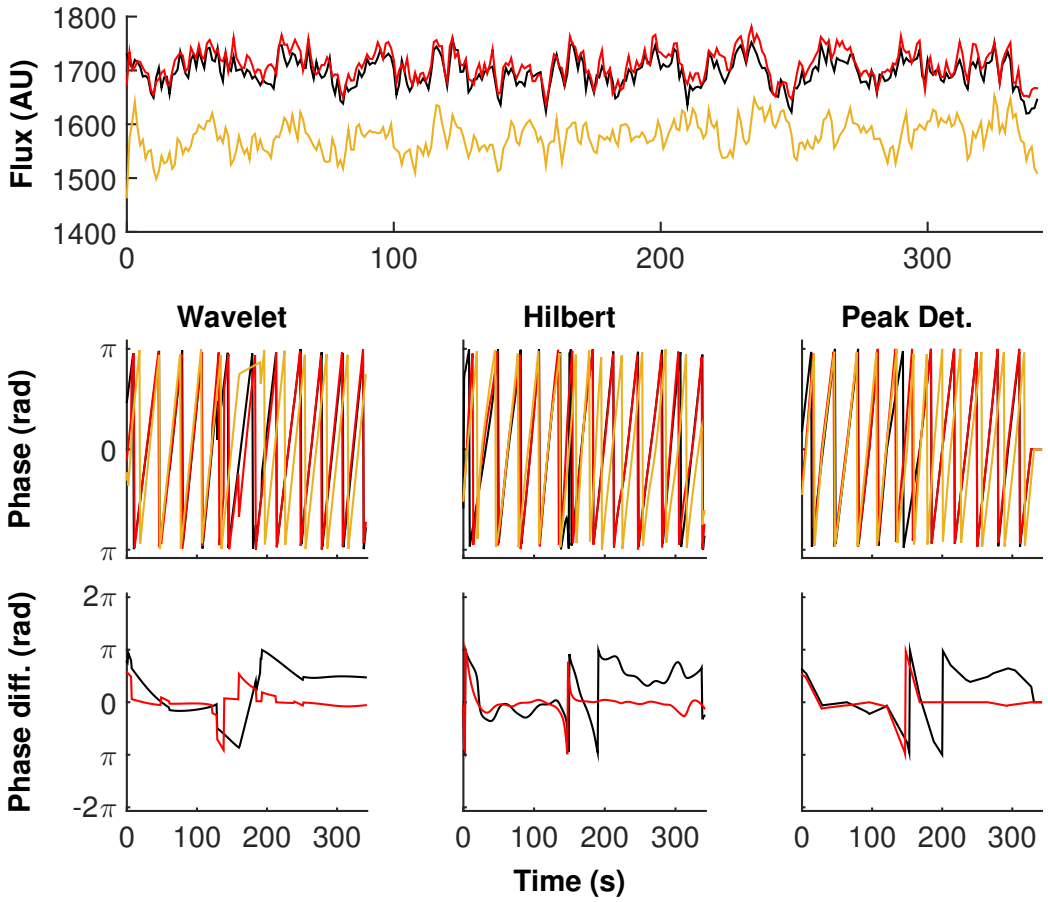

Figure 2.11: Renal surface perfusion from three separate regions of interest (ROI). Two ROI (black, red) are 140μm apart and the third (yellow) is 1.2 mm away from them. **Top:** Time series perfusion data are represented as flux, which is an index of blood flow. The nearby ROI have similar fluctuations over time, consistent with synchrony, while the distant ROI is independent of the first two ROI. **Middle:** Phase of each ROI, acquired using the three previously described techniques. **Bottom:** Difference in phase between nearby (blue: ROI1 *vs* ROI2) and distant (red: ROI1 *vs* ROI3). There are clear fluctuations in phase difference when ROI are far apart, while the phase difference is generally near zero when ROI are close to each other.

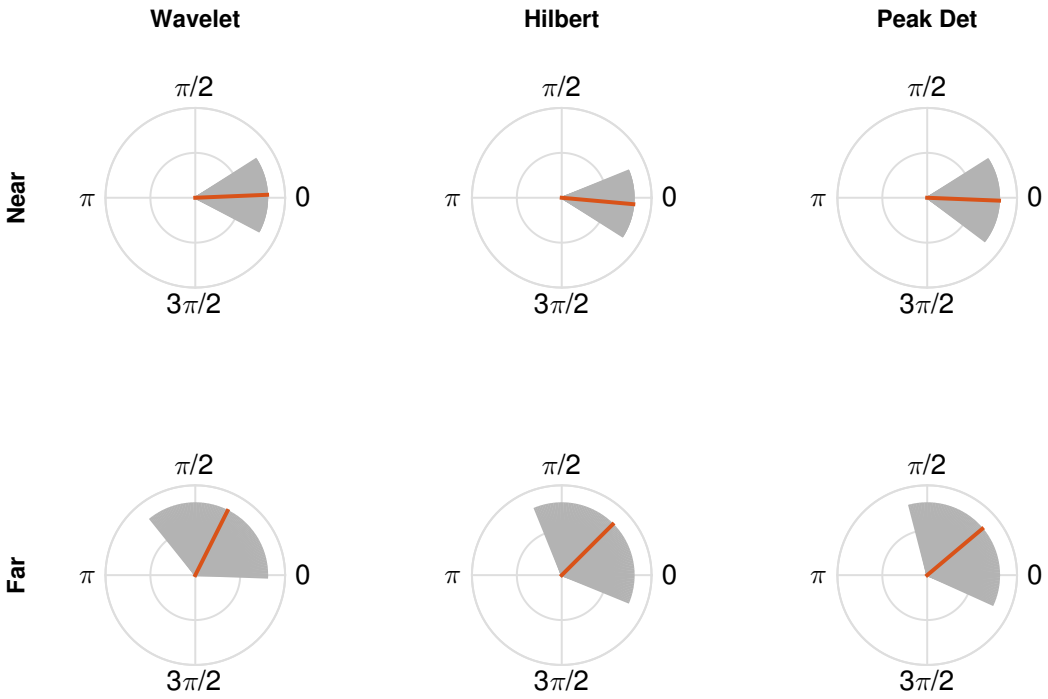

Figure 2.12: Circular mean of the phase difference between two ROI that are close to each other (**Near; Top**) or far apart (**Far; Bottom**) for one rat. In each plot, the red bar indicates the mean phase difference, and the grey area is the circular standard deviation of the phase differences that occurred in each time series. The three techniques of phase estimation return equivalent responses. When ROI are near to each other, phase difference is close to zero and generally tightly distributed around zero. However, when ROI are far apart, mean phase difference assumes a value that can be different from zero, and there is a wide range of values for the phase difference.

2.5 Discussion

Three techniques for estimating phase were compared in terms of accuracy and computing time. Our *in silico* test signals were time-varying by design, because biological systems are never strictly stationary, and was made to reflect the properties of the physiological signals that were subsequently considered. The Morlet wavelet transform technique obtained phase at each time point using the frequency of highest power. The Hilbert transform technique obtained phase by performing a weighted average of the phase of each frequency using the Fourier transform. The peak detection technique identified local maxima and computed phase from them.

Upon testing these techniques *in silico*, their behaviours under signal-to-noise ratios from $[-20, 5]$ dB were distinguished. The wavelet technique was the most susceptible to increasing levels of noise, resulting in significantly higher variance for SNR lower than -9 dB. The Hilbert transform and peak detection techniques continued to perform surprisingly well, even with SNR below -9 dB. Under conditions of very high noise levels in the signal of interest, therefore, the Hilbert transform or peak detection techniques should be favoured. The reason why the wavelet technique, as designed here, was more susceptible to noise was most likely due to its constitution as a *maximum likelihood estimator*, meaning it identified a single frequency as the carrier of information, rather than use a weighted average, as in the Hilbert transform technique. The vast majority of studies that use a wavelet-base technique of phase estimation do so as a maximum likelihood estimator.

The ability of a single family of wavelets, the Morlet wavelet of order 6, to estimate phase under varying conditions of noise *in-silico* for signals of high stationarity was tested. A higher order wavelet, with lower time resolution but greater frequency resolution, might have successfully averaged out the types of errors that this method of analysis created. Furthermore, in physiological settings, wavelets that are adapted to the specific oscillating characteristics of interest are known to more accurately estimate frequency and time domain components [23].

The relatively small errors for all three techniques at SNR ≥ -5 suggest that the type of forward-backward filtering that was used did not modify signal phase beyond an acceptable range for the *in-silico* data. From these analyses, it was concluded that negligible phase alteration also occurred during filtering of the *in-vivo* data.

The wavelet technique took the most computing time - greater than 10 times the duration of the other two. The only difference in the implementation of each phase estimation technique was the phase estimator. If speed is an issue, with especially large data files, then the wavelet technique should be avoided.

The Hilbert transform and peak detection techniques depend critically on *a priori* knowledge of the relevant frequency domain. In contrast, the wavelet technique returns a time-

frequency representation of the signal, and therefore could easily be adapted to work without any filtering.

The peak detection technique was computationally simpler than the Hilbert transform and wavelet techniques while it remained as accurate. Its relative simplicity allowed for better communication and comparison of results. However, the existence of plateaux (flat maximal regions) in the signal would have prevented clear identification of a single peak per cycle, which would have rendered the peak detection technique inadequate.

Taken together, these results can be used to determine which phase estimation technique is best for a particular application. The decision process is summarised in Fig. 2.13. The criteria were elaborated based on the conditions necessary to implement the three detection methods rather than from direct interpretations of the results of the study. They represent *sine qua non* criteria, rather than loose guidelines.

The *in-silico* signal design incorporated many of the characteristics of the relevant *in-vivo* signals. It was built by assembling individual oscillations of frequencies varying a central value, with the addition of levels of noise, analogously to time series like blood presssure, RR intervals, nasal temperature, and blood perfusion. The model did not, however, incorporate non-stationarities or stochastic processes, both of which are expected to exist in varying degrees within the signals mentioned, and was limited to testing each techniques' resilience under noise.

Because it is impossible to know the true phase of the *in-vivo* signals, because there is no gold standard of phase estimation in physiology, and indeed because the notion of true phase in such instances cannot be well defined, our conclusions were based upon the physiological interpretations that could be made from the three estimations. These interpretations were specific to the physiological situations, and required specific outcome variables.

Upon application to human systolic blood pressure and RR interval time series, the three techniques produced the same physiological conclusion. Namely, that changes in SBP precede changes in RR intervals in a frequency band around 0.1 Hz, which is compatible with baroreflex control of heart rate response to spontaneous oscillations in blood pressure. This was true individually, as well as for group statistics.

The breathing rate and RR interval data highlighted an important limitation of the three techniques. Although participants were instructed not to change their rate or depth of breathing, those frequencies changed in time, many going well below what would be expected for healthy adults [26]. This highlights the potential downfall of having to choose a static filtering band. In such a case, the wavelet technique would be prescribed for the initial exploration of the power spectrum of the signal, and could therefore be used for the subsequent phase analyses without additional downfalls.

The MG was activated during muscle lengthening, and the resulting phase difference was similarly detected by all three phase estimation techniques. The results were consistent with a role for the MG as a braking muscle during pedal downstroke.

The rat renal blood flow data distinguish themselves from the other sets of data presented because they show how phase can be used to identify strengths of interactions among oscillating signals. Whereas the other physiological examples reveal interactions where one system drives changes in another system, the renal data provided evidence that blood flow dynamics mutually entrain and become synchronous. Again, all three techniques generated equivalent interpretations.

2.6 Conclusion

Three useful techniques for estimation of the phase of oscillatory physiological signals were highlighted. The application of each technique was demonstrated in a broad variety of physiological systems. Generally speaking, it was found that when oscillatory physiological signals were analysed, the wavelet transform, Hilbert transform, and peak detection techniques each return similar results.

The peak detection technique was originally designed as a naïve alternative to the two most widely used other techniques. Its relatively good performance was then quite surprising. This finding encourages further examination of its characteristics and performances under different conditions.

Decision criteria were summarised in a tree to assist with technique selection (Fig. 2.13). The criteria were elaborated based on the conditions necessary to implement the three detection methods rather than from direct interpretations of the results of the study. They mostly represent *sine qua non* criteria, rather than loose guidelines.

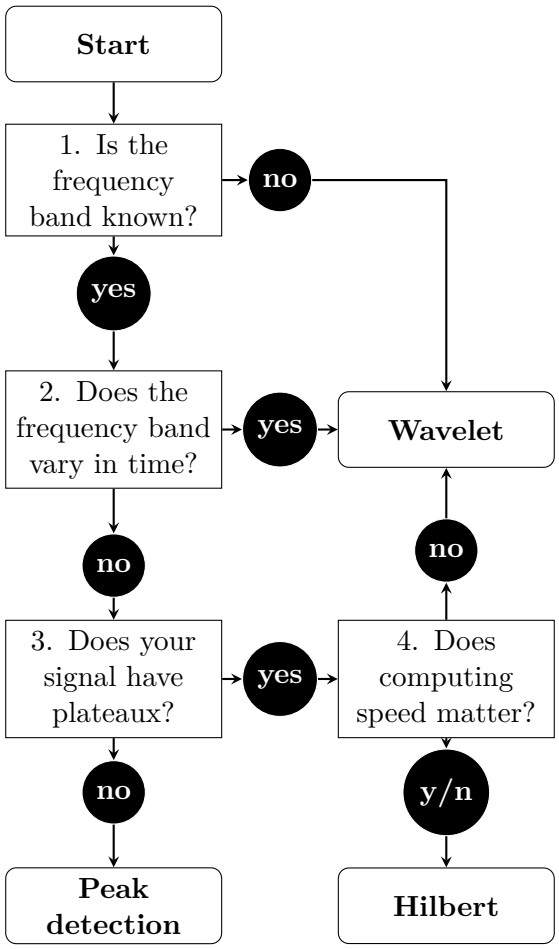

Figure 2.13: Decision tree for selecting the most appropriate technique of phase estimation. The first, second and third criteria were elaborated upon the conditions necessary to implement the three detection methods rather than from direct interpretations of the results of the study. They represent *sine qua non* criteria, rather than loose guidelines.

2.7 References

[1] M. Malik, J. T. Bigger, A. J. Camm, R. E. Kleiger, A. Malliani, A. J. Moss, and P. J. Schwartz, "Heart rate variability standards of measurement, physiological interpretation, and clinical use," *European Heart Journal*, vol. 17, no. 3, pp. 354–381, 1996.

[2] S. Mayer, "Studien zur physiologie des herzens und der blutgefässe 6. abhandlung: Über spontane blutdruckschwankungen.," *Sitzungsberichte Akademie der Wissenschaften in Wien. Mathematisch-naturwissenschaftliche Classe, Anatomie*, vol. 74, pp. 281–307, 1876.

[3] K. Fujii, D. D. Heistad, and F. M. Faraci, "Vasomotion of basilar arteries in vivo," *American Journal of Physiology: Heart & Circulatory Physiology*, vol. 258, no. 6 Pt 2, pp. H1829–34, 1990.

[4] M. Solomonow, C. Baten, J. Smit, R. Baratta, H. Hermens, R. D'Ambrosia, and H. Shoji, "Electromyogram power spectra frequencies associated with motor unit recruitment strategies," *Journal of Applied Physiology*, vol. 68, no. 3, pp. 1177–85, 1990.

[5] C. A. Czeisler and E. B. Klerman, "Circadian and sleep-dependent regulation of hormone release in humans.," *Recent Progress in Hormone Research*, vol. 54, pp. 97–130, 1998.

[6] S. M. Doesburg and L. M. Ward, "Synchronization between sources: emerging methods for understanding large-scale functional networks in the human brain," in *Coordinated Activity in the Brain*, pp. 25–42, Springer, 2009.

[7] M. Lauk, B. Köster, J. Timmer, B. Guschlbauer, G. Deuschl, and C. Lücking, "Side-to-side correlation of muscle activity in physiological and pathological human tremors," *Clinical Neurophysiology*, vol. 110, no. 10, pp. 1774–1783, 1999.

[8] A. Garg, D. Xu, A. Laurin, and A. P. Blaber, "Physiological interdependence of the cardiovascular and postural control systems under orthostatic stress," *American Journal of Physiology-Heart and Circulatory Physiology*, vol. 307, no. 2, pp. H259–H264, 2014.

[9] C. Scully, N. Mitrou, B. Braam, W. Cupples, and K. Chon, "Segmentation of renal perfusion signals from laser speckle imaging into clusters with phase synchronized dynamics," *IEEE Transactions on Biomedical Engineering*, vol. 61, no. 7, 2014.

[10] A. Boiteux, A. Goldbeter, and B. Hess, "Control of oscillating glycolysis of yeast by stochastic, periodic, and steady source of substrate: a model and experimental study," *Proceedings of the National Academy of Sciences*, vol. 72, no. 10, pp. 3829–3833, 1975.

[11] A. Pikovsky, M. Rosenblum, and J. Kurths, *Synchronization: A universal concept in nonlinear sciences*. Cambridge University Press, 2001.

[12] E. Batschelet, *Circular statistics in biology*, vol. 371. Academic Press London, 1981.

[13] M. Le Van Quyen, J. Foucher, J.-P. Lachaux, E. Rodriguez, A. Lutz, J. Martinerie, and F. J. Varela, "Comparison of Hilbert transform and wavelet methods for the analysis of neuronal synchrony," *Journal of Neuroscience Methods*, vol. 111, no. 2, pp. 83–98, 2001.

[14] R. Q. Quiroga, A. Kraskov, T. Kreuz, and P. Grassberger, "Performance of different synchronization measures in real data: a case study on electroencephalographic signals," *Physical Review E*, vol. 65, no. 4, p. 041903, 2002.

[15] M. Farge, "Wavelet transforms and their applications to turbulence," *Annual Review of Fluid Mechanics*, vol. 24, no. 1, pp. 395–458, 1992.

[16] C. Torrence and G. P. Compo, "A practical guide to wavelet analysis," *Bulletin of the American Meteorological Society*, vol. 79, no. 1, pp. 61–78, 1998.

[17] C. G. Scully, N. Mitrou, B. Braam, W. A. Cupples, and K. H. Chon, "Detecting physiological systems with laser speckle perfusion imaging of the renal cortex," *American Journal of Physiology-Regulatory, Integrative and Comparative Physiology*, vol. 304, no. 11, pp. R929–R939, 2013.

[18] R. M. Baevsky, I. Funtova, A. Diedrich, A. G. Chernikova, J. Drescher, V. M. Baranov, and J. Tank, "Autonomic function testing aboard the ISS using "PNEUMOCARD"," *Acta Astronautica*, vol. 65, no. 7, pp. 930–932, 2009.

[19] C. A. C. J. Gerhardt, *Handbuch der Kinderkrankheiten: Krankheiten der Neugeborenen, Allgemeinerkrankungen erster Theil (Acute Infectionskrankheiten)*, vol. 2. H. Laupp'schen Buchhandlung, 1877.

[20] J. A. Hirsch, B. Bishop, *et al.*, "Respiratory sinus arrhythmia in humans: how breathing pattern modulates heart rate," *American Journal of Physiology: Heart & Circulatory Physiology*, vol. 241, no. 4, pp. H620–H629, 1981.

[21] A. Angelone, N. A. Coulter, *et al.*, "Respiratory sinus arrhythmia: a frequency dependent phenomenon," *Journal of Applied Physiology*, vol. 19, no. 3, pp. 479–482, 1964.

[22] S. L. Delp, F. C. Anderson, A. S. Arnold, P. Loan, A. Habib, C. T. John, E. Guendelman, and D. G. Thelen, "Opensim: open-source software to create and analyze dynamic simulations of movement," *Biomedical Engineering, IEEE Transactions on*, vol. 54, no. 11, pp. 1940–1950, 2007.

[23] V. von Tscharner, "Intensity analysis in time-frequency space of surface myoelectric signals by wavelets of specified resolution," *Journal of Electromyography and Kinesiology*, vol. 10, no. 6, pp. 433–445, 2000.

[24] M. H. Dickinson, C. T. Farley, R. J. Full, M. Koehl, R. Kram, and S. Lehman, "How animals move: an integrative view," *Science*, vol. 288, no. 5463, pp. 100–106, 2000.

[25] A. R. Brazhe, D. J. Marsh, N.-H. Holstein-Rathlou, and O. Sosnovtseva, "Synchronized renal blood flow dynamics mapped with wavelet analysis of laser speckle flowmetry data," *PloS one*, vol. 9, no. 9, p. e105879, 2014.

[26] J. E. Hall, *Guyton and Hall Textbook of Medical Physiology: Enhanced E-book*. Elsevier Health Sciences, 2010.

Chapter 3

New indices from microneurography to investigate the arterial baroreflex

> Every twitching nerve and pulsing vein carries a message, discernible with the right tools.
>
> *MTG, Pain Seer*

3.1 Introduction

Baroreflex-mediated changes in heart rate and vascular resistance in response to variations in blood pressure are critical to maintain homeostasis. Inadequate responses resulting in hypotension vary widely in severity, causes, and symptoms [1]. In fighter pilots and astronauts, orthostatic hypotension due to severe changes in gravitational forces can cause an interruption in cognitive function and syncope, precisely in moments of critical importance [2, 3]. Studies that examine the reactions of highly tolerant individuals to extreme environments have often influenced standard cardiovascular models of orthostatic intolerance or delayed intolerance. In the the elderly, a group with high prevalence of orthostatic intolerance, orthostatic hypotension has been linked to higher risks of myocardial infarction [4], stroke [5], and may also cause syncope, a significant contributor to falls and injury [6].

Baroreceptors located in the carotid sinus, coronary arteries, and the aortic arch respond to changes in vessel diameter. Increased blood pressure distends vessel walls, which in turn increases baroreceptor afferent activity. This inhibits the vasoconstrictor center of the medulla, reducing sympathetic activity, and excites the vagal parasympathetic center.

The net effects in the heart are decreased heart rate and contractility. The effect on the peripheral blood vessels is general dilation.

It has been shown in young adults that an impairment in the ability to increase vascular responses to baroreflex stimulation when upright is associated with poor orthostatic tolerance [7]. This has led to the hypothesis that maintenance of blood pressure during orthostasis depends primarily on a vascular response, and secondly on a cardiac response [8, 9]. However, despite the evidence of the relative importance of vascular responses [10], there continues to be debate regarding the relative contribution of the cardiac and vascular responses to orthostasis [11].

Previous work has shown that the frequency of maximal coherence between RR interval and systolic arterial pressure time series in the low-frequency range was correlated to time-to-presyncope in individuals with histories suggestive of unexplained syncope.[12, 13]. Due to its minimal invasiveness, this index holds great potential to help in the clinical diagnosis of orthostatic intolerance. The physiological interpretation of this frequency is difficult to obtain, however, in part due to the absence of concurrent direct vascular analysis in the cited studies.

Lower body negative pressure (LBNP) is a technique where participants' lower body is placed in an air-tight box at the level of the iliac crest, air removed via a vacuum pump to reduce the internal box pressure. It is often used to investigate the reaction of the cardiovascular system to stress similar to standing or hypovolemia, but with minimal muscle pump effect and no vestibular stimuli [14, 15, 16]. The technique pools blood into the lower body and lowers blood pressure, decreasing parasympathetic and increasing sympathetic outflow, which in turn increases heart rate, myocardial contractility, and total peripheral resistance (Fig. 3.1).

While the parasympathetic-mediated effects on heart rate are easily measured via surface electrocardiogram, quantification of the sympathetic outflow is more difficult. Microneurography, which is not used clinically and requires onerous hands-on training, has been used since the late 1960's to record muscle sympathetic nervous activity (MSNA) and quantify sympathetic outflow to the arteries [17]. The technique has been recently used to study the arterial response to changes in blood pressure and its changes during pre-syncope in orthostatic finisher individuals [18, 19, 20].

Although these studies have contributed significantly to our understanding of the relationship between blood pressure and MSNA before and during pre-syncope, the challenge remains to understand the differences between levels of orthostatic tolerance in both cardiac and arterial branches of the baroreflex. The goal of this study was to examine the relationship between blood pressure and MSNA as it pertains to orthostatic tolerance. In particular the aim was to identify an index capable to distinguish possible mechanisms that contribute to earlier presyncope.

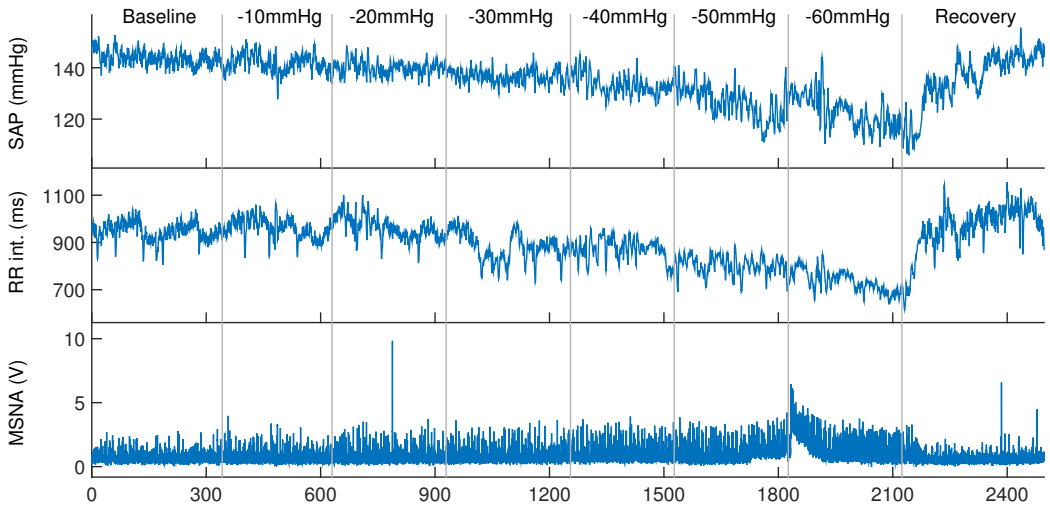

Figure 3.1: An example of typical systolic arterial pressure (SAP), RR intervals, and muscle sympathetic nervous activity (MSNA) responses during graded lower body negative pressure (LBNP). The participant shown here did not experience pre-syncope.

Blood pressure, heart rate, and MSNA all oscillate at a rate of approximately 0.1 Hz. These oscillations are commonly referred to as Mayer waves in blood pressure [21], and constitute a major low-frequency (LF) oscillation in all three signals. Although some evidence points to the existence of a central oscillator responsible for these waves, they are in large part due to inherent time delays in the processes involved in the centrally-mediated static baroreflex [22]. Communication latency between receptor and effector organs in the baroreflex negative feedback loop causes constant over/under-shoot and readjustment at the resonant frequency of 0.1 Hz (Fig. 3.2). Studying the relationships between the components of LF oscillations is key to understanding the baroreflex.

Low-frequency DAP and MSNA fluctuations, as well as the relationship between these two variables is usually quantified by frequency analysis. Individual DAP and MSNA power quantifies the amount of activity during a given period of time, and coherence quantifies the degree to which their oscillations are related.

In normotensive patients at rest, diastolic arterial pressure (DAP) and MSNA power in the LF range is relatively low, as is their coherence. Upon application of LBNP, coherence increases, as does their respective powers in the LF range [19, 25]. This shows that a loose healthy relationship between DAP and MSNA exists at rest which tightens when under stress, even when that stress is minimal, such as during a sit-to-stand test or a minute of -10 mmHg of LBNP.

The hypothesis is that while cardiac baroreflex indices cannot distinguish between levels of high orthostatic tolerance, the relationship between MSNA and DAP is different between these groups, and that this difference can be identified at early stages of orthostatic stress.

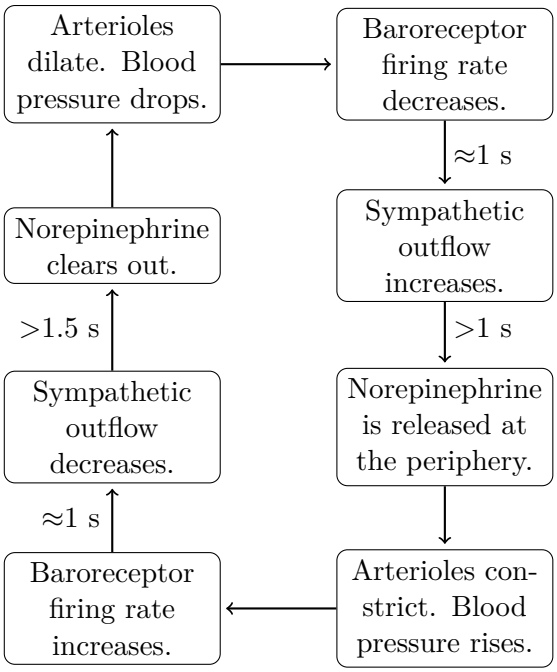

Figure 3.2: Summary of the main pathway of the arterial baroreflex loop. The principal time delays and communication lags are indicated [23, 17, 24]. Low frequency (0.1 Hz) oscillations in blood pressure (Mayer waves), MSNA, and total peripheral resistance emerges from the interactions between these lags and delays [22]. One such loop takes between 7 and 25 seconds, taking into account variations in the amplitude of blood pressure variation and the periods of MSNA activity/inactivity.

3.2 Methods

Eleven healthy, normotensive participants underwent LBNP at 0, −10, −20, −40, −50, and −60 mmHg. Each level was sustained for 5 minutes. LBNP was terminated when participants exhibited symptoms of presyncope. Participants that did not display symptoms of presyncope throughout the protocol were classified as finishers. Those that displayed presyncope before completing the 5-minute −60 mmHg level were classified as non-finishers. For all non-finishers, symptoms of presyncope occurred either during the −50 mmHg level, or at the onset of the −60 mmHg level.

Continuous measurements of ECG, MSNA, and blood pressure were recorded simultaneously on a personal computer with analogue-to-digital conversion (Acqknowledge, Biopack Systems, Goleta, CA, USA) for subsequent analysis. The continuous analogue electrocardiogram signal was then used to obtain R waves using the Pan-Tompkins algorithm [26]. RR intervals were then computed.

Continuous waveform blood pressure was provided by finger photoplethysmography (Finapres, Ohmeda, Englewood, CO, USA). Diastolic and systolic arterial pressures (SAP) were obtained as the maximum and minimum arterial pressures in each RR interval. For

each heart cycle, to adjust for the time of propagation of the blood pressure wave from the heart to the finger, the time difference between the R peak and diastolic timing was subtracted from both systolic and diastolic timings.

The resulting RR interval and arterial pressure time series were resampled at 5 Hz using a shape-preserving piecewise cubic interpolation method and forward-backward bandpass filtered to a band of $[0.04, 0.15]$ Hz to isolate LF oscillations. This filter design, particularly in its application in one time-direction and then the other, was chosen to minimize its effect on phase.

Muscle sympathetic nerve signals were obtained by microneurography. Unipolar tungsten microelectrodes (shaft diameter 0.1 mm and impedance 1-5 MΩ) were manually inserted percutaneously into sympathetic fasciles in the tibial nerves. One electrode was used for direct intraneural recordings and a second surface electrode was placed as a reference 3.0 cm away from the recording electrode. The electrodes were connected to a high impedance amplifier and the sympathetic signal was transmitted to a $[700, 2000]$ Hz band pass filter and amplified by a factor of 105. The neurogram was full wave rectified and integrated with a time constant of 0.1 s. MSNA was lowpass filtered with a cutoff frequency of 10 Hz to remove background activity. The number of bursts per low frequency baroreflex-mediated loop was used to quantify MSNA. Bursts were identified as points having a prominence of 3 times the inter-quartile range (3·iqr) of the MSNA signal, and no closer to each other than 0.9 times the shortest RR interval. Prominences between 2·iqr

To test whether traditional cardiac baroreflex indices were different berween finishers and non-finishers, cross-spectral analyses on the RR intervals and SAP time series was performed. These time series were fitted by a bivariate autoregressive model. Coherence and transfer function gain between SAP and RRI were computed, as well as the frequency of maximal coherence in the LF range [27, 28]. Gain and frequency values were only accepted when coherence was above 0.5.

To study the arterial baroreflex, DAP was chosen over SAP since it has been shown that the rhythmic relationship between blood pressure and sympathetic outflow is best observed with DAP [29].

The foundation of this study's new approach was to attempt to isolate single neurogenic constriction-dilation cycles in arteries. Time-frequency analysis techniques such as the wavelet or Hilbert transform, make 2 assumptions that render them inadequate for this purpose. First, they assume that the signal is a summation of oscillations of different frequencies and amplitudes. In the case of sympathetic outflow, this assumption is false for a recording at one particular location. In the case of diastolic blood pressure, although LF oscillations at one location may or may not constitute some addition of many related forces, the new assumption that the measured phenomenon constitutes a single cycle local neurogenic constriction-dilation cycle offers new avenues for interpretation.

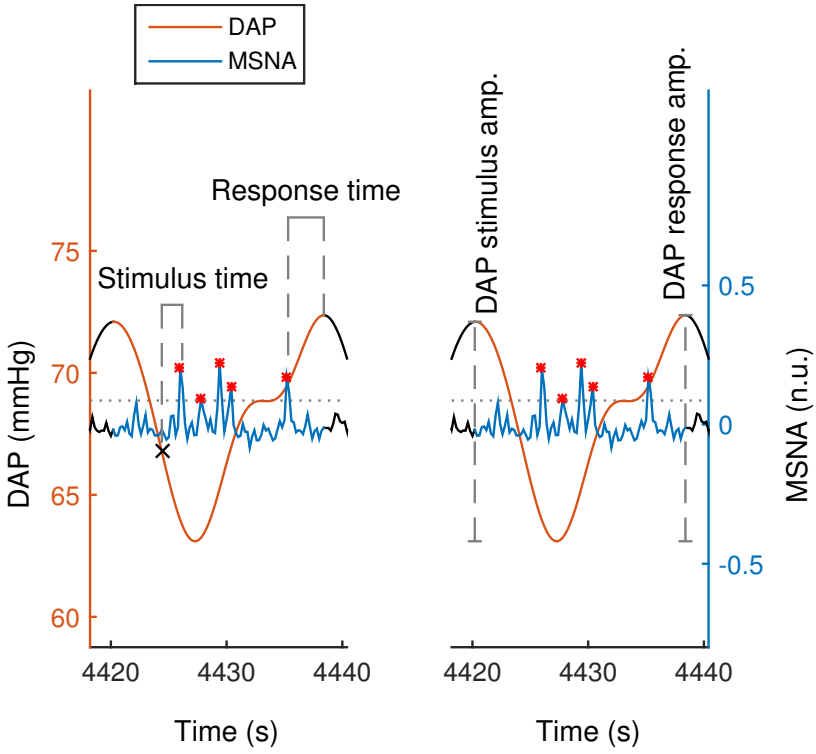

Figure 3.3: Filtered diastolic blood pressure (DAP) and muscle sympathetic nervous activity (MSNA) during a single low frequency baroreflex-mediated loop (Fig. 3.2). The steepest drop in DAP is shown as $\times$, and is a surrogate for the start of the blood pressure drop stimulus. MSNA bursts are shown as red $*$, with 3·iqr shown as a dotted line to represent the prominence threshold. Stimulus time is the time from the steepest drop in DAP to the first MSNA burst. Response time is the time from the last MSNA burst and the end of the loop. DAP stimulus amplitude is the magnitude of DAP change from the beginning of the loop to its lowest point. DAP response amplitude is the magnitude of DAP change from its lowest point to the end of the loop. DAP amplitudes are computed from the unfiltered signal and are shown here for heuristic purposes.
Here, the number of bursts is 5, stimulus time = 1.6 s and response time = 3.2 s. DAP stimulus amplitude = 7 mmHg, and response amplitude = 15 mmHg. The ratio of the 7 mmHg DAP stimulus to 5 MSNA bursts was used to compute the stimulus slope, and the ratio of 5 MSNA bursts to the 15 mmHg DAP response was used to compute the response slope.

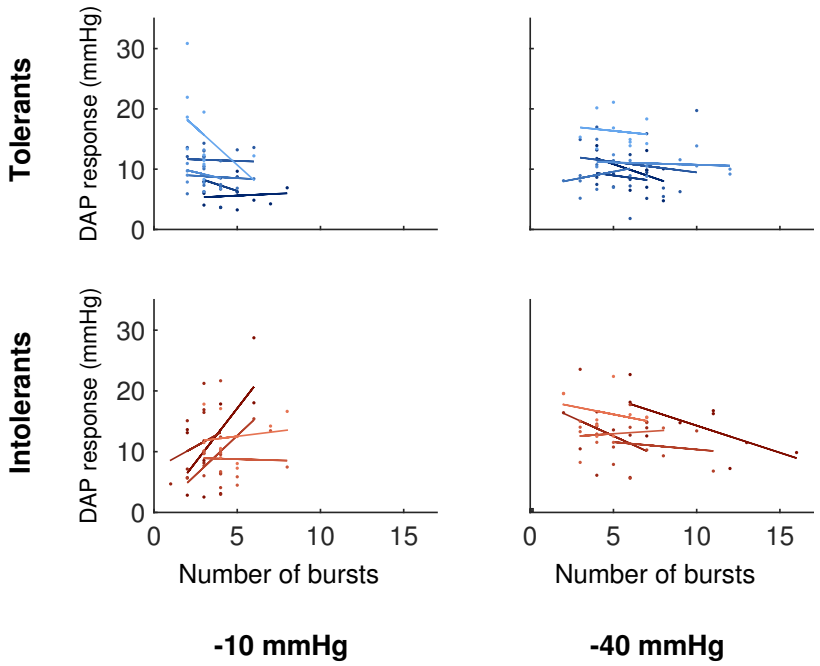

Figure 3.4: DAP response amplitude *versus* number of bursts in single low frequency baroreflex-mediated cycles (Fig 3.3). Figure shows values for -10 and -40 mmHg of lower body negative pressure (LBNP), for finishers and non-finishers. For each level of LBNP, ten low frequency baroreflex-mediated cycles were chosen to maximize DAP amplitudes, area under MSNA, and number of MSNA bursts. For each participant, represented by different colors, those ten loops are shown. Linear regressions are shown.

The second frequency analysis assumption is that oscillations are constant within some time window. Although both wavelet and Hilbert analyses constitute intelligent compromises between frequency and time domain resolutions, their quantification of a single cycle will always include previous and subsequent cycles. For example, in Morlet wavelet analysis of order 6, which is most commonly used, the 0.1 Hz power of a signal at time t includes the analysis of the signal at $t-30$ and $t+30$ seconds. In the case of Hilbert analysis, time-domain information is obtained by weighing frequency-domain variables by their respective power, and assumes time constance.

To isolate single neurogenic constriction-dilation cycles in the LF band, peaks were identified on the filtered and resampled DAP signal as any positive relative maximum with a minimum of 6.67 seconds (or 1/0.15 Hz) between them. These peaks were then used to obtain the closest relative maximum on the unfiltered DAP signal, which in turn were used as estimates for the time of maximum constriction. These peaks were used as cutoffs between cycles and the segments between them were then deemed single LF cycles in both DAP and MSNA.

It is known that acute drops in DAP cause increased MSNA [29]. In every LF cycle, the point of minimal derivative (MD) was identified to estimate the time of DAP mediated

sympathetic activation. For each cycle, MSNA bursts occurring between MD and the end of the cycle were identified.

Many variables affect MSNA and DAP. To locate the LF cycles where the DAP-MSNA relationship was strongest, an estimator of strength (S) for each cycles was computed. S was computed as the multiplication of MSNA area, number of MSNA bursts, and DAP amplitude. The 10 cycles with the highest S were kept for further analysis.

For each identified LF cycles, six indices were computed. These included four primary indices and two secondary indices (Table 3.1, Fig. 3.3). Indices were tested for statistical difference between groups for each level of LBNP, and within groups with respect to -10 mmHg. The mild level of -10 mmHg was chosen instead of baseline based on observations and previous research ([19, 25]) that indicated that the resting relationship between DAP and MSNA is weak, and might produce invalid indices. In figures, when no statistical difference was obtained between group within LBNP levels, values from both groups are shown together.

Where the indices were different between groups at -10 mmHg, the receiver operating character curve was computed to explore their predictive potential [31]. On this curve, the percentage of of true positives (sensitivity) is plotted against the percentage of false negatives (1-specificity) for a range of threshold index values. A good predictive index threshold has both a high sensitivity and a high specificity.

Signal analysis was performed in Matlab 2014b (Mathworks, MA, USA), and statistical analysis in JMP 11.2 (SAS Institute Inc, NC, USA). Values reported are mean $\pm$95% confidence interval. Confidence interval was computed as 1.95 the standard error within the group and LBNP level. Tukey's range test was used to compare values across LBNP levels together with non-finishers *versus* finishers (two-way ANOVA). Values of $p < 0.05$ were considered significant.

Table 3.1: Four primary indices and two secondary indices quantifying the relationship between diastolic arterial pressure (DAP) and muscle sympathetic nerve activity (MSNA). The indices were obtained by isolating single low-frequency neurogenic constriction-dilation cycles in DAP.

Primary indices (Fig. 3.3)	Stimulus time	Time from the steepest drop in DAP to the first burst in a single LF cycle. This index is related to the time delay from drops in DAP to subsequent sympathetic nerve activity at the vascular bed. The delay between carotid sinus nerve firing and muscle sympathetic nerve activity in the leg varies linearly according to the height of subjects and is approximately 2 s [23, 17].
	Response time	Time from the last burst in a single LF cycle to the end of that cycle. This index is related to the time from the last norepinephrine release in the synaptic cleft to maximal arterial constriction. In a rat tail artery, norepinephrine clearance takes ≥ 1.5 s [24].
	DAP stimulus amplitude	The absolute difference between DAP at the beginning of a single LF cycle and its lowest point. This index is related to the magnitude of the acute blood pressure stimulus.
	DAP response amplitude	The absolute difference between DAP at the lowest point in a single LF baroreflex-mediated cycle and its last point. This index is related to the magnitude of the neurogenic arterial constriction.
Secondary indices	Stimulus slope	The number of MSNA bursts within each LF cycle was plotted versus its respective DAP stimulus amplitude. A regression line was computed for each subject at each LBNP level using the method of least squares. For each subject, the stimulus slope is the slope of that line. This index quantifies the relationship between the amplitude of single acute blood pressure drop to the subsequent MSNA. A large slope would mean that MSNA is not only triggered by acute drops in DAP, but modulated by the size of that drop.
	Response slope	DAP response amplitude was plotted versus the number of MSNA bursts within each respective LF cycle (Fig. 3.4). A regression line was computed for each subject at each LBNP level using the method of least squares. For each subject, the response slope is the slope of that line. This index quantifies the relationship between MSNA and the subsequent rise in DAP. A large slope would mean that more intense MSNA causes larger LF increases in DAP. Indices similar to this response slope have been used, taking total change in MSNA and DAP into account, instead of individual LF cycles [19, 30].

DAP: diastolic arterial pressure; LF: low-frequency; MSNA: muscle sympathetic nerve activity.

3.3 Results

Mean SAP within LBNP levels were not statistically different between groups. Groups taken together, the means were 135.3 ± 4.2 mmHg, 133.2 ± 3.7 mmHg, 130.5 ± 3.5 mmHg, and 126.5 ± 3.4 mmHg. The means at -30 and -40 mmHg of LBNP were statistically different than the mean at -10 mmHg. The mean at -40 was statistically different than the mean at -10 mmHg. Within the non-finisher group, the mean at -40 mmHg of LBNP was statistically different than the means at -10 and -20 mmHg.

An expected increase in MSNA at increasing levels of LBNP was observed in both groups (Fig. 3.5). Considering both groups together, the mean number of MSNA peaks per LF cycle were 3.72 ± 0.48, 4.40 ± 0.39, 5.12 ± 0.53, and 5.96 ± 1.09 for increasing levels of LBNP. The means at -30 and -40 mmHg of LBNP were larger than the mean at -10 mmHg. The mean at -40 mmHg was also greater than the mean at -20 mmHg. Within LBNP levels, there were no statistical differences between the two groups.

In both the finisher and non-finisher groups, the means at -30 and -40 mmHg LBNP were greater than the mean at -10 mmHg within the group. Their respective mean at -40 mmHg were also greater than their mean at -20 mmHg.

Mean stimulus time decreased from 2.73 ± 0.50 s at -10 mmHg to 2.03 ± 0.28 s, 1.89 ± 0.35 s, and 1.36 ± 0.27 s, at -20, -30, and -40 mmHg respectively (Fig. 3.6). Within LBNP levels, there were no statistical differences between the two groups.

Mean response times in the finisher group were 3.12 ± 0.42 s, 2.72 ± 0.49 s, 2.63 ± 0.56 s, and 2.33 ± 0.35 s for increasing levels of LBNP. The time at -40 mmHg was statistically shorter than at -10 mmHg. For non-finishers, response times were 3.31 ± 0.46 s, 2.90 ± 0.53 s, 2.82 ± 0.61 s, and 2.84 ± 0.38 s, respectively, and were not statistically different from each other (Fig. 3.7).

Mean DAP stimulus amplitudes for finishers were 9.58 ± 2.41 mmHg, 8.86 ± 1.61 mmHg, 10.51 ± 2.30 mmHg, and 11.38 ± 2.40 mmHg for increasing levels of LBNP. The amplitude at -40 mmHg of LBNP was higher than at -20 mmHg of LBNP. For non-finishers, DAP stimulus amplitudes were 10.49 ± 1.75 mmHg, 12.03 ± 2.40 mmHg, 14.31 ± 1.85 mmHg, and 12.79 ± 2.04 mmHg, respectively, and the mean at -40 mmHg of LBNP was higher than that at -10 mmHg of LBNP. Within LBNP levels, there were no statistical differences between the two groups (Fig. 3.8).

Mean DAP response amplitudes for finishers were 9.78 ± 2.86 mmHg, 8.98 ± 1.70 mmHg, 11.03 ± 2.25 mmHg, and 10.88 ± 2.20 mmHg for increasing levels of LBNP. Within the this group, the means were not statistically different from each other. For non-finishers, DAP response amplitudes were 10.72 ± 1.34 mmHg, 12.75 ± 1.68 mmHg, 14.24 ± 1.39 mmHg, 13.60 ± 1.72 mmHg, respectively, and the means at -30 and -40 mmHg of LBNP were higher than at -10 mmHg (Fig. 3.9).

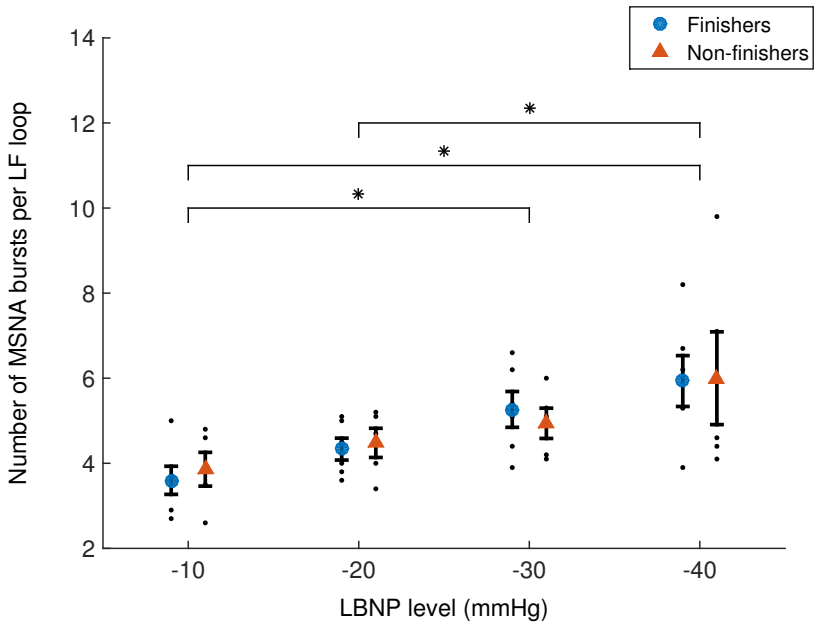

Figure 3.5: Mean number of muscle sympathetic nerve activity (MSNA) bursts within single low frequency baroreflex-mediated cycles for all lower body negative pressure (LBNP) levels ± confidence interval. For each level of LBNP, ten low frequency baroreflex-mediated cycles were chosen to maximize DAP amplitudes, area under MSNA, and number of MSNA bursts. For each subject, the mean of those ten values are shown as smaller grey dots. ∗ indicates statistical difference between levels of LBNP within groups, and also with both groups taken together.

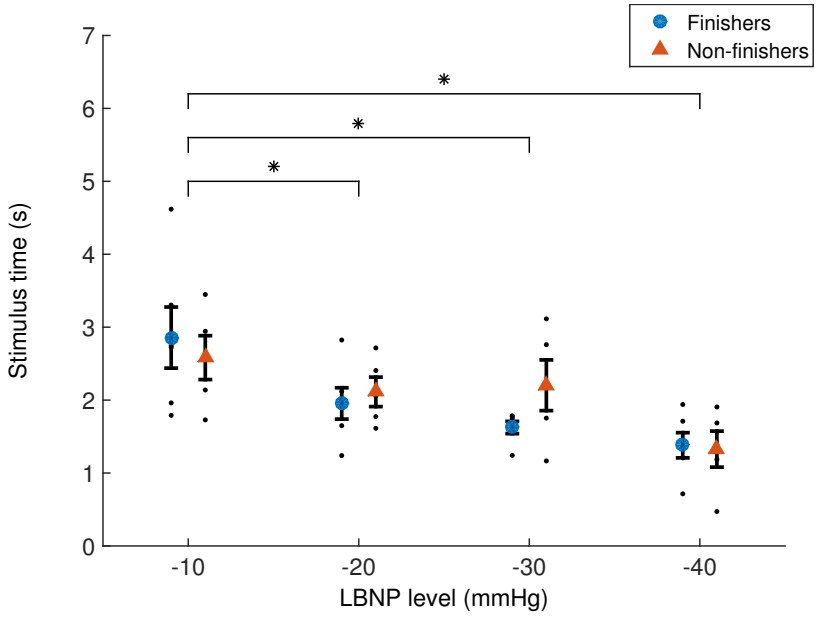

Figure 3.6: Mean stimulus times for all levels of lower body negative pressure (LBNP) ± confidence interval. Within single low frequency baroreflex-mediated cycles, stimulus time is the time from the steepest drop in diastolic arterial pressure to the first muscle sympathetic nerve activity burst. ∗ indicates statistical difference between levels of LBNP.

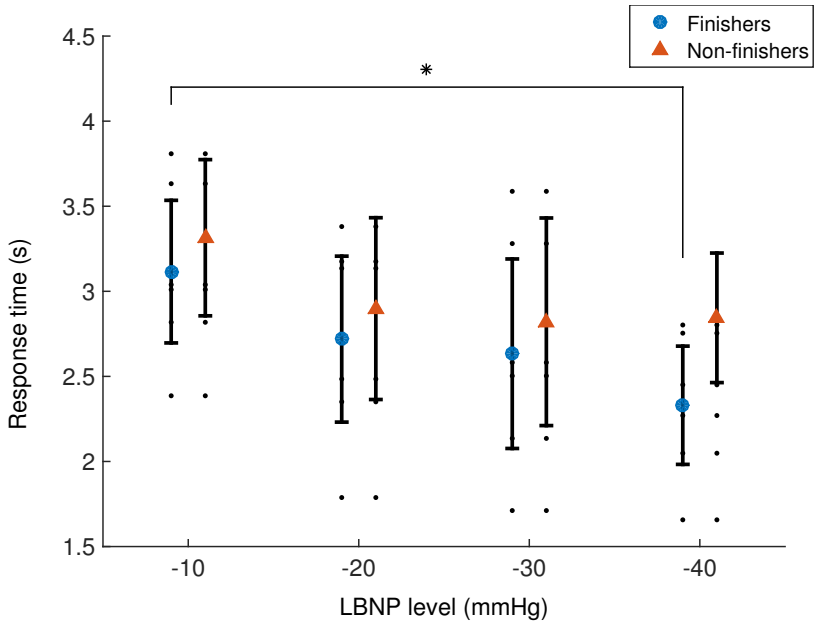

Figure 3.7: Mean response times for all levels of lower body negative pressure (LBNP) ± confidence interval. Within single low frequency baroreflex-mediated cycles, response time is the time from to last muscle sympathetic nerve activity burst to the end of the cycle. The mean response time of finishers at −10 mmHg is statistically different from the −10 mmHg mean in its own group.

Mean stimulus slopes within groups were not statistically different between LBNP levels. Within LBNP levels, they were not statistically different between groups. Their combined means were 0.012 ± 0.181 n/mmHg, -0.029 ± 0.123 n/mmHg, 0.114 ± 0.126 n/mmHg, -0.032 ± 0.152 n/mmHg for increasing levels of LBNP. The mean stimulus slope was different from 0 only for non-finishers at −20 mmHg.

Mean response slopes for finishers was smaller than that for the non-finisher group at −10 mmHg of LBNP. Within the non-finisher group, the mean response slope was smaller at −40 mmHg of LBNP than at −10 mmHg of LBNP (Fig. 3.10). In both groups, the response slope mean was never different than 0.

Means of coherence and gain between systolic arterial pressure and RR intervals within LBNP levels were not statistically different between groups (Tables 3.3 and 3.3). Within groups, they were not statistically different between LBNP levels.

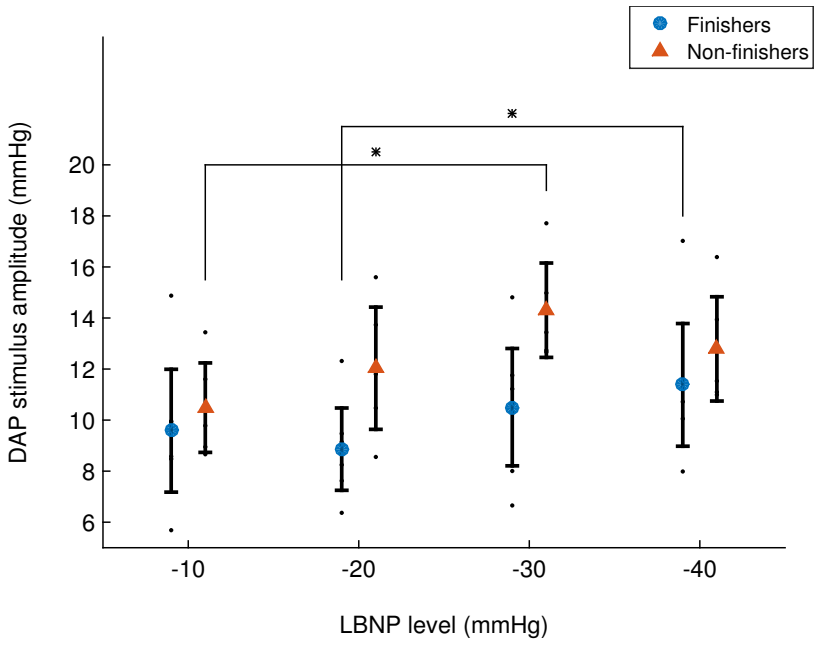

Figure 3.8: Mean diastolic arterial pressure (DAP) stimulus amplitudes for all levels lower body negative pressure (LBNP) ± confidence interval. Within single low frequency baroreflex-mediated cycles, DAP drop amplitude is the absolute difference between the DAP at the beginning of the cycle and the lowest DAP in the cycle. For finishers, the mean at -40 mmHg is different than the mean at -20 mmHg. For non-finishers, the mean at -30 mmHg is different than the mean at -10 mmHg.

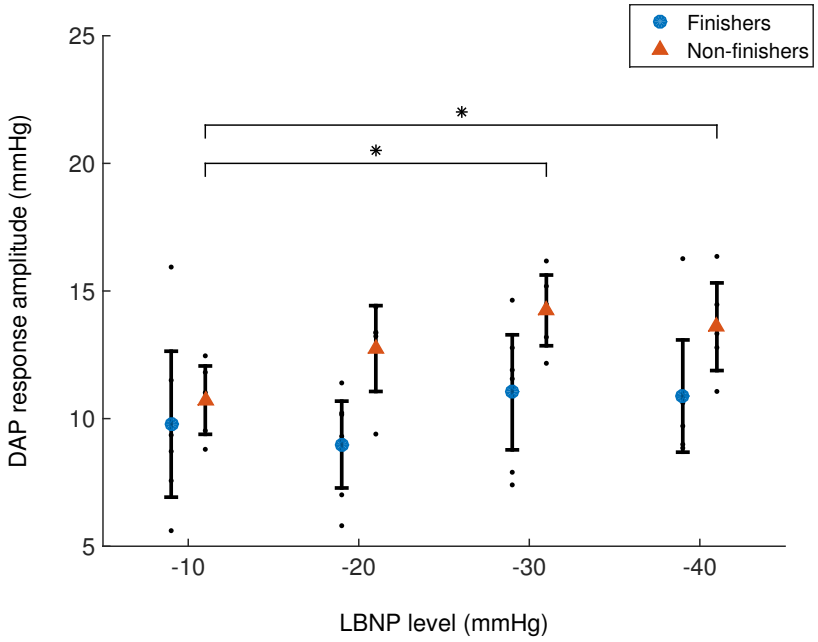

Figure 3.9: Mean diastolic arterial pressure (DAP) response amplitudes for all levels lower body negative pressure (LBNP) ± confidence interval. Within single low frequency baroreflex-mediated cycles, DAP rise amplitude is the absolute difference between the lowest DAP in the cycle to the DAP at the end of the cycle. Means indicated by a $*$ are statistically different from mean at -10 mmHg in their own group.

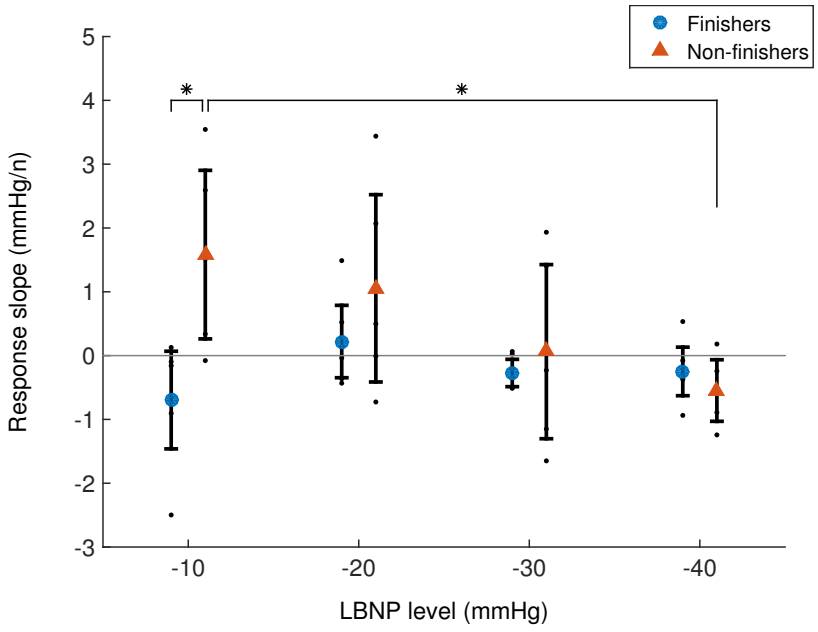

Figure 3.10: Mean response slope for all levels lower body negative pressure (LBNP) ± standard error. Response slope is obtained by computing the regressions between number of muscle sympathetic nervous activity (MSNA) bursts LF cycle and diastolic blood pressure rise amplitudes (see Fig. 3.4). The means of finishers at -10 mmHg and non-finishers at -40 mmHg are statistically different than the mean of non-finishers at -10 mmHg ($p < 0.05$).

Table 3.2: Coherence between systolic arterial pressure and RR intervals (mean ± confidence interval).

	Coherence	
LBNP level (mmHg)	finishers	non-finishers
−10	0.77 ± 0.02	0.86 ± 0.02
−20	0.74 ± 0.02	0.86 ± 0.01
−30	0.82 ± 0.02	0.81 ± 0.02
−40	0.81 ± 0.02	0.85 ± 0.02

Within LBNP levels, values were not statistically different between groups. Within groups, they were not statistically different between LBNP levels ($p < 0.05$).

Table 3.3: Gain between systolic arterial pressure and RR intervals (mean ± confidence interval).

	Gain	
LBNP level (mmHg)	finishers	non-finishers
−10	9.35 ± 73	10.52 ± 62
−20	7.90 ± 35	9.28 ± 58
−30	10.82 ± 65	8.80 ± 106
−40	6.75 ± 35	7.05 ± 65

Within LBNP levels, values were not statistically different between groups. Within groups, they were not statistically different between LBNP levels ($p < 0.05$).

Table 3.4: Frequency of maximal coherence between systolic arterial pressure and RR intervals (mean ± confidence interval).

	Frequency	
LBNP level (mmHg)	finishers	non-finishers
−10	0.090 ± 0.016	0.108 ± 0.010
−20	0.093 ± 0.009	0.090 ± 0.009
−30	0.104 ± 0.011	0.096 ± 0.010
−40	0.103 ± 0.016	0.096 ± 0.013

Within LBNP levels, values were not statistically different between groups. Within groups, they were not statistically different between LBNP levels ($p < 0.05$).

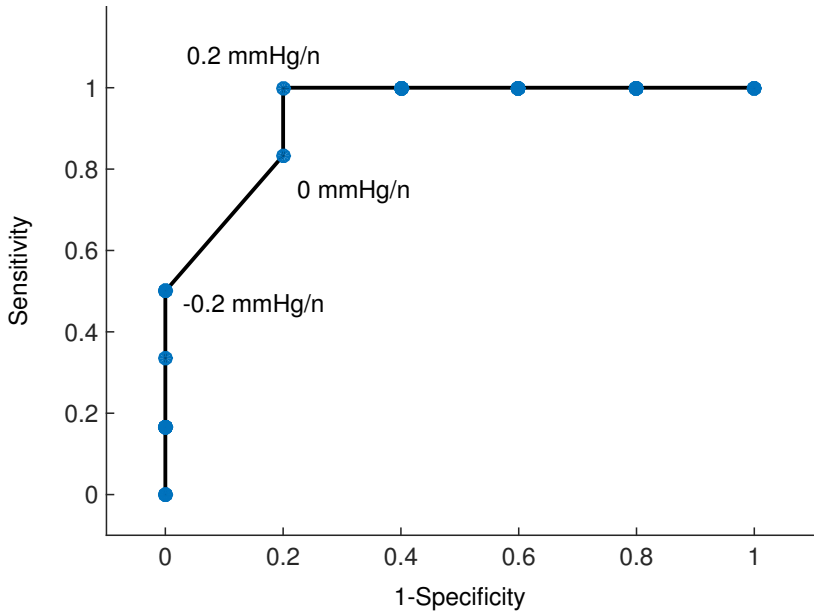

Figure 3.11: Receiver operating character curve for response slope at -10 mmHg of LBNP.

3.4 Discussion

In this study, new signal analysis techniques were applied to isolate individual low frequency constriction-dilation cycles in DAP and MSNA. Using these techniques, four primary indices, and two secondary indices were defined. The goal was to investigate the relationship between DAP and MSNA during LBNP, and to identify differences in this relationship between the finishers and non-finishers.

The mean number of MSNA bursts within single LF cycles showed a positive trend with increasing levels of LBNP, and were higher at -40 mmHg. This expected behaviour indicated that an increase of sympathetic outflow to increase peripheral resistance was a response to escalating levels of cardiovascular stress. Similar observations have been made in many previous studies,and its analogue here suggests that our selection criteria and analysis of these chosen LF cycles capture important well-known behaviours of the system.

Due to our selection of LF cycles with high DAP amplitude and high MSNA, this index was also able to capture at least some of the information that has previously been obtained with coherence analysis between DAP and MSNA. Indeed, if more MSNA bursts occur in concert with large DAP drops and increases during LF oscillations, the corresponding coherence would also be high. Increased DAP-MSNA coherence with graded LBNP has been reported [19].

In the finishers, although the mean number of MSNA bursts within single LF cycles rose during graded LBNP, the DAP response amplitudes did not. This result, along with the fact that the response slope was never different than zero in all LBNP levels, suggests that a finisher DAP-MSNA relationship could be characterized by a fixed desired DAP rise amplitude, mediated by a variable number of MSNA bursts. In other words, the system acts as if seeking to attain a particular rise in DAP, and provides just the necessary sympathetic activity.

In contrast, non-finishers' DAP rise amplitudes became larger at higher levels of LBNP. This result, along with a decreased response slope at -40 mmHg, suggests that the DAP-MSNA relationship of these participants was different than that of finishers. Under minimal stress, a higher response slope indicates that more MSNA bursts tend to result in a larger subsequent DAP rise. These results suggest that contrary to finisher group, where the sympathetic nervous system acts to obtain a precise DAP response, the non-finisher group modulates a variable DAP response with variable amounts of MSNA.

For non-finishers, a drop in response slope from 1.58 mmHg/n at -10 mmHg/n to -0.55 mmHg/n at -40 mmHg indicates an alteration in the DAP-MSNA relationship. Significant changes in cardiovascular variables such as DAP-MSNA coherence, MSNA, and heart rate have been reported during or before presyncope [30, 19, 12]. In all three, during or preceding presyncope, the system exhibits the opposite behaviour than would be expected in response

to cardiovascular stress. These results are analogous to our findings, wherein the nature of the relationship between DAP and MSNA inverts before presyncope.

The response slope receiver operating character curve for -10 mmHg of LBNP (Fig. 3.11) suggests that a threshold of 0.2 mmHg/n could distinguish most finishers from non-finishers. At that level of LBNP, all finishers had a response slope above 0.2, while only one non-finisher also did.

Stimulus slope remained constant for both groups in all levels of LBNP, and was statistically different from zero only for non-finishers at -20 mmHg. This indicates that the number of MSNA bursts per cycle was not related to the magnitude of the acute DAP drops in the LF band. Previous research has shown that the onset of MSNA volleys result from acute drops in DAP [25]. Along with our result showing decreasing SAP concurrent to increasing MSNA bursts per cycle, these would indicate that although MSNA volleys are caused by acute drops in DAP, their size may be modulated by a SAP moving average. It has been previously suggested that LBNP causes increased baroreceptor sensitivity in yet misunderstood ways [32].

Stimulus time values were within the physiological range of delay between carotid sinus nerve firing and muscle sympathetic nerve activity in the leg ($\approx$ 2 s, [23, 17]), although it is clear that stimulus time does not directly measure this delay. Stimulus time became progressively smaller for both groups as LNBP levels were increased, without differences between groups. These results either suggest that the nervous system reacted more aggressively to progressively smaller drops, and/or that reaction time became shorter. In this sense, the stimulus time index quantifies the sensitivity of the arterial baroreflex.

Response time values were within the physiological range of norepinephrine clearance rate in the arterial bed ($\geq$ 1.5 s, [24]). While no change was observed in the non-finishers, values for finishers were smaller at -40 mmHg than at -10 mmHg. These results suggest the existence of a stress adaptation mechanism for finishers which was not the case for non-finishers. This conclusion is supported by previous research showing norepinephrine transporter deficiency associated with orthostatic intolerance [33, 24, 34].

Our findings support previous work showing that sympathetic activity in the baroreflex is different in people who do not faint during intense LBNP versus people who do. Under minimal stress the response slope index, which corresponds to the arterial response to MSNA, was different between finishers and non-finishers. In settings such as the aerospace field, response slope could be used to characterize potential candidates for extreme environment assignments.

This study provides useful insight into the relationship between DAP and MSNA. It should be noted that MSNA is a technique that is all but absent in clinical settings, and demands often prohibitively high levels of expertise in laboratory settings. Further exploration of sympathogenic DAP fluctuations with these indices could provide information to

derive new techniques to quantify processes in the arterial branch of the baroreflex, which could be used to diagnose and monitor orthostatic hypotensive patients.

3.5 References

[1] A. Moya, R. Sutton, F. Ammirati, J.-J. Blanc, M. Brignole, J. B. Dahm, J.-C. Deharo, J. Gajek, K. Gjesdal, A. Krahn, *et al.*, "Guidelines for the diagnosis and management of syncope (version 2009) the task force for the diagnosis and management of syncope of the european society of cardiology (esc)," *European heart journal*, vol. 30, no. 21, pp. 2631–2671, 2009.

[2] J. M. Scott, B. T. Esch, L. S. Goodman, S. S. Bredin, M. J. Haykowsky, and D. E. Warburton, "Cardiovascular consequences of high-performance aircraft maneuvers: implications for effective countermeasures and laboratory-based simulations," *Applied physiology, nutrition, and metabolism*, vol. 32, no. 2, pp. 332–339, 2007.

[3] D. E. Watenpaugh and A. R. Hargens, "The cardiovascular system in microgravity," *Comprehensive Physiology*, 1996.

[4] H. Luukinen, K. Koski, P. Laippala, and K. Airaksinen, "Orthostatic hypotension and the risk of myocardial infarction in the home-dwelling elderly," *Journal of internal medicine*, vol. 255, no. 4, pp. 486–493, 2004.

[5] M. L. Eigenbrodt, K. M. Rose, D. J. Couper, D. K. Arnett, R. Smith, and D. Jones, "Orthostatic hypotension as a risk factor for stroke the atherosclerosis risk in communities (aric) study, 1987–1996," *Stroke*, vol. 31, no. 10, pp. 2307–2313, 2000.

[6] L. A. Lipsitz, F. C. Pluchino, J. Y. Wei, and J. W. Rowe, "Syncope in institutionalized elderly: the impact of multiple pathological conditions and situational stress," *Journal of chronic diseases*, vol. 39, no. 8, pp. 619–630, 1986.

[7] V. Cooper and R. Hainsworth, "Effects of head-up tilting on baroreceptor control in subjects with different tolerances to orthostatic stress," *Clinical science*, vol. 103, no. 3, pp. 221–226, 2002.

[8] R. Hainsworth, "Pathophysiology of syncope," *Clinical Autonomic Research*, vol. 14, no. 1, pp. i18–i24, 2004.

[9] V. E. Claydon and R. Hainsworth, "Salt supplementation improves orthostatic cerebral and peripheral vascular control in patients with syncope," *Hypertension*, vol. 43, no. 4, pp. 809–813, 2004.

[10] W. Wieling, F. J. de Lange, and D. L. Jardine, "The heart cannot pump blood that it does not receive," *Frontiers in physiology*, vol. 5, 2014.

[11] V. A. Convertino, "Neurohumoral mechanisms associated with orthostasis: reaffirmation of the significant contribution of the heart rate response," *Frontiers in physiology*, vol. 5, 2014.

[12] G. Gulli, V. L. Wight, R. Hainsworth, and A. Cevese, "Spectral and cross-spectral autoregressive analysis of cardiovascular variables in subjects with different degrees of orthostatic tolerance," *Clinical Autonomic Research*, vol. 11, no. 1, pp. 19–27, 2001.

[13] G. Gulli, V. L. Cooper, V. Claydon, and R. Hainsworth, "Cross-spectral analysis of cardiovascular parameters whilst supine may identify subjects with poor orthostatic tolerance," *Clinical science*, vol. 105, no. 1, p. 119, 2003.

[14] P. M. Stevens and L. E. Lamb, "Effects of lower body negative pressure on the cardiovascular system," *The American journal of cardiology*, vol. 16, no. 4, pp. 506–515, 1965.

[15] V. Convertino, "Lower body negative pressure as a tool for research in aerospace physiology and military medicine.," *Journal of gravitational physiology: a journal of the International Society for Gravitational Physiology*, vol. 8, no. 2, pp. 1–14, 2001.

[16] T. Hachiya, M. L. Walsh, M. Saito, and A. P. Blaber, "Delayed vasoconstrictor response to venous pooling in the calf is associated with high orthostatic tolerance to lbnp," *Journal of Applied Physiology*, vol. 109, no. 4, pp. 996–1001, 2010.

[17] K.-E. Hagbarth and Å. Vallbo, "Pulse and respiratory grouping of sympathetic impulses in human muscle nerves," *Acta physiologica Scandinavica*, vol. 74, no. 1-2, pp. 96–108, 1968.

[18] S. Iwase, T. Mano, A. Kamiya, Y. Niimi, Q. Fu, and A. Suzumura, "Syncopal attack alters the burst properties of muscle sympathetic nerve activity in humans," *Autonomic Neuroscience*, vol. 95, no. 1, pp. 141–145, 2002.

[19] W. H. Cooke, C. A. Rickards, K. L. Ryan, T. A. Kuusela, and V. A. Convertino, "Muscle sympathetic nerve activity during intense lower body negative pressure to presyncope in humans," *The Journal of physiology*, vol. 587, no. 20, pp. 4987–4999, 2009.

[20] T. Hachiya, I. Hashimoto, M. Saito, and A. P. Blaber, "Peripheral vascular responses of men and women to lbnp," *Aviation, space, and environmental medicine*, vol. 83, no. 2, pp. 118–124, 2012.

[21] S. Mayer, "Studien zur physiologie des herzens und der blutgefässe 6. abhandlung: Über spontane blutdruckschwankungen.," *Sitzungsberichte Akademie der Wissenschaften in*

Wien. Mathematisch-naturwissenschaftliche Classe, Anatomie, vol. 74, pp. 281–307, 1876.

[22] C. Julien, "The enigma of Mayer waves: facts and models," *Cardiovascular research*, vol. 70, no. 1, pp. 12–21, 2006.

[23] C. Borst and J. M. Karemaker, "Time delays in the human baroreceptor reflex," *Journal of the autonomic nervous system*, vol. 9, no. 2, pp. 399–409, 1983.

[24] C. Schroeder, J. Tank, M. Boschmann, A. Diedrich, A. M. Sharma, I. Biaggioni, F. C. Luft, and J. Jordan, "Selective norepinephrine reuptake inhibition as a human model of orthostatic intolerance," *Circulation*, vol. 105, no. 3, pp. 347–353, 2002.

[25] R. Furlan, A. Porta, F. Costa, J. Tank, L. Baker, R. Schiavi, D. Robertson, A. Malliani, and R. Mosqueda-Garcia, "Oscillatory patterns in sympathetic neural discharge and cardiovascular variables during orthostatic stimulus," *Circulation*, vol. 101, no. 8, pp. 886–892, 2000.

[26] J. Pan and W. J. Tompkins, "A real-time qrs detection algorithm," *Biomedical Engineering, IEEE Transactions on*, no. 3, pp. 230–236, 1985.

[27] A. Cevese, G. Gulli, E. Polati, L. Gottin, and R. Grasso, "Baroreflex and oscillation of heart period at 0.1 hz studied by α-blockade and cross-spectral analysis in healthy humans," *The Journal of Physiology*, vol. 531, no. 1, pp. 235–244, 2001.

[28] J. A. Taylor, D. L. Carr, C. W. Myers, and D. L. Eckberg, "Mechanisms underlying very-low-frequency rr-interval oscillations in humans," *Circulation*, vol. 98, no. 6, pp. 547–555, 1998.

[29] G. Sundlöf and B. Wallin, "Human muscle nerve sympathetic activity at rest. relationship to blood pressure and age," *The Journal of Physiology*, vol. 274, no. 1, pp. 621–637, 1978.

[30] M. Ichinose, M. Saito, N. Fujii, N. Kondo, and T. Nishiyasu, "Modulation of the control of muscle sympathetic nerve activity during severe orthostatic stress," *The Journal of physiology*, vol. 576, no. 3, pp. 947–958, 2006.

[31] M. H. Zweig and G. Campbell, "Receiver-operating characteristic (roc) plots: a fundamental evaluation tool in clinical medicine.," *Clinical chemistry*, vol. 39, no. 4, pp. 561–577, 1993.

[32] V. L. Cooper and R. Hainsworth, "Carotid baroreceptor reflexes in humans during orthostatic stress," *Experimental Physiology*, vol. 86, no. 5, pp. 677–681, 2001.

[33] G. Jacob, J. R. Shannon, F. Costa, R. Furlan, I. Biaggioni, R. Mosqueda-Garcia, R. M. Robertson, and D. Robertson, "Abnormal norepinephrine clearance and adrenergic receptor sensitivity in idiopathic orthostatic intolerance," *Circulation*, vol. 99, no. 13, pp. 1706–1712, 1999.

[34] J. R. Shannon, N. L. Flattem, J. Jordan, G. Jacob, B. K. Black, I. Biaggioni, R. D. Blakely, and D. Robertson, "Orthostatic intolerance and tachycardia associated with norepinephrine-transporter deficiency," *New England Journal of Medicine*, vol. 342, no. 8, pp. 541–549, 2000.

Chapter 4

Accurate and consistent automatic seismocardiogram annotation without concurrent ECG

> An indrik's howl is much subtler than its crushing foot. The sound is mundane, but inaudible vibrations scatter and sunder magical contrivances.
>
> *Simic research notes*

4.1 Introduction

Seismocardiography (SCG) is the measurement of thoracic vibrations recorded from accelerometers placed on the sternum. The signal was originally recorded by Roman Baevsky and used to monitor cosmonauts [1]. During the 90's Salerno and Zanetti used the technology for diagnosis of coronary artery disease [2]. Recent developments in MEMS accelerometer technology have rekindled research interest in the technique [3, 4].

Peaks observed in SCG have been related to significant cardiac events, the main ones being aortic valve opening (AO) and isovolumic moment (IM) during the systolic cycle, and aortic valve closure (AC) during the diastolic cycle (Fig. 4.1). The assignment of these fiducial points was based on concurrent echocardiogram analysis with SCG morphology [5, 6]. Precise cardiac mechanical timings that can only be obtained from SCG are critically dependent on accurate identification fiducial points [7, 8].

Heart rate variability (HRV) analysis is a practical and widely used noninvasive technique to study the autonomic control of the cardiovascular system [9]. The sympathetic and parasympathetic nervous systems have complementary excitatory and inhibitory effects on

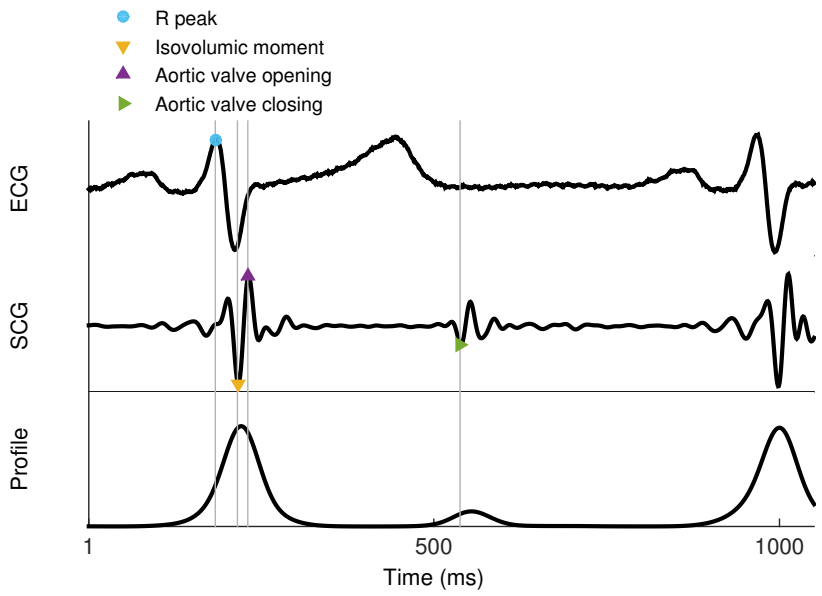

Figure 4.1: Example electrocardiogram (ECG), seismocardiogram (SCG), and SCG profile with relevant fiducial points. The profile is obtained from the Morlet wavelet transform of the SCG by isolating the frequency with highest power in the $[20, 60]$ Hz band, and returning its power in the time domain.

the heart, respectively. The interplay between these systems cause the heart rate to exhibit regular oscillations under normal conditions. These oscillations in the steady-state heart rate are dominated by 2 frequencies. In the low-frequency range of $[0.04, 0.15]$ Hz, baroreflex mediated oscillations are centered around a frequency of ≈ 0.1 Hz. These oscillations are largely due to time delays inherent to the processes involved in arterial constriction and dilation [10]. Because of this, power in this band is often used to quantify sympathetic activity [11, 12]. Likewise, oscillations in the high-frequency range of $[0.15, 0.4]$ Hz centered around the breathing frequency are mediated by respiratory sinus arrhythmia, and are often used to quantify vagal parasympathetic activity [13].

The heartbeat intervals (HBi) used for HRV analysis are predominantly obtained from electrocardiogram (ECG) R peaks, with some exceptions such as photoplethysmography (PPG) peaks [14]. Recently, mechanical cardiac signals have provided alternatives for HBi acquisition. SCG and Ballistocardiograms (BCG) are the primary examples of such signals. BCG measures the recoil of the body due to aortic blood circulation and can be recorded from weight scales and bed sensors [4]. The comparison of HRV indices obtained from alternative and conventional methods has been used to test the consistency of the HBi estimation.

The modern-day ubiquity of accelerometers in wearable devices and smart phones could make SCG an inexpensive data acquisition tool. Such devices have been used to obtain HBi [15, 16, 17], and the possibility of using SCG to obtain HRV indices has been reported

by us [18], and others [17, 19]. BCG has also been used to consistently measure heartbeat intervals [20, 21, 22]. Additionally, correctly annotated BCG has been shown to return valid HBi and HRV indices when compared to those obtained from ECG [23, 24] and PPG [25]. In all these studies, however, the identification algorithms either depended on concurrent R peak identification, or did not report the accuracy of fiducial point identification. The eventual use of SCG as a stand-alone application without concurrent ECG or PPG, either at home or in the laboratory, depends on the accurate and consistent automatic identification of fiducial points with minimal user input.

The goal of this study was to develop and test SCG fiducial point identification software capable of returning valid HRV indices, while requiring no input from the user. A core concept for the algorithm in question was the elaboration of a function model for systolic vibration cycles, as well as an optimization function capable of accurately fitting this model to the *in-vivo* signal.

Accuracy of fiducial point identification differs importantly from the consistency necessary to obtain valid HRV indices. While HRV depends on consistent beat-to-beat identification of any one feature in systolic cycles, precise mechanical timings depend on the accurate identification of a particular fiducial point. To this end, our team has been involved in the development of an algorithm capable of correct identification of ten IM points per five minutes of recording [26]. This study builds on these few identified points, filling the gaps between them.

In order to test the software's ability to correctly identify SCG fiducial points in a variety of settings, it was applied on dataset recorded from subjects who were exposed to lower body negative pressure (LBNP). Previous work on this dataset showed that HRV indices could be obtained from manually identified fiducial points.

A secondary goal of this study was to investigate changes in SCG morphology due to LBNP. Although the moments in time when some important features of SCG occur are identified, there remains a gap in our knowledge of the forces that cause them, and how they may be altered by variations in intra-thoracic pressures and volumes. In this regard, the model was used to propose some standard morphology which could then be compared to each *in-vivo* systolic vibration cycle.

4.2 Methods

4.2.1 Data collection and annotation

A total of 18 participants took part in this study, including three female and fifteen males, (age: 27.6 ± 1.7 years, weight: 71.2 ± 5.4 kg and height: $174.3 \pm \pm 3.2$ cm). None of the participants had any documented cardiac abnormality. Signals were recorded at the Aerospace Physiology Laboratory under an ethics approval from the Simon Fraser University

Research Ethics Board. Participants followed the informed consent procedure and signed consent forms.

Each participant's lower body was placed in a negative pressure chamber and sealed at the iliac crest. Vacuum was applied to the chamber to drop the box pressure to -20 mm Hg, -30 mm Hg, -40 mm Hg and -50 mm Hg progressively. The participants were kept at each stage for 5 minutes and were returned to normal pressure at the end of the -50 mm Hg stage. If a participant exhibited a sudden decrease in heart rate or blood pressure or if they expressed any discomfort and wanted to stop, the negative pressure was immediately terminated [7].

SCG was acquired by a high sensitivity accelerometer (Brüel Kjær model 4381, Nærum, Denmark) placed on the xiphoid process of the sternum. The participants were in the supine position and the signals were recorded in back-to-front direction, perpendicular to the body surface. The ECG signal was simultaneously acquired through the NI 9205 analog input module (National Instruments, Austin, TX).

The filter banks algorithm [27] was used to identify the QRS complexes of the ECG. On the SCG, IM and AO points were assigned as the local minimum and maximum following each R peak. The AC point was assigned as the local minimum in a window of radius 50 ms centred 350 ms after the Q-wave. The software annotations were imported to the HFM Waveform Analysis software (Heart Force Medical, Vancouver, Canada) and were manually corrected. An algorithm described in detail later in this paper (subsection 4.2.2) was then used to identify IM points without the use of R peaks.

It has been previously shown that HBi obtained with either AO points or IM points can be used to compute valid HRV indices. Since previous results indicated that IM identification is slightly more consistent than AO identification [26], our algorithm was tested on its ability to identify IM points.

HBi obtained from R peaks and IM points were computed and resampled at 5Hz using a shape-preserving piecewise cubic interpolation method (Fig. 4.2).

For all LBNP levels and participants, the frequency spectrum of the filtered HBi time series was computed using Welch's method [28] (Fig. 4.2), and computed normalized frequency-domain HRV indices. Frequency-domain indices were chosen over time-domain indices to reflect their dominant use in research on cardiac autonomic control. Normalized indices were chosen over absolute indices since the former are unreliable for comparisons between individuals [9].

To quantify the accuracy of the algorithm, the time difference between hand-annotated and automatically annotated IM points was computed. For each IM point obtained by hand, the closest IM point obtained automatically was identified. To prevent comparisons in heart cycles where noise prevented automatic identification of IM points, or where ECG noise prevented identification of the R peak, the minimum heart period using IM points

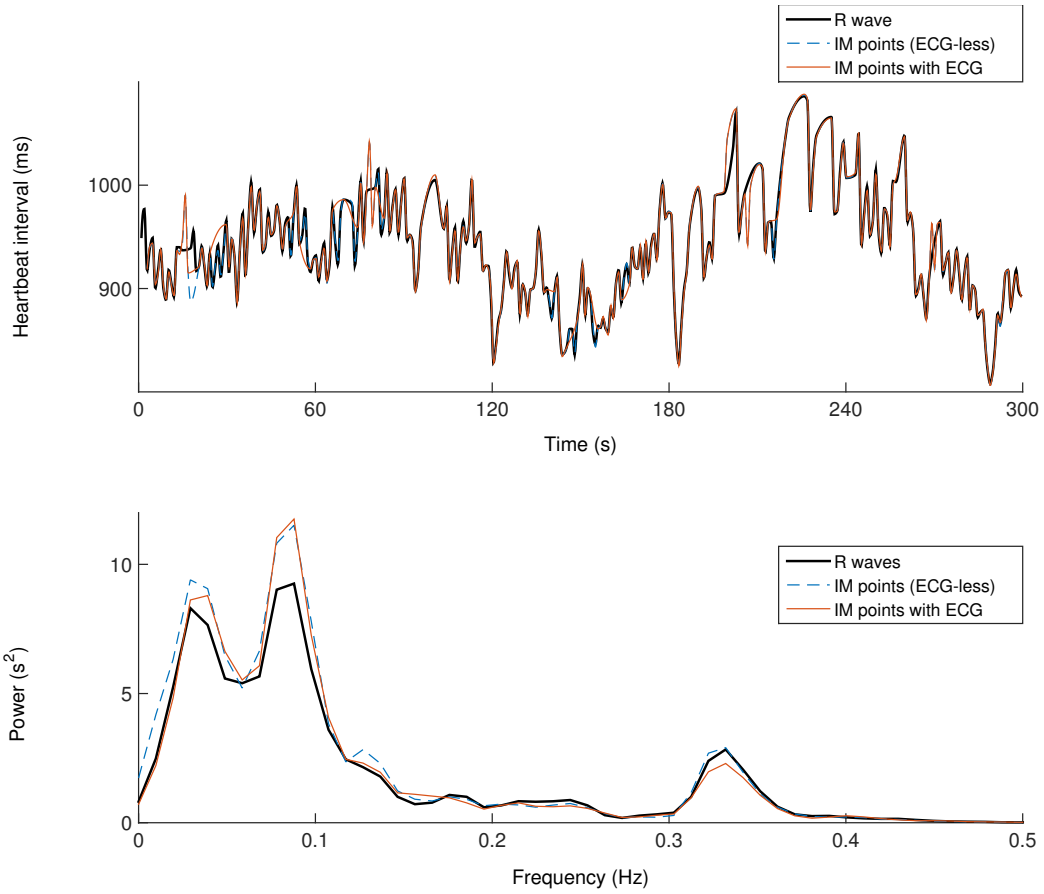

Figure 4.2: **Top** Example heartbeat interval time series, resampled at 5Hz, using R peaks, automatically identified isovolumic moments, and hand-identified isovolumic moments using ECG. **Bottom** Power spectra of the above time series. Through heart rate variability indices, these spectra are used to quantify autonomic control of the heart.

obtained by hand was computed. Only the pairs of IM points that differed in time by less than 2/3 the minimum HBi were then kept.

Signal analysis was performed with Matlab 2014b (Mathworks, MA, USA), and statistical analysis with JMP 11.2 (SAS Institute Inc, NC, USA). Values reported are mean ±95% confidence interval. Confidence interval was computed as 1.95 times the standard error within the LBNP level.

4.2.2 Detailed identification algorithm

All SCG signals were pre-annotated using a previously described algorithm [26] which uses two envelopes: the first replaces the ECG R peak and the second finds the approximate location of the IM point with respect to the first envelope peak. The output of the algorithm returns 10-second segments of annotated SCG separated by gaps of at least 2 seconds to avoid overlap.

The algorithm described below was developed to fill in these 2-second gaps and refine the overall estimation (Fig. 4.3).

1. *Beat-to-beat rejection*

   (a) *Computation the SCG wavelet profile.* This process created a time series used to identify AO and AC cycles.

   A Morlet wavelet transform of order 6 was performed on the filtered SCG signal. The sum of the resulting time-frequency power over time was then obtained,

   $$S(f) = \sum_t |\tilde{s}(t, f)|, \tag{4.1}$$

   where $\tilde{s}(t, f)$ is the wavelet transform of the signal$s$. The frequency f_p where S attained its maximum was computed such that

   $$S(f_p) = \max\big(S(f)\big). \tag{4.2}$$

   The profile P was then computed as the mean power for the frequencies around f_p,

   $$P(t) = \sum_{f_{p-2}}^{f_{p+2}} \tilde{s}(t, f)/5. \tag{4.3}$$

   Five frequencies were included instead of one to mitigate mistakes caused by *maximum likelihood estimators* (see Chapter 2).

   (b) *Rejection of estimates using HBi.* HBi was computed for each 10-second section. If successive intervals differed by more than a threshold value T, they were rejected.

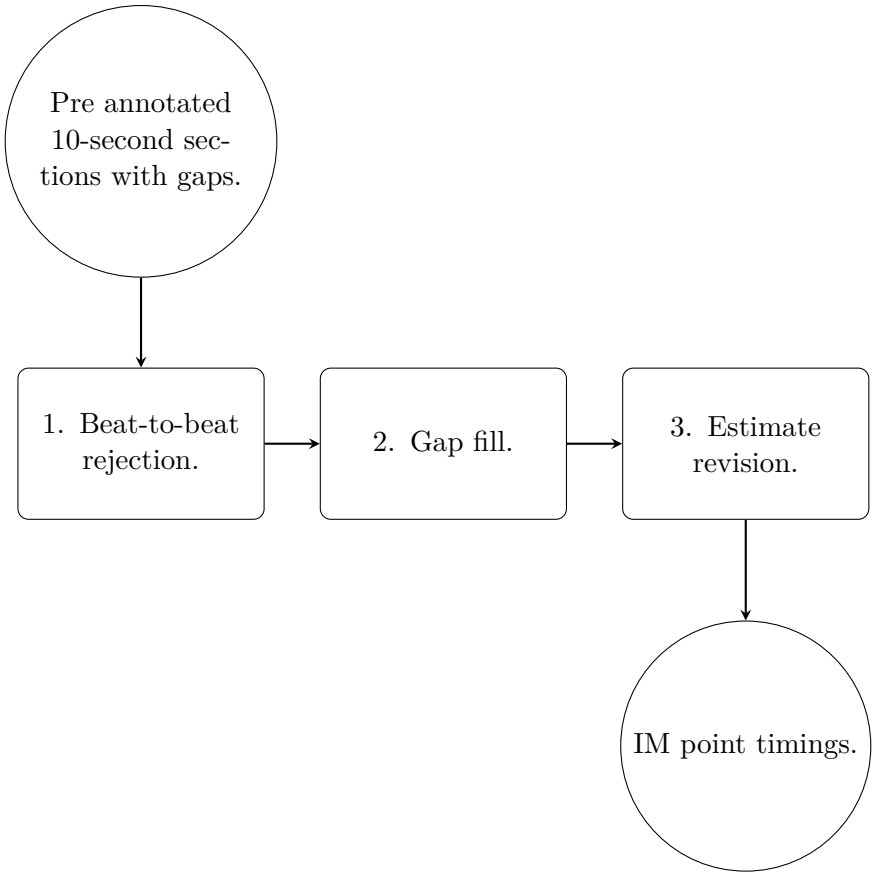

Figure 4.3: Summary of the isovolmic moment (IM) point identification algorithm. The input are a few very good estimates of IM points that come from a previously described algorithm and [26]. The first step rejects the set of initial estimates in which sufficient confidence was not attained. The second step fills the gaps between these few very good estimates. The last step uses the estimates, which are close to IM points, to predict the exact location of the IM points.

If 3 or more consecutive heart beats did not deviate from each other by more than T, they were kept.

This process assumed that heart period rarely changes by more than some threshold T in a single beat. Here, T was set as 3 times the interquartile range of HBi including all sections if this value was $\in [120, 300]$ ms. Otherwise, it was set at either 120 or 300 ms, whichever was closest. The threshold T is purposely low to favour false negatives over false positives.

$$T = \begin{cases} 3 \cdot iqr(\text{HBi}) & \text{if } 3 \cdot iqr(\text{HBi}) \in [120, 300] \\ 300 & \text{if } 3 \cdot iqr(\text{HBi}) > 300 \\ 120 & \text{if } 3 \cdot iqr(\text{HBi}) < 120, \end{cases} \tag{4.4}$$

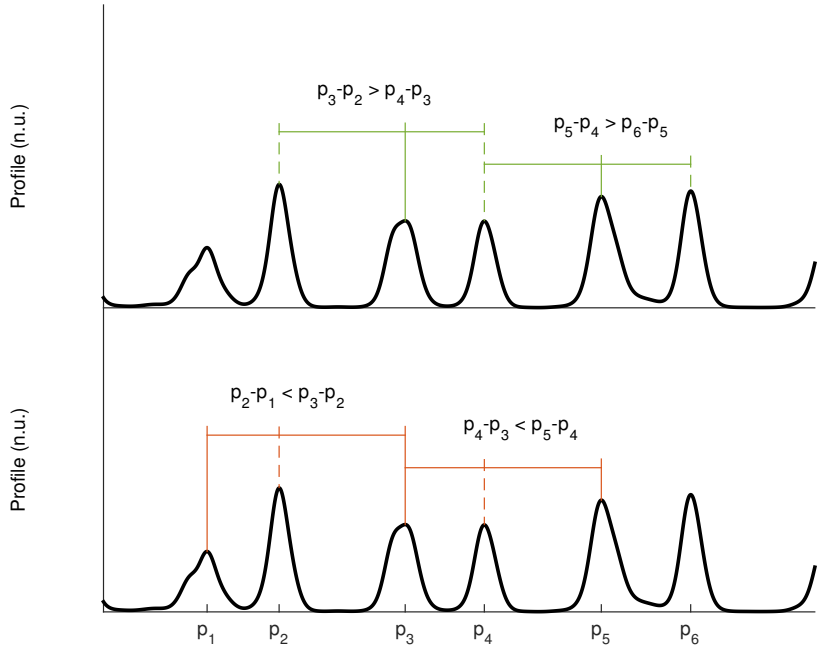

Figure 4.4: Example SCG profile showing exclusion criterion for aortic valve closure (AC) peaks labeled mistakenly as aortic valve opening (AO) peaks. Here, odd peaks $\{p_1, p_3, p_5\}$ are AO, and even peaks $\{p_2, p_4, p_6\}$ are AC. **Top** Correctly identified AO peaks are closer to the next AC peak than the previous AC peak. **Bottom**. Incorrectly identified AC peaks are closer to the previous AO peak than the next AO peak.

where *iqr* is the inter-quartile range. The interquartile range was chosen for its ability to ignore outliers.

(c) *Rejection of estimates that look like diastolic cycles.* The misidentification of AC cycles as AO cycles for entire sections was a recurrent problem. Because such systematic misidentifications did not affect HBi, and thus did not affect T, another rejection criterion had to be designed.

For each identified profile peak p_n in the section, the profile peaks directly before (p_{n-1}) and after it (p_{n+1}) were identified. For the section, if $p_n - p_{n-1} < p_{n+1} - p_n$ for all initially identified peaks, the the section was rejected (Fig. 4.4). This process assumed that AO cycles were closer to the subsequent AC cycle than to the preceeding AC cycle.

This process was repeated after each other step.

2. *Gap fill.* The previously described algorithm used to obtain initial IM estimates automatically rejected sections of the signal where it was not sufficiently confident [26]. Because of this, the algorithm sometimes left large gaps in the IM identifications.

   The gap filling process relied on minimizing the standard deviation of the HBi time series, taking into account the sections immediately preceding and following the gap.

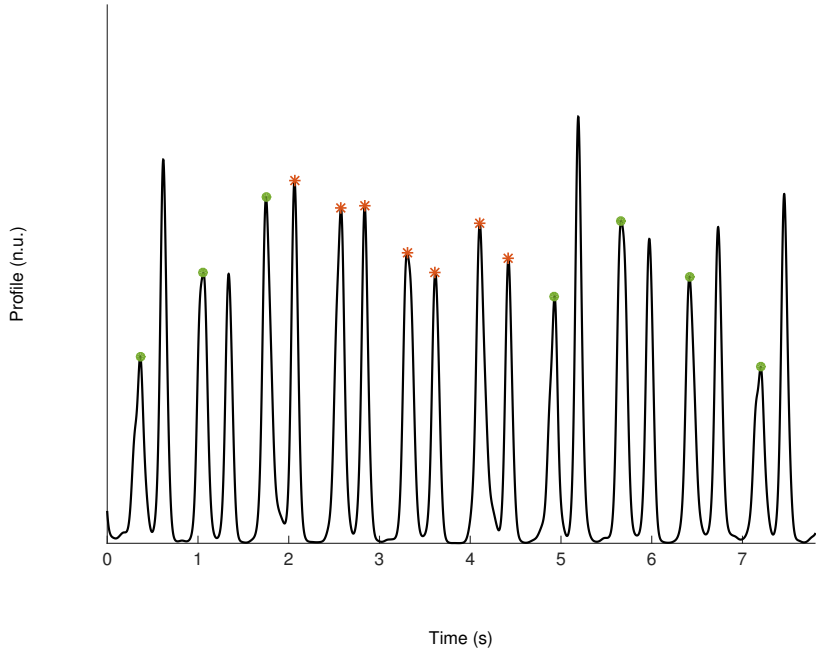

Figure 4.5: Seismocardiogram (SCG) profile with previously identified aortic valve opening (AO) peaks in green circles and gap-filling candidates for AO peaks in red asterisks. To identify which candidates were correct, the heart period time series was computed using the previously identified AO peaks and all possible candidate combinations. The correct candidates were then identified as the combination that minimized the standard deviation of the heart period.

For a given gap, candidate AO peaks were identified as local maxima higher than half the median of the relevant sections (Fig. 4.5). The sections immediately preceding and following the gap were appended with all possible combinations of the candidates. For each combination, standard deviation of HBi was computed. The set of candidates that minimized the standard deviation were kept for further analysis. This process relied on the assumption that the fluctuations in HBi over a limited time are small.

If a gap between sections was longer than 10 s, the process proceeded analogously to the manner previously described, but included only the section immediately preceding the gap and 3 s of the beginning of the gap profile. This initial narrowing of the gap was followed by the same technique, but including the section immediately following the gap and 3 s of the ending of the gap profile. This gap-narrowing process was repeated until the gap became shorter than 10 s.

3. *Estimate revision.*

   (a) *Fit of a model to the participant's median systolic cycle.* This process assumed that at least half of the profile peaks correctly identified systolic cycles, and that the absolute maximum of the SCG during systolic cycles is consistent in time.

For each profile peak, the absolute maximum if the SCG signal within a 200 ms radius was identified. 400 ms segments of the SCG signal were then centered around those maxima, and computed their median (Fig. 4.6 **Top**). The resulting median was normalized by dividing it by its maximum absolute value. The normalized median was windowed by the function $\exp(-(t/100)^2)$ to isolate the relevant vibrations.

The model was defined as the function

$$f(t, x_0, p, \phi_i) = A \cdot \sin\left((t - x_0) \cdot \frac{2\pi}{p}\right) \cdot \sum_{1}^{5} \phi_i \tag{4.5}$$

where A normalized the maximum to 1, t was time, x_0 was the time shift which is constrained to $[-30, 30]$ ms and represented the point exactly between IM and AO, p was the period which was constrained to $[20, 60]$ ms, and each ϕ_i was a compactly supported gaussian modulating the mitral closure (MC), IM, AO, and post-AO peaks, as well as a decay gaussian. The width of the gaussians was p for $i \in \{1, 5\}$ and $p/2$ for $i \in \{2, 3, 4\}$. The gaussians were centered at the MC, IM, AO, post-AO, and post-post-AO peaks, respectively. The amplitudes of the gaussians were constrained, respectively from left to right, to $[0.1, 0.6]$, $[0.3, 1]$, $[0.9, 1]$, $[0.1, 1]$, and $[0.1, 1]$. The amplitude constraints were designed from repeated observation to emulate normal signal morphology.

To determine the initial values of the parameters, the 2 SCG segment minima, and 2 SCG segment maxima that differed by at least 20 ms were identified. By comparing the timings of these extrema it was determined if the left-most minima was a MC point or an AO point. The initial period p was then set to be the distance between these 2 minima, and either the MC and AO amplitudes, or the AO and post-post-AO amplitudes to their respective SCG segment minima values. The initial IM and post-AO amplitudes were set to their respective SCG segment maxima values. If the minima were not both below 0.6, he initial values were set to by default to $p = 40$, and amplitudes $= \{0.2, 0.8, 0.9, 0.5, 0.1\}$.

The model was fitted by a simplex search method [29], implemented in Matlab as fminsearch, to minimize a distance function D defined as

$$D = \frac{d_1}{p} \cdot \sum_{t} w(t) \cdot d_2(t), \tag{4.6}$$

where d_1 is the mean distance between the 2 maxima and 2 minima of the model and signal, respectively, d_2 is the square point-wise difference between the signal and the model, and $w(t)$ is a weighing function that favours the beginning of the cycle over its end. The weighing function $w(t)$ was necessary because, while inter-participant differences in the beginning of systolic cycles are minimal, differences

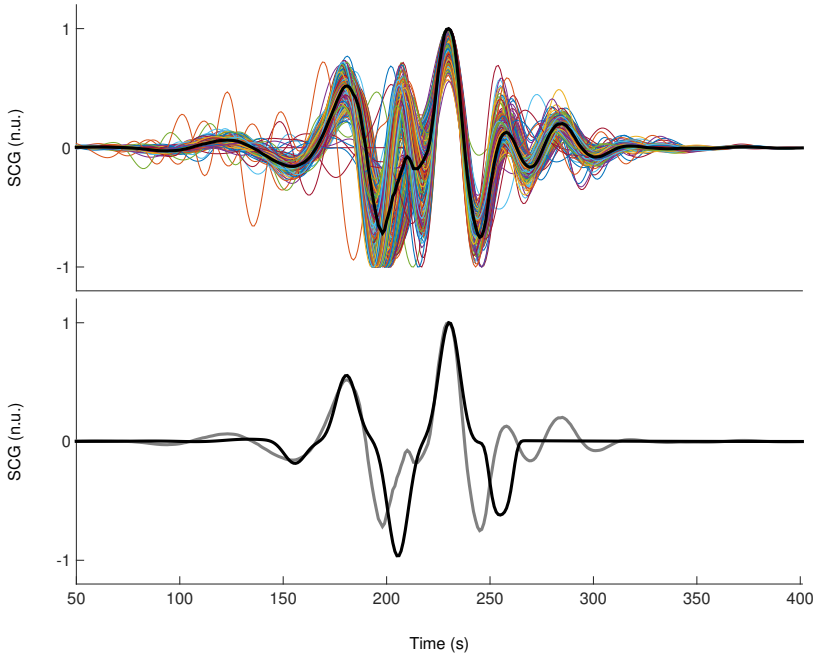

Figure 4.6: **Top** Seismocardiograms (SCG) within 200 ms of all identified profile peaks of a single participant, centered around their absolute maximums. The median of the resulting signals is shown (black). Identifying fiducial points to local maxima or minima is a standard technique for automatic identification [15, 16, 17, 19] and for this participant would return at least some misidentified peaks. **Bottom** The median SCG obtained above (grey) with its corresponding model (black). The model is the function in equation 4.5 with $x_0 = -8$ ms, $p = 50$ ms, and the amplitudes of the gaussians $= \{0.2, 0.5, 0.9, 1, 0.8\}$, respectively.

in their end are substantial. The weighing function $w(t)$ was then designed as a decaying sigmoid defined as

$$w(t) = 0.8 \cdot \tan^{-1}\Big(-0.05 \cdot (t - (3.5 \cdot p))\Big) + 1.2. \tag{4.7}$$

The model resulting from this process was assumed to represent a generic systolic cycle for the participant, for the particular LBNP level.

(b) *Fit of a model to each systolic cycle.* This process fitted the generic model obtained in step 4 to all systolic cycles of the participant, for a particular level of LBNP. For each identified profile peak, the distance function D (Equation 4.6) was minimized with respects to x_0 (Equation 4.5).

This process implicitly returned timing estimates for MC, IM, and AO points.

(c) *Refinement of each estimate.* While IM points are always local SCG minima, the initial timings estimates are often a slight distance from the nearest minimum. For each IM estimate, the SCG minimum within a window of radius $p/4$ was identified. The estimate was then moved to the identified minimum and repeated these steps until a minimum relative to the window was reached .

4.3 Results

Across LBNP levels and subjects, a median of 6% of the the automatically annotated IM points did not have a hand-annotated IM points in the same cardiac cycle. A median of 17% of the hand-annotated IM points did not have automatically annotated IM points in the same cardiac cycle. These points could not be tested for accuracy.

IM points identified by hand were compared to those identified automatically. For each LBNP level and each subject, the percentage of accurately identified IM points was computed. An identification was considered accurate when the difference between the timing of the hand-identified IM point and the automatically identified IM point was 0. Mean

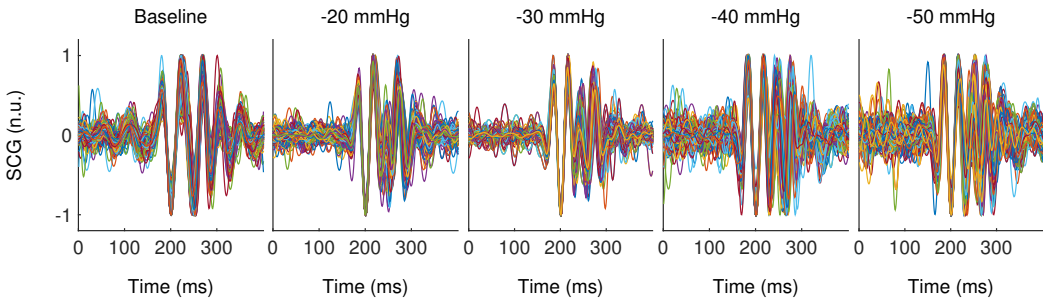

Figure 4.7: All systolic cycles for one participant across all levels of LBNP. Each cycle was centered at the hand-identified isovolumic moment fiducial point.

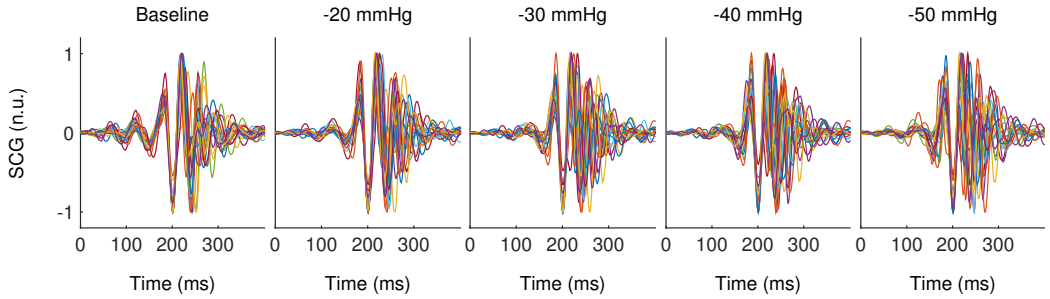

Figure 4.8: Median systolic cycles for all participants across all levels of LBNP. Each median cycle was centered at the hand-identified isovolumic moment fiducial point.

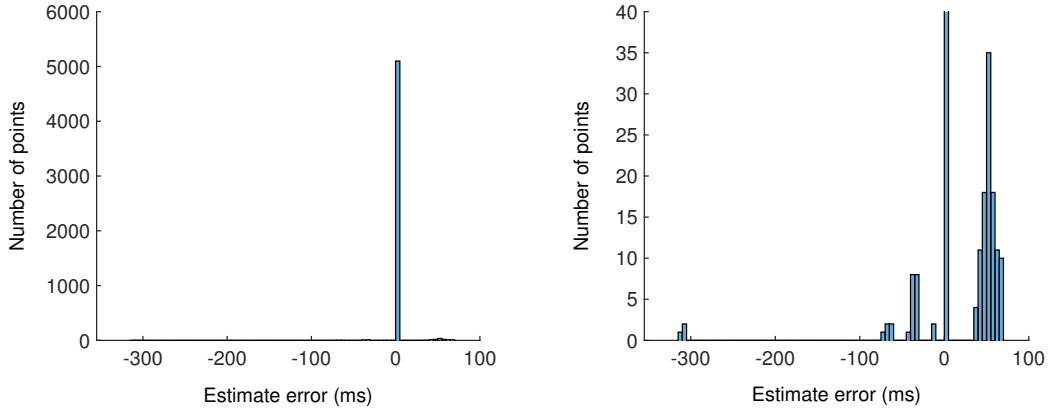

Figure 4.9: Histogram of the estimation errors of the algorithm at baseline for all participants. The mean error is 0.72 ± 0.30 ms. **Right** A truncated version of the histogram on the **left** highlighting the inaccuracies. The groups of errors centered at $\approx \pm 50$ ms represent errors wherein either the previous or subsequent peaks were misidentified as the isovolumic moments. The few errors near -300 ms represent diastolic cycles mistaken for systolic cycles.

accuracies for increasing levels of LBNP were $97.61 \pm 3.39\%$, $93.32 \pm 5.33\%$, $78.28 \pm 14.29\%$, $58.68 \pm 17.58\%$, $63.36 \pm 14.23\%$.

The HRV ratio LF/HF was computed for each level of LBNP and all subjects. Indices obtained with IM points were compared to those obtained from RR intervals. For indices obtained from hand annotations, the mean differences were -0.08 ± 0.34, -0.24 ± 0.50, -0.34 ± 0.43, -0.70 ± 0.64, and -1.07 ± 0.77 for increasing levels of LBNP. For indices obtained from automatic annotations, the mean differences were 0.16 ± 0.19, -0.10 ± 0.58, 0.89 ± 0.85, -1.22 ± 0.62, 2.30 ± 1.10 for increasing levels of LBNP.

For LF/HF measurements, LF-HF power balance obtained with IM points were compared to those obtained from RR intervals. If both values were either above 1 or below 1, the balance was deemed accurate. For hand annotations, the number of participants with accurately identified balance was 17, 16, 18, 17, and 17 for increasing levels of LBNP ($N = 18$).

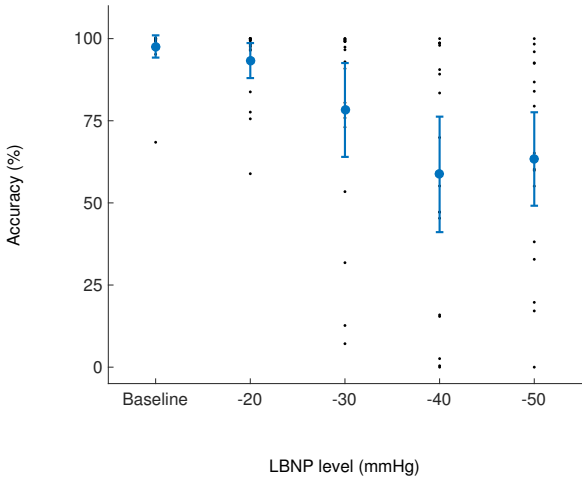

Figure 4.10: Mean accuracy of isovolumic moment (IM) identification for each level of lower body negative pressure (LBNP). For each subject, accuracy is computed as the percentage of automatically annotated IM points that are identical to hand-annotated IM points. Values are given as mean ± confidence interval.

For automatic identification, the number pf participants with accurately identified balance was 17, 16, 17, 18, and 16 for increasing levels of LBNP ($N = 18$).

HF norm was computed for each level of LBNP and all subjects. Indices obtained with IM points were compared to those obtained from RR intervals. For HF indices obtained from hand annotations, the mean differences were 0.2 ± 1.9 %, 0.8 ± 3.1 %, 1.4 ± 1.8 %, 1.9 ± 2.0 %, and 1.7 ± 1.3 % for increasing levels of LBNP, whereas for HF indices obtained from automatic annotations, the mean differences were -1.2 ± 1.6 %, 1.0 ± 4.3 %, -4.7 ± 3.8 %, -6.0 ± 3.2 %, -9.1 ± 4.6 % for increasing levels of LBNP.

LF norm was computed for each level of LBNP and all subjects. Indices obtained with IM points were compared to those obtained from RR intervals. For LF indices obtained from hand annotations, the mean differences were -0.3 ± 2.0 %, -1.3 ± 3.4 %, -1.6 ± 1.8 %, -2.1 ± 2.0 %, and -1.9 ± 1.4 % for increasing levels of LBNP, whereas for LF indices obtained from automatic annotations, the mean differences were 1.2 ± 1.9 %, -1.2 ± 4.7 %, 5.1 ± 3.9 %, 6.1 ± 3.7 %, 9.6 ± 4.8 % for increasing levels of LBNP.

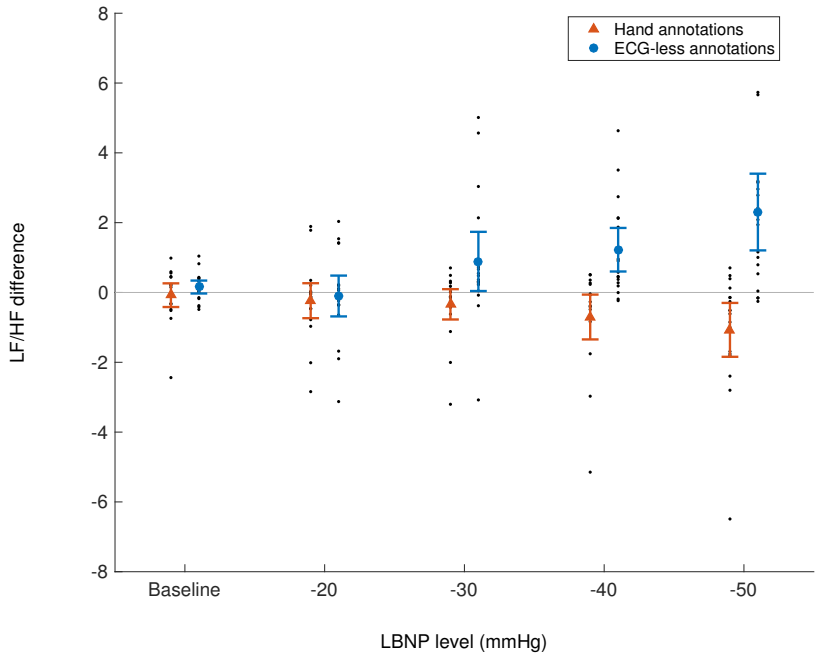

Figure 4.11: Mean differences between the low-frequency to high-frequency power ratio (LF/HF) computed from heartbeat interval (HBi) time series obtained from R peaks and isovolumic moments (IM) for all levels of lower body negative pressure (LBNP). Values shown are mean ± confidence interval.

4.4 Discussion

A new algorithm for the identification of the IM fiducial point on SCG without the use of ECG was tested in its accuracy and consistency across levels of LBNP.

The methodology described in this study uses new techniques, 2 of which distinguish themselves importantly from previously described algorithms. Firstly, the systolic cycle model was able to overcome the difficulties created by multiple extrema in the vicinity of true fiducial points. The modelling also allows for concurrent estimation of all systolic fiducial points, as well as a representation of participants' general SCG morphology. Secondly, the distance function that was minimized to fit the model took into account the square difference, the distances between the 2 highest and 2 lowest peaks, as well as a weighing function penalizing the earlier portion of each systolic vibration cycle. This distance function successfully mitigated different kinds of systematic errors by counter-balancing them with other ways to compute distance.

The accuracy of IM identification was tested by the comparison of the timings obtained automatically to timings obtained by hand-identification. This accuracy reached above 97 and 93% when analyzed at baseline and -20 mmHg of LBNP, respectively. At baseline, 17 participants in a total of 18 had an identification accuracy of over 95%. These levels would be largely sufficient for applications that require either the exact amplitude,frequency, or

timing of the systolic SCG fiducial points. As such, it could provide sufficient data to track changes in cardiac function during hemorrhage [7].

The consistency of the IM point identification was tested by comparing HRV indices as obtained from R peaks to those obtained from hand-identified IM points and automatically identified IM points. At baseline and -20 mmHg of LBNP, these indices were not statistically different from 0. They had small mean difference, small standard error and most importantly, 17 and 16 participants out of a total of 18 had an accurately estimated LF-HF balance. This supports the claim that the algorithm is consistent enough to perform HRV analysis without concurrent signals or timings.

The algorithm became much less accurate and consistent at levels of LBNP higher than -20 mmHg. Figure 4.7 shows that higher levels of LBNP create more noise in the signal. For this example participant, higher levels of LBNP also created vibration peaks with amplitudes comparable to those of fiducial points throughout the cycle. Noise and non-fiducial peaks of high amplitude are important sources of error for the algorithm. They both modify the profile, making it vary from the norm, and create errors in model fitting. Figure 4.8 shows that these changes are not consistent across participants, and so might depend on individual physiology.

It is possible that the changes in intra-thoracic pressure and volume caused by LBNP affect the mechanical properties of the heart and other constituent tissue through which these vibrations propagate. The relation between SCG fiducial points and valve openings was shown for subjects at rest and could potentially be altered during LBNP. Regardless of these hypotheses, the results show that the algorithm requires sophistication to adapt itself to situations of high cardiovascular and orthostatic stress.

In supine position at low levels of LBNP, such as is the case the algorithm was both accurate enough to obtain precise IM timings, and consistent enough to obtain meaningful HRV indices. The results open opportunities for stand-alone applications of SCG for home use as well as in laboratories.

4.5 References

[1] R. M. Baevsky, A. D. Egorov, and L. A. Kazarian, "The Method of Seismocardiography," *Kardiologiia*, vol. 18, pp. 87–9, Jan. 1964.

[2] D. Salerno, J. M. Zanetti, L. Poliac, R. Crow, P. Hannan, K. Wang, I. Goldenberg, and R. Van Tassel, "Exercise Seismocardiography for Detection of Coronary Artery Disease," *American Journal of Noninvasive Cardiology*, pp. 321–330, 199.

[3] J. M. Zanetti and K. Tavakolian, "Seismocardiography : Past , Present and Future," in *IEEE Engineering in Medicine and Biology Society Conference*, (Osaka, Japan), pp. 7004–7007, 2013.

[4] O. Inan, P.-F. Migeotte, K.-S. Park, M. Etemadi, K. Tavakolian, R. Casanella, J. Zanetti, J. Tank, I. Funtova, K. Prisk, and M. Di Rienzo, "Ballistocardiography and Seismocardiography: A Review of Recent Advances," *IEEE Journal of Biomedical and Health Informatics*, vol. 30308, no. c, pp. 1–1, 2014.

[5] R. Crow, P. Hannan, D. Jacobs, L. Hedquist, and D. Salerno, "Relationship between seismocardiogram and echocardiogram for events in the cardiac cycle," *American journal of Noninvasive Cardiology*, vol. 8, no. 39, pp. 39–46, 1994.

[6] K. Tavakolian, A. Blaber, B. Ngai, and B. Kaminska, "Estimation of hemodynamic parameters from seismocardiogram," in *Computing in Cardiology*, (Belfast), pp. 1055–1058, 2010.

[7] K. Tavakolian, G. A. Dumont, G. Houlton, and A. P. Blaber, "Precordial vibrations provide noninvasive detection of early-stage hemorrhage," *Shock*, vol. 41, no. 2, pp. 91–96, 2014.

[8] D. M. Salerno and J. Zanetti, "Seismocardiography for monitoring changes in left ventricular function during ischemia.," *CHEST Journal*, vol. 100, no. 4, pp. 991–993, 1991.

[9] Task Force of the European Society of Cardiology *et al.*, "Heart rate variability standards of measurement, physiological interpretation, and clinical use," *Eur Heart J*, vol. 17, pp. 354–381, 1996.

[10] C. Julien, "The enigma of Mayer waves: facts and models," *Cardiovascular research*, vol. 70, no. 1, pp. 12–21, 2006.

[11] J. P. Saul, R. Berger, P. Albrecht, S. Stein, M. H. Chen, and R. Cohen, "Transfer function analysis of the circulation: unique insights into cardiovascular regulation," *American Journal of Physiology-Heart and Circulatory Physiology*, vol. 261, no. 4, pp. H1231–H1245, 1991.

[12] P. Van De Borne, M. Rahnama, S. Mezzetti, N. Montano, A. Porta, J. P. Degaute, and V. K. Somers, "Contrasting effects of phentolamine and nitroprusside on neural and cardiovascular variability," *American Journal of Physiology-Heart and Circulatory Physiology*, vol. 281, no. 2, pp. H559–H565, 2001.

[13] D. L. Eckberg, "Human sinus arrhythmia as an index of vagal cardiac outflow," *Journal of Applied Physiology*, vol. 54, no. 4, pp. 961–966, 1983.

[14] M. Bolanos, H. Nazeran, and E. Haltiwanger, "Comparison of heart rate variability signal features derived from electrocardiography and photoplethysmography in healthy

individuals," in *Engineering in Medicine and Biology Society, 2006. EMBS'06. 28th Annual International Conference of the IEEE*, pp. 4289–4294, IEEE, 2006.

[15] M. Di Rienzo, E. Vaini, B. Bruno, P. Castiglioni, P. Lombardi, G. Parati, C. Lombardi, P. Meriggi, and F. Rizzo, "Wearable seismocardiography: Towards the beat-to-beat assessment of cardiac mechanics during sleep in microgravity," *2014 8th Conference of the European Study Group on Cardiovascular Oscillations, ESGCO 2014*, pp. 239–240, 2014.

[16] M. Di Rienzo, E. Vaini, P. Castiglioni, P. Lombardi, P. Meriggi, and F. Rizzo, "A Textile-Based Wearable System for the Prolonged Assessment of Cardiac Mechanics in Daily Life," in *IEEE EMBC*, pp. 6896–6898, 2014.

[17] J. Ramos-Castro, J. Moreno, H. Miranda-Vidal, M. a. García-González, M. Fernández-Chimeno, G. Rodas, and L. Capdevila, "Heart rate variability analysis using a seismocardiogram signal.," *Conference proceedings: Annual International Conference of the IEEE Engineering in Medicine and Biology Society. IEEE Engineering in Medicine and Biology Society. Conference*, vol. 2012, pp. 5642–5, 2012.

[18] A. Laurin, A. Blaber, and K. Tavakolian, "Seismocardiograms return valid heart rate variability indices," in *Computing in Cardiology Conference*, pp. 413–416, 2013.

[19] M. J. Tadi, E. Lehtonen, T. Koivisto, M. Pankaala, A. Paasio, and M. Teras, "Seismocardiography: Toward heart rate variability (hrv) estimation," in *Medical Measurements and Applications (MeMeA), 2015 IEEE International Symposium on*, pp. 261–266, IEEE, 2015.

[20] J. Paalasmaa, H. Toivonen, and M. Partinen, "Adaptive heartbeat modelling for beat-to-beat heart rate measurement in ballistocardiograms," *IEEE Journal of Biomedical and Health Informatics*, vol. 2194, pp. 1–8, 2014.

[21] D. Friedrich, X. L. Aubert, H. Führ, and A. Brauers, "Heart rate estimation on a beat-to-beat basis via ballistocardiography - A hybrid approach," *2010 Annual International Conference of the IEEE Engineering in Medicine and Biology Society, EMBC'10*, pp. 4048–4051, 2010.

[22] J. H. Shin, B. H. Choi, Y. G. Lim, D. U. Jeong, and K. S. Park, "Automatic ballistocardiogram (BCG) beat detection using a template matching approach.," *Conference proceedings: Annual International Conference of the IEEE Engineering in Medicine and Biology Society.*, vol. 2008, no. c, pp. 1144–1146, 2008.

[23] J. H. Shin, S. H. Hwang, M. H. Chang, and K. S. Park, "Heart rate variability analysis using a ballistocardiogram during Valsalva manoeuvre and post exercise.," *Physiological measurement*, vol. 32, no. 8, pp. 1239–1264, 2011.

[24] C. Brueser, S. Winter, and S. Leonhardt, "Unsupervised heart rate variability estimation from ballistocardiograms," *International Journal on Bioelectromagnetism*, vol. 15, no. 1, pp. 1–6, 2013.

[25] E. Pinheiro, O. Postolache, and P. Girão, "Blood pressure and heart rate variabilities estimation using ballistocardiography," *Proceedings of the 7th Conf. on. Telecom.*, pp. 125–128, 2009.

[26] F. Khosrow-khavar, K. Tavakolian, A. Blaber, J. M. Zanetti, R. Fazel-Rezai, and C. Menon, "Automatic annotation of seismocardiogram with high frequency precordial accelerations," *IEEE Journal of Biomedical and Health Informatics*, vol. 19, no. 4, 2014.

[27] V. X. Afonso, W. J. Tompkins, T. Q. Nguyen, and S. Luo, "ECG beat detection using filter banks.," *IEEE Transactions on Biomedical Engineering*, vol. 46, pp. 192–202, Feb. 1999.

[28] P. D. Welch, "The use of fast Fourier transform for the estimation of power spectra: A method based on time averaging over short, modified periodograms," *IEEE Transactions on Audio and Electroacoustics*, vol. 15, no. 2, pp. 70–73, 1967.

[29] J. C. Lagarias, J. A. Reeds, M. H. Wright, and P. E. Wright, "Convergence properties of the Nelder–Mead simplex method in low dimensions," *SIAM Journal on Optimization*, vol. 9, no. 1, pp. 112–147, 1998.

Chapter 5

3D models of the thorax for seismocardiography

> Drafna, founder of the College of Lat-Nam, could create a working model from even the smallest remnants of a newly unearthed artifact.
>
> *MTG, Drafna's Restoration*

5.1 Introduction

Seismocardiography (SCG) is the measurement of low-frequency (<0.25 Hz) sternum vibrations caused by the beating of the heart. The signal was originally recorded by Roman Baevsky and used to monitor cosmonauts [1]. During the 90's Salerno and Zanetti used the technology for diagnosis of coronary artery disease [2]. Recent developments in MEMS accelerometer technology have rekindled research interest in the technique [3, 4].

The modern-day ubiquity of accelerometers in wearable devices and smart phones is quickly making SCG an inexpensive data acquisition tool. Such devices have been used to accurately obtain heartbeat intervals [5, 6, 7], and the possibility of using SCG to obtain useful heart rate variability indices has been explored by us [8], and others [7, 9]. One of the main limitations of all these algorithms is the differences in the signal between individuals. While the fiducial points are almost always identifiable in a healthy signal, their relative amplitudes as well as the behaviour of the signal following them can be quite variable.

The timing of peaks observed in SCG have been related to significant cardiac events, the main ones being mitral valve closing (MC), isovolumic moment (IM) and aortic valve opening (AO) during the systolic cycle, and aortic valve closure (AC) during the diastolic cycle (Fig. 5.1). The assignment of these fiducial points was based on the echocardiogram

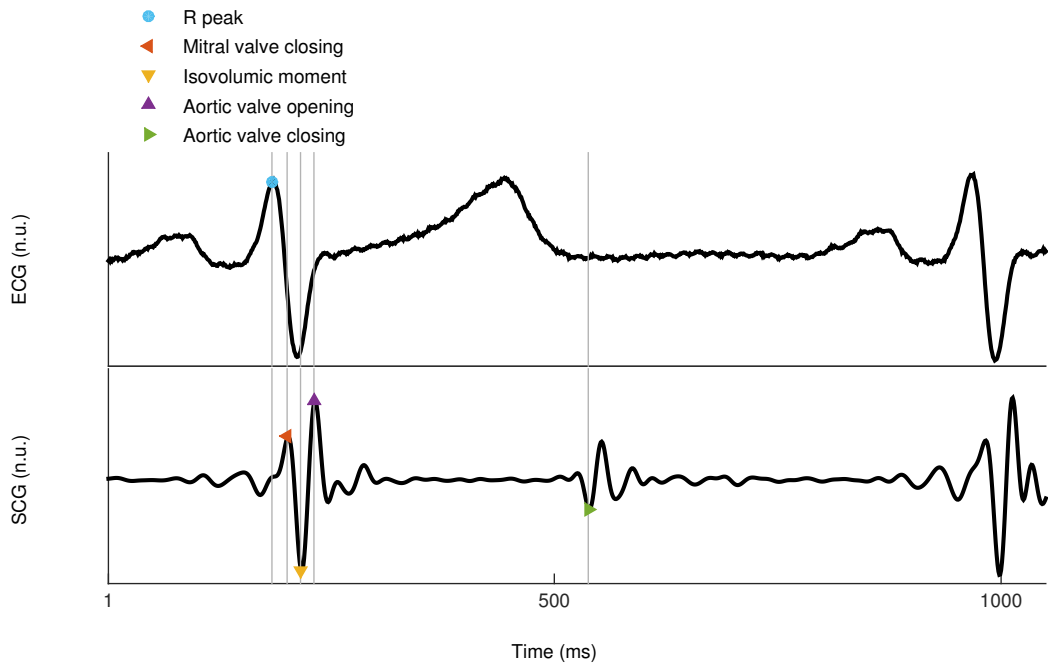

Figure 5.1: Example electrocardiogram (ECG) and seismocardiogram (SCG) with relevant fiducial points. SCG signals exhibit important variations between individuals. Although these four fiducial points are identifiable in all healthy signals, their relative amplitudes as well as the behaviour of the signal following them can be quite variable.

analysis of SCG morphology [10, 11]. Precise mechanical timings of the cardiovascular system that can only be obtained from SCG depend critically on accurately identified fiducial points [12, 13].

Although the moments in time when some important features of SCG occur have been identified, a gap remains in our knowledge of the forces that cause them. Indeed, in the case of the aortic valve opening and closing fiducial points, it is implausible that the low frequency vibration peaks are caused by the valves themselves. In the case of the isovolumic moment fiducial point, the exact meaning of the timing is highly implicit. The definition of this point is the absolute minimum attained by the signal during isovolumic contraction, and isovolumic contraction itself is defined as the entire lapse of time between mitral valve closure and aortic valve opening. So far, then, the IM point has a clear significance only on SCG, with an imprecise physiological interpretation.

The goal of this study was to design a 3D representation of the thorax to simulate SCG and explore the precise mechanical causes of sternum vibrations during heart beats.

Important initial work has been conducted on a SCG heart and rib model [14]. This earlier model included practical simplifications that rendered derived results difficult to interpret. To strengthen the physiological interpretation of the results, simulations on a set of two models of the thoracic cage were compared. The first model was idealized with

basic shapes and the second was life-like. Both models incorporated measured values for the viscoelastic properties of cortical bone, cancellous bone, and costal cartilage.

To simulate the SCG measurement, a force function representing a heart beat was applied on the zone of contact between the heart and the rib cage, and the acceleration of a second zone in the middle of the xiphoid process was then computed.

5.2 Methods

5.2.1 Numerical considerations

To examine the mechanical propagation of thoracic vibrations due the forces from the heart, the standard equations for damped elastic wave propagation were considered, which depend on the viscoelastic properties the constituent materials. The formulation assumed that the stress tensor σ depended linearly on the deformation tensor ε, that the stress at time t depended only on the deformation at time t, and that the stresses at point x depended only on the deformations at point x. Furthermore, small displacements and small deformations were assumed such that at any time, the domain of the elastic body could be identified to the initial configuration Ω, and that the equations could be linearized. A viscous damping formulation was used, and all materials were considered isotropic.

The system then became

$$\begin{cases} u(x,0) = 0 & x \in \Omega, \\ \frac{\partial u}{\partial t}(x,0) = 0 & x \in \Omega, \\ \rho \frac{\partial^2 u}{\partial t^2} - \operatorname{div} \mathbf{C}\varepsilon(u) + \operatorname{div}\left[c_k \mathbf{C}\right]\varepsilon(\frac{\partial u}{\partial t}) = g(x,t) & x \in \Omega, t > 0, \\ \mathbf{C}\varepsilon(u)(x,t)\vec{n} = h(x,t) & x \in \Gamma, t > 0, \end{cases} \tag{5.1}$$

where u was displacement, t was time, ρ was density, c_m was the mass-proportional damping coefficient, c_k was the stiffness-proportional damping coefficient, $\mathbf{C}$ was the elasticity tensor of the given materials, ε was the deformation tensor, Γ was the surface boundary of Ω, and $\vec{n}$ was the outward normal to Γ.

The variable for which the system was solved was the displacement $u(x,t)$.

5.2.2 Viscoelastic properties

The thoracic cage was considered to be comprised of three materials: cortical bone, cancellous bone, and cartilage. The domain Ω was appropriately divided into three parts $\Omega_{\{1,2,3\}}$, where the material-dependent parameters $\rho(x)$, $c_m(x)$, $c_k(x)$, and $\mathbf{C}(x)$ were constant.

The viscoelastic properties of the sternum, costal cartilage, ribs, and lungs were obtained from the literature [15, 16, 17, 18, 19, 20, 21] (Table 5.1). These values in the sternum and ribs were assumed to be more similar to those of the iliac crest than of load-bearing bones

Table 5.1: Viscoelastic properties of the sternum, costal cartilage, and ribs.

	Bone cortical/cancellous [15, 16, 21]	Cartilage [17]	Lungs [18, 19, 20]
Young's modulus (GPa)	3.8/3.0	$5.2 \cdot 10^{-3}$	$1.0 \cdot 10^{-4}$
Poisson ratio	0.3/0.3	0.3	0.4
Density (kg/m^3)	$2.0 \cdot 10^3/2.0 \cdot 10^3$	$1.5 \cdot 10^3$	280
Stiffness-proportional damping coeff. (s)	$6.7 \cdot 10^{-2}/6.7 \cdot 10^{-2}$	0.13	$\sim$

such as the femur. The computations necessary to approximate thermoelastic damping as viscous damping are included in the appendix.

The lung material was considered sufficiently soft (small Young's modulus), and light (low density) to be approximated with an unconstrained boundary condition on the bones and cartilage.

5.2.3 Boundary conditions

Three relevant boundaries $\Gamma_{\{a,b,c\}}$ were identified. Γ_a represented the area where the ribs would attach to the vertebral column. The displacement there was fixed at 0 (Dirichlet boundary condition).

$$u(x,t) = 0 \qquad x \in \Gamma_a, t > 0. \tag{5.2}$$

The area of contact with the heart was represented by Γ_b, where a force F was applied uniformly. The displacement there depended on F as

$$\mathbf{C}\varepsilon(u)(x,t) = F(t) \qquad x \in \Gamma_b, t > 0. \tag{5.3}$$

The function F represented the force that would be exerted on this zone by the heart. This force was defined as shown in Fig. 5.2, and was composed mainly of a large sustained relative pull, lasting 300 ms that represented systole. This pull was flanked on both sides by smaller pushes. The first push represented atrial contraction and the second, diastolic recoil. The transition periods between the pushes and the pull were all 10 ms.

Certain assumptions on the heart and pericardium were made for the design of the force F. It was assumed that the heart created forces parallel to its outward normal, and that the distance between the heart and parietal pericardium was negligible it the zone Γ_c where the lungs aren't interposed between the heart and the thoracic cage. It was further assumed that the pericardial fluid acts as a perfect lubricant between the heart and the surrounding media, and that F was positive when the heart either pushed or rested on the thoracic cage,

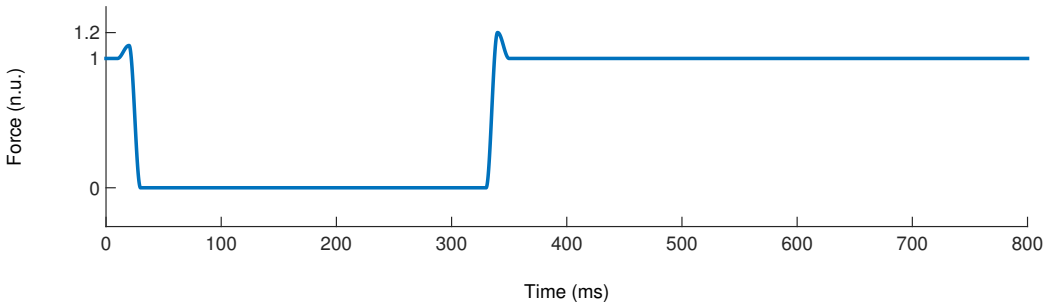

Figure 5.2: The force input on the thoracic zone of contact with the heart. The initial push represents a slight positive force caused by the contraction of the atria, the prolonged pull is caused by ventricular systolic contraction, and the subsequent final push is caused by the recoil following the closure of the aortic valve.

and was 0 otherwise. These assumptions give rise to the fact that any positive F should be applied homogeneously on Γ_b in the normal direction, and therefore does not depend on x

$$F(x,t) = F(t) \qquad x \in \Gamma_b \tag{5.4}$$

The boundaries not included in either the area where the ribs would attach to the vertebral column, or the zone of contact with the heart were represented by Γ_c and were unconstrained.

$$\Gamma_c = \Gamma/(\Gamma_a \cup \Gamma_b), \tag{5.5}$$

and

$$\mathbf{C}\varepsilon(u)(x,t) = 0 \qquad x \in \Gamma_c, t > 0. \tag{5.6}$$

5.2.4 Meshes

The solution algorithm was run on a set of two 3D volume meshes; the first was idealized with basic shapes, and the second was life-like.

The life-like surface mesh was adapted from a ZygoteBody (Zygote Media Group Inc., American Fork, UT, USA) full-body human male mesh. The sternum, costal cartilage, and ribs were considered (Fig. 5.3).

The different parts of the initial mesh were adjusted from quadrilaterals to triangles, and then joined with 3-Matic (Materialise, Leuven, Belgium). The resulting surface mesh was automatically adjusted for regularity with Yams (Inria, FRA), and used to create a 3D tetrahedral mesh with GSH3D (Inria, FRA).

The idealized mesh was designed to represent the thoracic geometry while bypassing meshing problems such as sharp angles, narrow volumes, and connection between parts. It included the cortical and cancellous parts of the manubrium and sternum body, the xiphoid process, and two sets of 6 ribs with their respective costal cartilages. Dimensions were

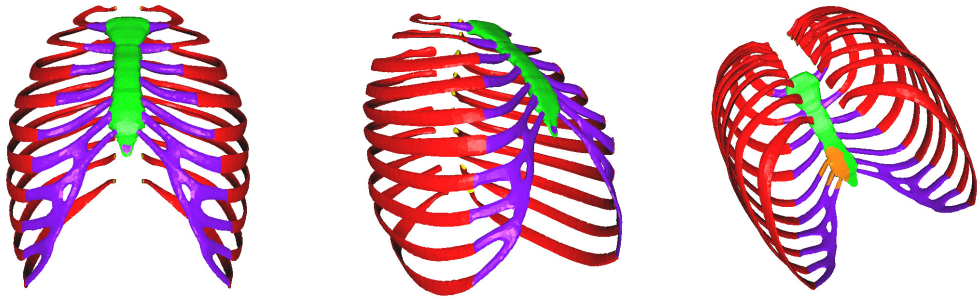

Figure 5.3: The life-like sternum (green), costal cartilage (purple), and rib (red) meshes. In the **left** and **middle** panels, the dark pink spot on the ziphoid process represents the zone of observation corresponding to standard seismocardiography data collection methods. The **right** panel shows the mesh from the back, slightly askew, with the zone of contact with the heart in orange.

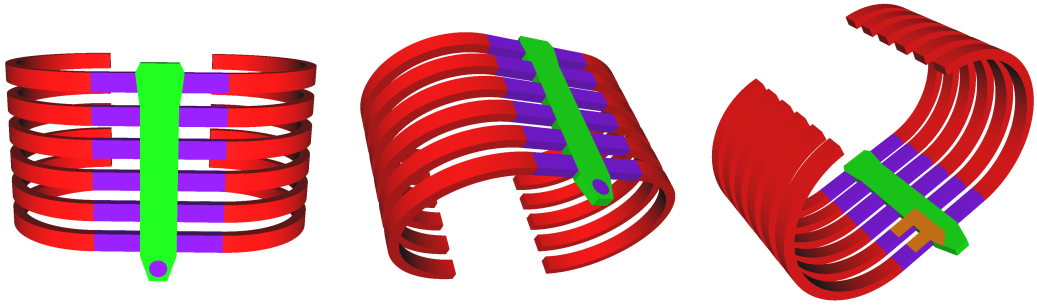

Figure 5.4: The idealized sternum (green), costal cartilage (purple), and rib (red) meshes. In the **left** and **middle** panels, the dark pink spot on the ziphoid process represents the zone of observation corresponding to standard seismocardiography data collection methods. The **right** panel shows the mesh from the back, slightly askew, with the zone of contact with the heart in orange.

estimated from rough averages on the life-like mesh. The thickness of all the elements was 1.2 cm, the width of the sternum body was 4 cm, the height of the entire sternum was 23 cm, the length of the costal cartilage pieces was 5 cm, and the diameter of the rib hemi-cyclinders was 20 cm. The surface geometry was used to create a volume mesh of maximum edge length 5 mm with Gmsh (open source by Christophe Geuzaine and Jean-François Remacle, FRA).

On the life-like thoracic mesh, the zone of contact with the heart was identified from a standard anatomy textbook [22] (Fig. 5.3, **Right**), and then estimated on the idealized mesh.

The solution to the system was approximated by linear finite elements with a second order centered implicit time discretization based on the Leap-Frog scheme [23].

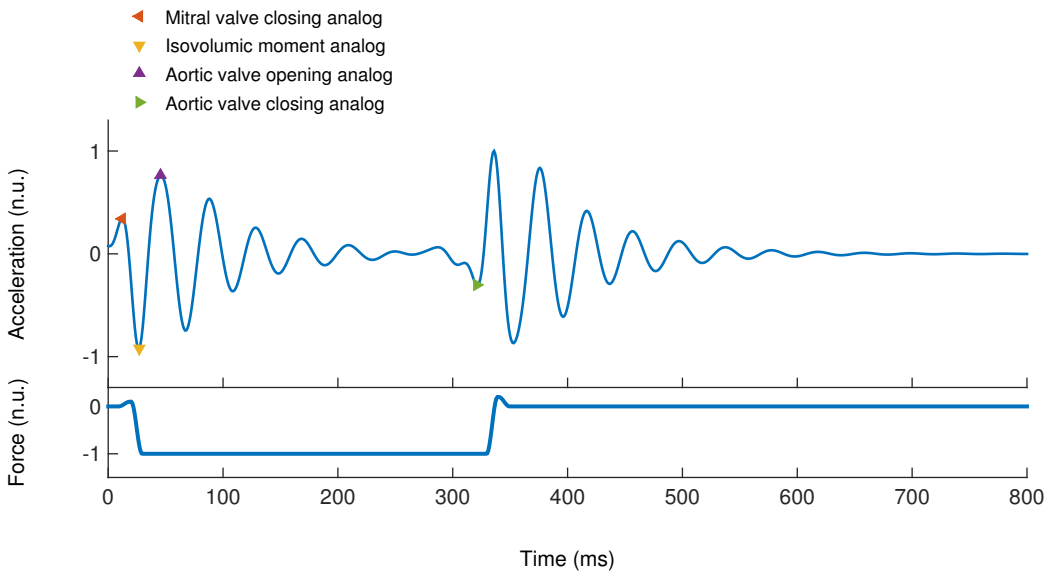

Figure 5.5: Filtered simulated seismocardiogram from the life-like mesh showing four fiducial point analogs. **Top** Mean acceleration of the zone of observation in the middle of the xiphoid process (Fig. 5.3 **Left, Middle**), in the direction of the outward normal. The signal was input to the SCG annotation algorithm (Chap. 4), which applied a band-pass filter in the relevant frequency band, and returned the mitral valve closing, isovolumic moment, and aortic valve opening fiducial point analogs. The aortic valve closing fiducial point analog was estimated by observation. **Bottom** The force function F, applied on the zone of contact with the heart.

5.3 Results and discussion

The goal of this study was to reproduce an SCG-like output from a physiologically correct *in-silico* 3D mechanical model of the thorax. The model included cortical and cancellous sternal bone, costal cartilage, and ribs. A force was considered that consisted of a long sustained pull to represent systole, flanked on both sides by short and relatively smaller pushes to represent atrial contraction in the beginning, and a diastolic recoil at the end. From u, the spatial mean of acceleration was computed as

$$\bar{a} = \int_{x \in O} \frac{\partial^2 u}{\partial t^2} \cdot \vec{n}$$

where O was the zone of observation in the middle of the xiphoid process shown in Figs. 5.3 and 5.4. This acceleration was considered to simulate SCG. The overall morphology of the simulated SCG on the life-like mesh (Fig. 5.5) comprised many morphological similarities to the set of 2 wave trains seen in *in-vivo* SCG (Figs. 4.7, 4.8, 5.1).

To quantify the degree to which the simulated SCG resembled *in-vivo* SCG, it was formatted as an input to the automatic annotation algorithm described in Chapter 4. For both meshes, the systolic segment of the simulated SCG included analogs to all three fiducial

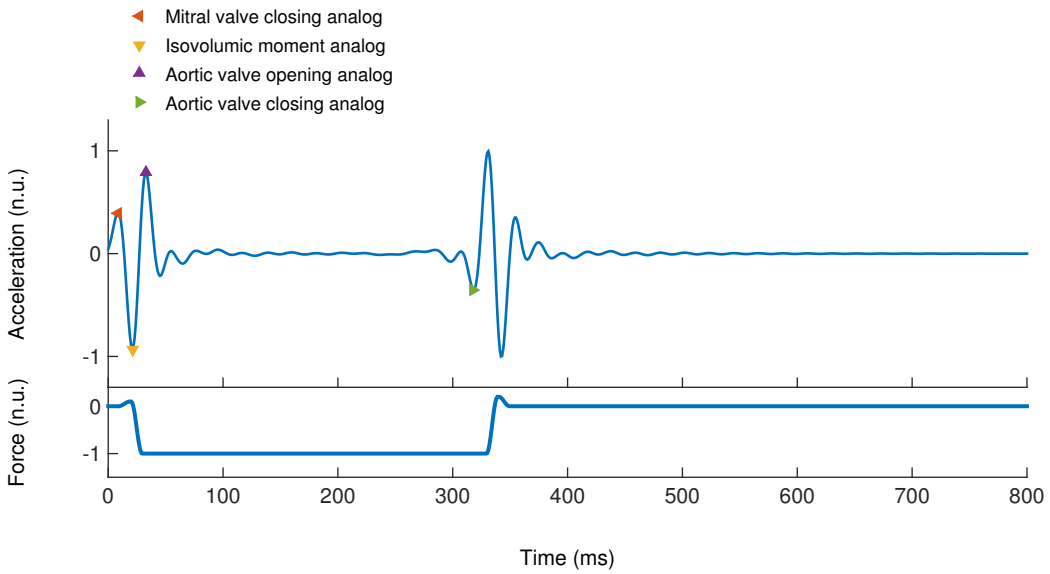

Figure 5.6: Filtered simulated seismocardiogram from the idealized mesh showing the four fiducial point analogs. **Top** Mean acceleration of the zone of observation in the middle of the xiphoid process (Fig. 5.3 **Left, Middle**), in the direction of the outward normal. The signal was input to the algorithm described in Chapter 4, which applied a band-pass filter in the relevant frequency band, and returned the mitral valve closing, isovolumic moment, and aortic valve opening fiducial point analogs. The aortic valve closing fiducial point analog was estimated by observation. **Bottom** The force function F, applied on the zone of contact with the heart.

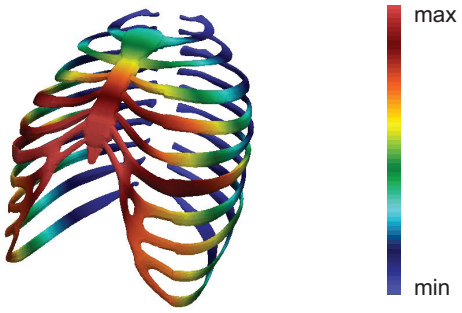

Figure 5.7: Life-like thoracic mesh showing relative total acceleration on all surfaces at the time of the isovolumic moment point analog.

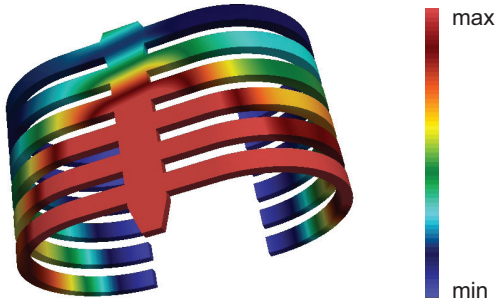

Figure 5.8: Idealized thoracic mesh showing relative total acceleration on all surfaces at the time of the isovolumic moment point analog.

points, namely the MC, IM, and AO points. The validity of the AC point analog is less clear, as it is not the absolute minimum of the diastolic segment.

Following the main peaks, the simulated SCG exhibited oscillatory behaviour at what seems to be the first resonance frequency. Although the physiological interpretation of this result should be approached cautiously, it encourages the notion that *in-vivo* fiducial points are caused by sudden heart movements, followed by periods of regular damped oscillation.

In the life-like simulation, the MC analog occurred 2 ms after the onset of the positive force that represented atrial contraction, and the IM analog occurred 7 ms after the onset of isovolumic contraction. The time difference between the AO and MC peak analogs is 34 ms, which is slightly below the standard implicit lower limit of 40 ms. The interpretation of the AO peak is tenuous, however, as the force function F did not distinguish between

isovolumic contraction and ejection period during its sustained pulling period, and therefore cannot pinpoint a theoretical AO.

The relative differences between the life-like and idealized simulations suggested two conclusions. Firstly, that the overall morphology of the simulated SCG was not affected by either the finesse or regularity of the mesh. Secondly, that the geometry of the mesh did affect the resonant frequency. Although there remained clear fiducial point analogs in both cases, the unfiltered oscillation frequencies were of 24.9 and 95.2 Hz for the life-like and idealized meshes, respectively.

The model considered in some detail the ribs, costal cartilage, xiphoid process, as well as the cortical and trabecular constituents of the manubrium and sternum body. For the sake of simplicity of this first iteration, a number of organs and physiological processes were omitted. One of the most important omitted process was breathing, which is known to affect the SCG amplitude [24]. Since, however, breathing has not been shown to affect the frequency content of SCG in the relevant range, it was assumed that the system could adequately represented the end of expiration. The lungs were also not included under the assumption that they should at most dampen the longitudinal propagation of the vibrations, especially at the end of expiration, and thus minimally affect the point of observation on the xiphoid process.

The most obvious missing organ is, of course, the heart itself. The mechanical modelling of a beating heart, including its attachments at the level of the atria and the boundary conditions caused by the pericardium, is quite onerous. Its inclusion will be the next step in our modelling process. It will greatly increase the level of complexity of the model as well as its physiological relevance.

The ultimate goal is to characterize the transfer function between the movements of the heart and the derived simulated SCG, and therefore enable accelerometer measurements to return information about subject-specific heart forces and movements.

The simulated SCG signals obtained from the life-like and idealized meshes included many of the key morphological components of *in-vivo* signals. The initial model reacted well and encourages further work to increase its complexity.

Appendix

Approximation of thermoelastic damping by viscous damping

Generally, the standard equations for damped elastic wave propagation include

$$\rho \frac{\partial^2 u}{\partial t^2} - \operatorname{div} \sigma = g(x,t), \tag{5.7}$$

where u is displacement, t is time, and ρ is density.

In the viscous damping formulation, the σ term incorporates the stiffness-proportional damping coefficient c_k as

$$\sigma(x,t) = \mathbf{C}\varepsilon(u) + c_k\mathbf{C}\varepsilon(\frac{\partial u}{\partial t}), \tag{5.8}$$

where $\mathbf{C}$ is the elasticity tensor, and ε is the deformation tensor. Notice that

$$\begin{aligned} \hat{\sigma}(x,\omega) &= \mathbf{C}\varepsilon\big(\hat{u}(x,\omega)\big) + i\omega c_k\mathbf{C}\varepsilon\big(\hat{u}(x,\omega)\big) & (5.9)\\ &= \Big(1 + i\omega c_k\Big)\mathbf{C}\varepsilon\big(\hat{u}(x,\omega)\big), & (5.10)\end{aligned}$$

where $\hat{f}$ denotes the Fourier transform of f.

In the thermoelastic damping formulation, the σ term incorporates stress relaxation as

$$\sigma(x,t) = \mathbf{C}\varepsilon(u) + \frac{c}{\tau}\int_0^t e^{-s/\tau}\mathbf{C}\varepsilon\big(u(x,t-s)\big)ds, \tag{5.11}$$

where c is related to instantaneous stress relaxation, and τ describes this relaxation over time. In this case

$$\hat{\sigma} = \mathbf{C}\varepsilon\big(\hat{u}(x,\omega)\big) + \mathcal{F}\Big(\frac{c}{\tau}H(t)e^{-t/\tau}\Big)\mathbf{C}\varepsilon\big(\hat{u}(x,\omega)\big), \tag{5.12}$$

where $\mathcal{F}$ is the Fourier operator, and H is the Heaviside unit step function.

The Fourier transform in the second term is well known, and the equation becomes

$$\hat{\sigma} = \mathbf{C}\varepsilon\big(\hat{u}(x,\omega)\big) + \frac{c}{1+i\omega\tau}\mathbf{C}\varepsilon\big(\hat{u}(x,\omega)\big). \tag{5.13}$$

Considering the frequency of maximal source energy ω_0, the above equation becomes

$$\begin{aligned} \hat{\sigma} &= \mathbf{C}\varepsilon\big(\hat{u}(x,\omega)\big) + \Big(\frac{-c}{1+\omega_0^2\tau^2} + \frac{i\omega\tau c}{1+\omega_0^2\tau^2}\Big)\mathbf{C}\varepsilon\big(\hat{u}(x,\omega)\big) & (5.14)\\ &= \Big(1 + i\omega\frac{c}{\omega_0^2\tau^2}\Big)\mathbf{C}'\varepsilon\big(\hat{u}(x,\omega)\big), & (5.15)\end{aligned}$$

where $\mathbf{C}'$ incorporates a constant of the form $1 - c/(1+\omega_0^2\tau^2)$ in its elastic moduli.

Since the energy of the the source force F is highest at $\omega_0 = 1.3$, and considering the case in [17] where $\tau = 1 \Rightarrow c = 0.3$, the equation

$$\hat{\sigma} = \Big(1 + i\omega\cdot 0.13\Big)\mathbf{C}'\varepsilon\big(\hat{u}(x,\omega)\big). \tag{5.16}$$

Comparing equations 5.9 and 5.16, the final value becomes

$$c_k \approx 0.13. \tag{5.17}$$

5.4 References

[1] R. M. Baevsky, A. D. Egorov, and L. A. Kazarian, "The Method of Seismocardiography," *Kardiologiia*, vol. 18, pp. 87–9, Jan. 1964.

[2] D. Salerno, J. M. Zanetti, L. Poliac, R. Crow, P. Hannan, K. Wang, I. Goldenberg, and R. Van Tassel, "Exercise Seismocardiography for Detection of Coronary Artery Disease," *American Journal of Noninvasive Cardiology*, pp. 321–330, 1992.

[3] J. M. Zanetti and K. Tavakolian, "Seismocardiography : Past , Present and Future," in *IEEE Engineering in Medicine and Biology Society Conference*, (Osaka, Japan), pp. 7004–7007, 2013.

[4] O. Inan, P.-F. Migeotte, K.-S. Park, M. Etemadi, K. Tavakolian, R. Casanella, J. Zanetti, J. Tank, I. Funtova, K. Prisk, and M. Di Rienzo, "Ballistocardiography and Seismocardiography: A Review of Recent Advances," *IEEE Journal of Biomedical and Health Informatics*, vol. 30308, no. c, pp. 1–1, 2014.

[5] M. Di Rienzo, E. Vaini, B. Bruno, P. Castiglioni, P. Lombardi, G. Parati, C. Lombardi, P. Meriggi, and F. Rizzo, "Wearable seismocardiography: Towards the beat-to-beat assessment of cardiac mechanics during sleep in microgravity," *2014 8th Conference of the European Study Group on Cardiovascular Oscillations, ESGCO 2014*, pp. 239–240, 2014.

[6] M. Di Rienzo, E. Vaini, P. Castiglioni, P. Lombardi, P. Meriggi, and F. Rizzo, "A Textile-Based Wearable System for the Prolonged Assessment of Cardiac Mechanics in Daily Life," in *IEEE EMBC*, pp. 6896–6898, 2014.

[7] J. Ramos-Castro, J. Moreno, H. Miranda-Vidal, M. a. García-González, M. Fernández-Chimeno, G. Rodas, and L. Capdevila, "Heart rate variability analysis using a seismocardiogram signal.," *Conference proceedings: Annual International Conference of the IEEE Engineering in Medicine and Biology Society. IEEE Engineering in Medicine and Biology Society. Conference*, vol. 2012, pp. 5642–5, 2012.

[8] A. Laurin, A. Blaber, and K. Tavakolian, "Seismocardiograms return valid heart rate variability indices," in *Computing in Cardiology Conference*, pp. 413–416, 2013.

[9] M. J. Tadi, E. Lehtonen, T. Koivisto, M. Pankaala, A. Paasio, and M. Teras, "Seismocardiography: Toward heart rate variability (hrv) estimation," in *Medical Measurements and Applications (MeMeA), 2015 IEEE International Symposium on*, pp. 261–266, IEEE, 2015.

[10] R. Crow, P. Hannan, D. Jacobs, L. Hedquist, and D. Salerno, "Relationship between seismocardiogram and echocardiogram for events in the cardiac cycle," *American journal of Noninvasive Cardiology*, vol. 8, no. 39, pp. 39–46, 1994.

[11] K. Tavakolian, A. Blaber, B. Ngai, and B. Kaminska, "Estimation of hemodynamic parameters from seismocardiogram," in *Computing in Cardiology*, (Belfast), pp. 1055–1058, 2010.

[12] K. Tavakolian, G. A. Dumont, G. Houlton, and A. P. Blaber, "Precordial vibrations provide noninvasive detection of early-stage hemorrhage," *Shock*, vol. 41, no. 2, pp. 91–96, 2014.

[13] D. M. Salerno and J. Zanetti, "Seismocardiography for monitoring changes in left ventricular function during ischemia.," *CHEST Journal*, vol. 100, no. 4, pp. 991–993, 1991.

[14] V. Gurev, K. Tavakolian, J. Constantino, B. Kaminska, A. P. Blaber, and N. A. Trayanova, "Mechanisms underlying isovolumic contraction and ejection peaks in seismocardiogram morphology," *Journal of Medical and Biological Engineering*, vol. 32, no. 2, pp. 103–110, 2012.

[15] S. C. Cowin, *Bone mechanics handbook*. CRC Press, 2001.

[16] J. L. Kuhn, S. A. Goldstein, R. Choi, M. London, L. A. Feldkamp, and L. S. Matthews, "Comparison of the trabecular and cortical tissue moduli from human iliac crests," *Journal of Orthopaedic Research*, vol. 7, pp. 876–884, Nov. 1989.

[17] A. Lau, M. L. Oyen, R. W. Kent, D. Murakami, and T. Torigaki, "Indentation stiffness of aging human costal cartilage," *Acta Biomaterialia*, vol. 4, pp. 97–103, Jan. 2008.

[18] S. J. Lai-Fook, T. A. Wilson, R. E. Hyatt, and J. R. Rodarte, "Elastic constants of inflated lobes of dog lungs," *Journal of Applied Physiology*, vol. 40, no. 4, pp. 508–513, 1976.

[19] G. C. Lee and A. Frankus, "Elasticity properties of lung parenchyma derived from experimental distortion data," *Biophysical Journal*, vol. 15, no. 5, pp. 481–493, 1975.

[20] M. H. Tawhai, M. P. Nash, C.-L. Lin, and E. A. Hoffman, "Supine and prone differences in regional lung density and pleural pressure gradients in the human lung with constant shape," *Journal of Applied Physiology*, vol. 107, no. 3, pp. 912–920, 2009.

[21] E. Garner, R. Lakes, T. Lee, C. Swan, and R. Brand, "Viscoelastic dissipation in compact bone: implications for stress-induced fluid flow in bone," *Journal of biomechanical engineering*, vol. 122, no. 2, pp. 166–172, 2000.

[22] F. H. Netter, *Atlas of human anatomy*. Elsevier Health Sciences, 2014.

[23] P. Joly, "Variational methods for time-dependent wave propagation problems," in *Topics in computational wave propagation*, pp. 201–264, Springer, 2003.

[24] K. Pandia, O. T. Inan, G. T. Kovacs, and L. Giovangrandi, "Extracting respiratory information from seismocardiogram signals acquired on the chest using a miniature accelerometer," *Physiological measurement*, vol. 33, no. 10, p. 1643, 2012.

Chapter 6

Summary

> A regression to ancient forms? A glimpse of future evolutions? Or a fleeting alteration of the present?
>
> *Vorel of the Hull Clade*

The studies contained in this thesis developed and applied new methods of signal analysis to obtain cardiac event timings and thus clarify the relationships between various cardiovascular variables.

It was first showed that the ability of a new peak detection method to return valid frequency and phase characteristics of physiological signals. The implications of this result extend beyond the scope of just phase and frequency, however, due to the particular characteristics of this method *versus* those of the gold standards wavelet and Hilbert techniques. Indeed, the peak detection technique inherently divides the analysed signal into a series of individual cycles. In most physiological cases, these cycles can be interpreted individually in terms of amplitudes, timings, etc. This allows us to make precise measurements of phenomena at the moment when they occur, instead of averaging over a certain period of time. Because this peak detection method is able to obtain phase as well, or better than the traditional techniques, it can be advanced that its divisions are valid. Some possibilities of this use of the peak detection technique were explored in the second chapter.

The relationship between DAP and MSNA is intricate and often difficult to quantify in a way that lends itself to simple interpretation. The peak detection method was applied to these signals to compare its results to traditionally obtained indices, in an attempt to complement the existing theory. Individual cycles were quantified in terms of amplitudes, strength, and relative timings. Six new indices were computed from which changes in the cardiovascular system caused by LBNP could be observed, as well as some differences between subjects who fainted during the protocol and those who did not. Most notably,

the index named *stimulus slope* was able to distinguish between the 2 groups at the lowest level of LBNP.

These new indices not only offer a way of predicting LBNP induced orthostatic intolerance, but also help clarify the processes involved in healthy and pathological baroreflexes. While coherence and gain together have been used to to quantify the general strength of the relationship between DAP and MSNA, stimulus slope provides a measurement of the MSNA response to a particular DAP stimulus. In this sense, the interpretation that can be made is simpler and more direct.

In some cases, peak detection is clearly not enough to properly characterise a signal. This is the case for SCG, where peak detection has been used to segment cardiac cycles and identify fiducial points. SCG is problematic for this approach because its important morphological features vary in relative amplitude between successive cycles as well as between individuals. To accurately and consistently identify SCG features a specialised software was developped that required no user input. This software first identified the beginning of systole, and then fitted a model with adaptable relative amplitudes to the vibrations therein. In this way, identification of all the peaks of the relevant segments was made at the same time without making assumptions as to which peaks would be the highest and lowest.

The algorithm described in chapter 4, which identified fiducial points on SCG was accurate and consistent enough to obtain amplitudes and timings in individual cycles, as well as HRV indices. Contrary to existing algorithms, this was done without concurrent signals, and thus open opportunities for the use of SCG in standalone applications.

Our efforts in quantifying and analysing SCG were continued in chapter 5, where a mechanical model of the thoracic cage was described. The goal of this modelling was to investigate the cause of thoracic vibrations caused by the heart, and thus complement the exiting timing interpretations of this signal. A simulated SCG was computed with the use of traditional wave propagation systems of equations, and by inputing the viscoelastic properties of bone and cartilage into a life-like mesh. The obtained simulation comprised all the features as identified in the algorithm described in chapter 4. The vibrations simulated by this model arose mostly from the first mode of resonance of the structure. This generated the hypothesis that the main peaks and frequency of SCG are not caused are caused by cardiac events inasmuch as they are started by the onset of systole but result from characteristics of the thorax as a whole.

This last hypothesis necessitates much more modelling and testing to be validated. More organs and processes should be included in the existing model, and *in-vivo* experiments measuring the resonance frequency of the thorax should be performed. This work could be complemented by the development of end-user applications to present relevant state-of-the-art cardiovascular data in a way conducive to its inclusion in daily life choices.